

Molecular Modeling of Polymer Free Volume Distribution

A Dissertation
Presented to
The Academic Faculty

by

Derrick B. Callander

In Partial Fulfillment
Of the Requirements for the Degree
Doctor of Philosophy in Chemical and Biomolecular Engineering

Georgia Institute of Technology

December 2005

Copyright © Derrick B. Callander 2005

Molecular Modeling of Polymer Free Volume Distribution

Approved by:

Dr. Peter J. Ludovice, Advisor
School of Chemical and Biomolecular
Engineering
Georgia Institute of Technology

Dr. Clifford L. Henderson
School of Chemical and Biomolecular
Engineering
Georgia Institute of Technology

Dr. Christopher W. Jones
School of Chemical and Biomolecular
Engineering
Georgia Institute of Technology

Dr. William J. Koros
School of Chemical and Biomolecular
Engineering
Georgia Institute of Technology

Dr. C. David Sherrill
School of Chemistry
Georgia Institute of Technology

Date Approved: July 8, 2005

To my wife Najah and my mother Iris

ACKNOWLEDGMENTS

I would like to thank the following individuals and/or institutions for their help in the completion of this work:

- Dr. Peter J. Ludovice for being a mentor
- Dr. Sherrill and the Center for Computational Molecular Science and Technology for computational resources and assistance with quantum calculations
- Dr. Henderson and Trevor Hoskins for HFA PNB sample preparation
- Dr. Jean and his research group at UMKC for PALS measurements
- The Ludovice research group, past and present, for their friendship and support

TABLE OF CONTENTS

Acknowledgements.....	iv
List of Tables	viii
List of Figures.....	xi
Nomenclature.....	xvi
Summary.....	xx
<u>Chapter 1 Introduction</u>	1
1.1 Motivation and Goals.....	1
1.2 Polyethylene Terphthalate.....	4
1.3 Polynorbornene.....	6
1.4 Molecular Modeling Introduction.....	10
1.5 Molecular Dynamics.....	12
1.6 Molecular Mechanics.....	13
1.7 Force Field.....	14
1.8 Polymer Glasses.....	15
References.....	17
<u>Chapter 2 Polyester Modeling</u>	20
2.1 PET-Previous Experimental and Simulated Work.....	21
2.2 Verification of the Ethylene Glycol Trans/Gauche Fraction in PET.....	23
2.2-1 <i>ab – initio</i> Calculations	24
2.2-2 Semi Empirical Calculations.....	26
2.2-3 Molecular Mechanics Calculations.....	28
2.2-4 Molecular Dynamics Calculations.....	30
2.3 Rotational Isomeric States Models.....	32

2.3-1 Original RIS Model for Polyethylene Terephthalate.....	36
2.3-2 Development of New RIS Model for PET.....	38
2.3-3 New RIS Model for PET & PEN.....	56
2.4 Bulk Models for Polyesters.....	58
2.4-1 Force field Development PET.....	60
References.....	73
<u>Chapter 3 Polyester Free Volume Analysis</u>	75
3.1 Free Volume Basics.....	75
3.2 PET & PEN PALS.....	76
3.3 Modeling Free Volume via Simulations.....	77
3.4 Simulated Polyester Free Volume Results.....	81
References.....	95
<u>Chapter 4 Hexafluoroalcohol Substituted Polynorbornene Modeling</u>	97
4.1 HFA-PNB Previous Experimental and Simulated Work.....	99
4.2 HFA-PNB Simulated Intermediate Models.....	102
References.....	107
<u>Chapter 5 HFA-PNB Free Volume</u>	108
5.1 HFA-PNB Positron Annihilation Lifetime Spectroscopy Experiment.....	108
5.2 HFA-PNB Free Volume Analysis Amorphous Sample.....	114
5.3 HFA-PNB Clustering Amorphous Sample-Volume Analysis.....	119
5.4 HFA-PNB Clustering Amorphous Sample-Shape Analysis.....	123
5.5 HFA-PNB Clustering Amorphous Sample- τ_3 Analysis.....	125
References.....	133
<u>Chapter 6 Conclusions and Recommendations</u>	134
Polyethylene Terephthalate (PET) and Polyethylene Napthalate (PEN).....	134

Conclusions.....	134
Recommendations.....	135
Hexafluoroalcohol substituted Polynorbornene (HFA-PNB).....	135
Conclusions.....	135
Recommendations.....	137

LIST OF TABLES

Table 1-1: Comparison of selected PET and PEN properties.....	6
Table 2-1: <i>ab-initio</i> results for ethylene glycol geometry optimizations. The angle value in parentheses represents the final torsion angle value after minimization.....	25
Table 2-2: Semi empirical geometry optimization calculations on ethylene glycol. The angle value in parentheses represents the final torsion angle value after minimization.....	27
Table 2-3: Bond angles and bond lengths derived from DFT calculations at B3LYP/6-31G** level of theory. Averages and confidence intervals represent data extracted over 10 sampled conformations.....	43
Table 2-4: Local energy minima of torsion angles as assigned by Flory for PET and from DFT calculations at B3LYP/6-31G** level of theory. Averages and confidence intervals represent data extracted over 10 sampled conformations.....	45
Table 2-5: Relative energy minima of RIS Bond torsion angles from DFT calculations at B3LYP/6-31G** level of theory.....	46
Table 2-6: Results of <i>ab-initio</i> calculations on methyl benzoate.....	48
Table 2-7: Using a MATLAB unconstrained minimization routine, statistical weight parameters were selected that most closely matched the overall targets. The resulting bond probabilities were not fixed or targets in the routine but were defined by the parameter selection.....	51
Table 2-8: Using Flory's original geometric parameters, the above values were calculated using the aforementioned matrix generation method.....	52
Table 2-9: Derivative analysis shows the dependence of each target on the basic statistical weight parameters.....	54
Table 2-10: Summary of new PET RIS model.....	56
Table 2-11: Statistical weight matrices assignment for PET and PEN.....	57

Table 2-12: Chain building statistics for PET and PEN models. Confidence limits shown represent 95% on 30 models for PET and 17 models for PEN.....	59
Table 2-13: Initial and final forms of the OCCO intrinsic torsional potential.....	62
Table 2-14: PET build first relax data.....	63
Table 2-15: Final form of the OCCO intrinsic torsion potential [2.35] used for PET relaxation.....	65
Table 2-16: Initial and final COCC intrinsic torsion potentials for PET.....	66
Table 2-17: Final OCCO and COCC intrinsic torsion potentials for PEN.....	67
Table 2-18: Relaxed model statistics for PET and PEN models. Confidence limits shown represent 95% on 30 models for PET and 17 models for PEN.....	68
Table 2-19: Simulated solubility parameters for 30 PET models and 17 PEN models..	69
Table 2-20: Detailed PEN model solubility parameter results.....	71
Table 3-1: PALS experimental results for PET and PEN. Experiments were performed at 25° C.....	77
Table 3-2: Number of defined tetrahedron using Delaunay tessellation at the 95% confidence level.....	81
Table 3-3: Average total free volume distribution statistics with 95% confidence intervals.....	87
Table 3-4: Total simulated fractional free volume results for PET and PEN at the 95% confidence level compared to group contribution method.....	89
Table 3-5: Table of gas diffusant radii.....	89
Table 3-6: Average largest clusters for PET and PEN at o- P_s and O_2 penetrant radii at 95 % confidence limits.....	90

Table 3-7: Average number of clusters for PET and PEN at o-Ps and O ₂ penetrant radii at 95 % confidence limits.....	90
Table 3-8: T-test results for the difference between the mean number of PET and PEN clusters for O ₂ sized penetrants.....	91
Table 5-1: The M _w and polydispersity index for HFA-PNB samples.....	109
Table 5-2: Free volume distribution statistics.....	117
Table 5-3: Three largest o-Ps clusters in amorphous HFA-PNB.....	123
Table 5-4: Cluster eigenvalues for HFA-PNB. Confidence intervals on average cluster values are 95% confidence levels.....	124
Table 5-5: Aspect ratios of HFA-PNB clusters.....	124
Table 5-6: Cluster eccentricities for HFA-PNB. The 95% confidence interval is shown for the average cluster	130

LIST OF FIGURES

Figure 1-1: Free volume curve	2
Figure 1-2: Two hypothetical polymers with the same total fractional free volume but a different free volume distribution.....	3
Figure 1-3: PET repeat unit.....	4
Figure 1-4: 2-6 PEN repeat unit.....	5
Figure 1-5: PNB by various polymerization routes.....	7
Figure 1-6: Erythro di-isotactic isomer of 2,3 poly(norbornene) (left) and the cis-transoid configuration of substituted poly(acetylene). Note that each backbone structure has alternating non-rotatable bonds in common.....	8
Figure 1-7: Stereochemical configurations of erythro (exo-exo) PNB.....	9
Figure 1-8: Polymer glass modeling protocol.....	15
Figure 2-1: Lyon's free volume analysis for PET, PEN and selected copolymers. Note that there is no significant difference in the curves.....	22
Figure 2-2: Experimental barrier data obtained from Dr. Eric Baer and Dr. Anne Hiltner's Barrier Research Group at Case Western Reserve University.....	23
Figure 2-3: Isolated ethylene glycol molecule used in ab -initio, semi-empirical, molecular mechanics and molecular dynamics work.....	24
Figure 2-4: Torsional potential for ethylene glycol using the MM+ force field.....	29
Figure 2-5: Torsional potential for ethylene glycol using the Amber force field.....	29

Figure 2-6: Molecular dynamics (300K) and performed on an isolated constrained EG molecule.....	31
Figure 2-7: PET RIS bond assignments. The Greek letters represent the statistical weight parameters for each bond and Flory's assigned values for them.....	37
Figure 2-8: Model compound selected for PET. This model compound was used in the QCHEM quantum software package to study the torsional state probabilities for RIS bonds 4, 5, and 6.....	40
Figure 2-9: Methyl benzoate and its calculated dipole moment of 1.89 debye at 107°.....	48
Figure 2-10: Response of characteristic ratio (diamonds) and dipole moment ratio (squares) to an increase in the number of monomeric units.....	53
Figure 2-11: Response of dipole moment ratio of PET. Note that in order to achieve the target dipole moment ratio at smaller angles, the COCC trans fraction must increase.....	55
Figure 2-12: PEN RIS bond assignments.....	57
Figure 2-13: Model compound representing a portion of the PET chain symmetric about the ethylene glycol bond.....	60
Figure 2-14: Decomposed OCCO intrinsic torsion potential.....	61
Figure 2-15: Amorphous density versus ethylene glycol gauche torsion fraction for PET. The lines for each data set represent a linear fit of the data.....	64
Figure 2-16: PET (left) and PEN (right) molecular models comprised of 120 monomeric units each. The PEN model was zoomed-out to show the elongated conformation of the entire chain.....	72
Figure 3-1: Illustration of tetrahedron free volume.....	78
Figure 3-2: Tetrahedron Clustering Algorithm.....	80

Figure 3-3: Free volume distribution among tetrahedron for representative PET model.....	82
Figure 3-4: Free volume distribution among tetrahedron for representative PEN model	83
Figure 3-5: Histogram of total free volume within tetrahedra by penetrant radius for a representative PET model.....	84
Figure 3-6: Histogram of total free volume within tetrahedra by penetrant radius for a representative PEN model.....	85
Figure 3-7: Fractional free volume distribution curves for PET and PEN with 95% confidence interval error bars.....	88
Figure 3-8: Distribution of tetrahedron per cluster of o- P_s radius size for PET and PEN. Error bars represent 95 % confidence interval. Right graph is a close up view of the graph on left.....	92
Figure 3-9: Distribution of tetrahedron per cluster of O_2 radius size for PET and PEN. Error bars represent 95 % confidence interval. Right graph is a close up view of the graph on left.....	92
Figure 3-10: Cluster volume distribution for PET and PEN at O_2 size penetrant radius. Confidence limits are at 95 %	93
Figure 4-1: PNB helical /kinked structure forming irregular free volume pockets.....	97
Figure 4-2: Stereochemical configurations of PNB.....	99
Figure 4-3: Chung's comparison between simulated and experimental WAXD patterns for methyl (solid), butyl (short-long dash), and hexyl (dotted) PNB.....	100
Figure 4-4: Simulated WAXD patterns for HFA-PNB. The solid line represents a periodic model composed of 4 perfect chains and the dotted line represents 2 amorphous chains.....	101
Figure 4-5: 4 Chain perfect HFA-PNB periodic model used by Chung.....	102
Figure 4-6: 2 Chain amorphous HFA-PNB periodic model used by Chung.....	102

Figure 4-7: Experimental WAXD patterns of HFA-PNB as a function of molecular weight from 8.5×10^3 (solid line with open circles) to 4.74×10^5 (dotted line with open squares).....103

Figure 4-8: Shown on the left is the initial 40 monomer HFA-PNB chain developed by Chung for the "Perfectly Aligned" model. On the right is the same chain after MD at 700 K for 100ps. Note the elongation and more irregular structure of the second chain.....104

Figure 4-9: Simulated WAXD patterns of HFA-PNB representing various stages of chain alignment. Data was cutoff at 5 \AA^{-1} due to extraneous low 2 theta peaks.....105

Figure 5-1: Schematic of Slow Positron Beam used for PALS testings. (A: positron source; B: W-mesh moderator; C: magnetic field coils; D: filter; E: positron accelerator and electric insulator; F: correcting magnets; G: gas inlet; H: positron lifetime system for PAL; I: turbo molecular pump; J: sample; K: sample manipulator; L: cryo pump; M: Ge solid state detector; N: PAL detector)..... 110

Figure 5-2: o-Ps Lifetime data for HFA samples of MW 5000, 30000, and 100000 at various sample depths. MW are approximate and are based on Gel Permeation Chromatography..... 111

Figure 5-3: Intensity data for HFA samples of MW 5000, 30000, and 100000 at various sample depths..... 112

Figure 5-4: Fractional free volume data for HFA samples of MW 5000, 30000, and 100000 at various sample depths. Conversion from lifetime and intensity data to ffv data was performed using equations [3.1-3.3]112

Figure 5-5: Probability distribution function of o-Ps lifetimes and free volume cavity radii from HFA samples of MW 5000, 30000, and 100000 at a sample depth of 0.17 \mu m ... 113

Figure 5-6: Dissolution behavior of HFA-PNB as a function of molecular weight shown in log scale (left) and linear (right)..... 114

Figure 5-7: Single cell view of the amorphous HFA-PNB model. Note the large void areas representing free volume115

Figure 5-8: Free volume distribution among tetrahedra for amorphous HFA-PNB model.....116

Figure 5-9: Histogram of total free volume within tetrahedra by penetrant radius for amorphous HFA-PNB model.....	116
Figure 5-10: Fractional free volume distribution for amorphous HFA-PNB.....	117
Figure 5-11: Distribution of the number of tetrahedra per cluster of o- <i>Ps</i> radius size for simulated amorphous HFA-PNB.....	119
Figure 5-12: Distribution of tetrahedron per cluster of o- <i>Ps</i> radius size for simulated amorphous HFA-PNB for clusters with 10 or less tetrahedron per cluster. Note that due to the definition of a cluster it can not contain less than 2 tetrahedra.....	120
Figure 5-13: Distribution of cluster volume of o- <i>Ps</i> radius size for simulated amorphous HFA-PNB.....	121
Figure 5-14: Distribution of cluster volumes of o- <i>Ps</i> radius size for simulated amorphous HFA-PNB for clusters with volumes of 10 or less cubic angstroms	122
Figure 5-15: Simulated lifetime distribution of amorphous HFA-PNB based upon individual tetrahedron. Probability is based upon all tetrahedron in model.....	126
Figure 5-16: Simulated lifetime distribution of amorphous HFA-PNB based upon individual tetrahedron within relevant lifetime range. Probability is based upon tetrahedron in model with lifetimes greater than 1ns.....	127
Figure 5-17: Simulated lifetime distribution of amorphous HFA-PNB based upon clustered tetrahedron. Probability is based upon all clusters in model.....	128
Figure 5-18: Simulated lifetime distribution of amorphous HFA-PNB based upon clustered tetrahedron within relevant lifetime range. Probability is based upon clusters in model with lifetimes greater than 1ns.....	129
Figure 5-19: Average HFA cluster lifetime $\tau_{ell, average}$ as a function of ξ	131
Figure 5-20: Connolly Surface of amorphous HFA-PNB periodic cell. Note the large connected free volume pockets as well as the smaller isolated free volume pockets.....	132

NOMENCLATURE

Summary:

PET	Polyethylene terephthalate
PEN	Polyethylene naphthalate
RIS	Rotational Isomeric States
FTIR	Fourier Transform Infrared Spectroscopy
C_{∞}	Characteristic Ratio
D_{∞}	Dipole Moment Ratio
FFV	Fractional Free Volume
HFA-PNB	Hexafluoroalcohol substituted Polynorbornene
WAXD	Wide Angle X-ray Diffraction
o-Ps	ortho-positronium
PALS	Positron Annihilation Lifetime Spectroscopy

Chapter 1:

V_l	Polymer Liquid Specific Volume
V_g	Polymer Liquid Specific Volume
V_o	Polymer Occupied Specific Volume
SAXS	Small Angle X-ray Scattering
PNB	Polynorbornene
T_g	Glass transition temperature
$^{\circ}$	Degree
C	Celsius
T_m	Polymer melt temperature
cc	Cubic Centimeter
cm	Centimeter
m^2	Square meters
atm	Atmosphere
g	Grams
ROMP	Ring Opening Methathesis Polymerization
DVD	Digital Video Disc
H	Hamiltonian
Ψ	Wavefunction
R	Nuclei position
r	electron position
E	Total Energy
E(R)	Potential Energy
$\Theta(R)$	Wavefunction for the nuclei
DFT	Density Functional Theory
ρ	Particle density
U[ρ]	Coulombic Interaction Energy
T[ρ]	Kinetic Energy
$E_{xc}[\rho]$	Many body contributions in the total energy
F_i	Force on atom i
U	Potential Energy
m	Mass

t	Time
MD	Molecular Dynamics
m_i	Mass of atom i
r_i	Position of atom i
NVE	Constant Number of moles, Volume, and Energy ensemble
NPT	Constant Number of moles, Pressure, and Temperature ensemble
NPH	Constant Number of moles, Pressure, and Enthalpy ensemble
NVT	Constant Number of moles, Volume, and Temperature ensemble
E	Total Energy
E_{Bonded}	Energy related to bonded interactions
$E_{\text{Nonbonded}}$	Energy related to non-bonded interactions
E_{Bond}	Energy related to bonded interactions
E_{Angle}	Energy related to angles
E_{Torsion}	Energy related to torsion
$E_{\text{Inversion}}$	Energy related with one atom having single bonds with 3 atoms
$E_{\text{Crossterms}}$	Energy related to mixed term interactions
$E_{\text{Restraint}}$	Energy related to external system restraints
$E_{\text{Coulombic}}$	Energy related to coulombic interactions
$E_{\text{Dispersion}}$	Energy related to the electron dispersion effect

Chapter 2:

IPA	
NMR	Nuclear Magnetic Resonance
Å	Angstroms
s	Seconds
K	Kelvin
kcal	Kilocalorie
RMS	Root Mean Squared
NDO	Neglect Differential Overlap
CNDO	Complete Neglect Differential Overlap
INDO	Intermediate Neglect Differential Overlap
MINDO	Modified Intermediate Neglect Differential Overlap
ZINDO	Zerner's Intermediate Neglect Differential Overlap
ps	Picosecond
P	Probability
U_i	Statistical Weight Matrix
Φ	Torsion Angle
E_t	Energy of trans energy state
E_o	Energy of reference energy state
E_g	Energy of reference energy state
k	Boltzman's constant
$\langle r_o^2 \rangle$	Mean squared end to end distance
$\langle s_o^2 \rangle$	Mean squared radius of gyration
Z	Configurational partition function
n	Number of skeletal bonds
u	Respective component of the statistical weight matrix
I_A	Identity matrix
\otimes	Direct product
θ_i	Bond angle i
length _i	Bond Length i

γ	Statistical weight cis probability for PET RIS bond 2
σ_x	Statistical weight gauche probability for PET RIS bond 4/6
σ_η	Statistical weight gauche probability for PET RIS bond 5
$\omega_{\eta x}$	Statistical weight probability of opposite gauche states for PET RIS bonds 4,5 and 6
l	Average length of backbone bonds
g	Gauche torsional state
D	Debye
N_D	Number of monomeric dipoles
m_0	Magnitude of monomeric dipole
DMT	Dimethyl Terephthalate
SCF	Self Consistent Field
MP2	Moller Plesset correlation correction
PCFF	Polymer Consistent Force Field
$k_{\phi,j}$	j fold Intrinsic torsion potential coefficient
δ_i	Solubility parameter
ΔU_i^v	Potential Energy change upon vaporization of a saturated liquid to the ideal gas state
V_i^L	Liquid molar volume
$\Delta U_{simulated}$	Potential energy difference between an isolated and a bulk simulated model
V_{system}	System volume
N_A	Avogadro's number
MPa	Mega pascal
ns	Nanoseconds
$E_{isolated\ Chain}$	Potential energy of an isolated simulated model
E_{Bulk}	Potential energy of a bulk simulated model

Chapter 3:

τ_3	ortho-positronium lifetime
I_3	ortho-positronium intensity
τ_{sphere}	ortho-positronium lifetime based on spherical assumption
R	Radius of spherical free volume cavity
V_f	Volume of spherical free volume cavity
f	Fractional free volume
C	Constant
π	Pi
$V_{tetrahedron}$	Volume of Delaunay Tetrahedra
$V_{occupied}$	Volume occupied by atomic radii
$V_{overlap}$	Volume correction for double and triple atomic overlaps
$R_{penetrant}$	Radius of spherical penetrant associated with tetrahedra
R	Radius of spherical penetrant associated with tetrahedra
$R_{average}$	Average atomic radius of each atom

\AA^3	Cubic angstroms
\bar{r}	Mean Radius
σ	Standard deviation
γ_3	Skewness
γ_4	Kurtosis
$V(r_i)$	Volume associated with tetrahedra with radius r_i

Chapter 4:

nm	Nanometers
$\tau_{ell.}$	Lifetime of an elliptical free volume cavity
ε	Eccentricity
a	Major axis of ellipsoid
b	Minor axis of ellipsoid

Chapter 5:

M_w	Molecular Weight
keV	Kiloelectron volts
z	Sample depth
ρ	Sample density in grams/cubic centimeters
E	Incident energy
cm^3	Cubic centimeters
μm	Micrometers
PDF	Probability Distribution Function
S_{ij}	Radius of gyration Tensor
$\langle x_0^2 \rangle$	Largest eigenvalue of the radius of gyration tensor
$\langle y_0^2 \rangle$	Medium eigenvalue of the radius of gyration tensor
$\langle z_0^2 \rangle$	Smallest eigenvalue of the radius of gyration tensor
x	Atomic coordinates in angstroms
x_{cm}	Atomic coordinates of center of mass in angstroms
$\tau_{elliptical}$	Lifetime of an elliptical free volume cluster
$\tau_{ell. average}$	Average lifetime of an elliptical free volume cluster
$Volume_{total}$	Cumulative cluster free volume
$Volume_{(i)}$	Cluster i free volume
$\tau_{elliptical.(i)}$	Lifetime of an elliptical free volume cluster i
ξ	Probability of cluster sampling

SUMMARY

Free volume and free volume distribution have long been used to explain differences in the gas transport properties of polymeric materials. However, only a few experimental techniques allow a comprehensive evaluation of polymeric void space. Through the use of computer simulations, Delaunay Tessellation, and Clustering Analysis, the free volume was characterized of two polyester systems used for beverage packaging and polynorbornene, a unique polymer with possible applications in both microelectronic fabrication and membrane separations.

Molecular models of Polyethylene Terephthalate (PET) and Polyethylene Naphthalate (PEN) were developed and their free volume characterized. To aid in the creation of accurate atomistic simulations, a new Rotational Isomeric States (RIS) model was created for PET and PEN and was used to create accurate initial conformations of the polymers. The RIS model was parameterized using several experimental values as guides to predict the correct conformation. Fourier Transform Infrared Spectroscopy (FTIR), characteristic ratio (C_{∞}) measurements and dipole moment ratio measurements (D_{∞}) were used to determine the accuracy of the RIS model.

Delaunay Tessellation was used to calculate the fractional free volume (FFV) of both PET and PEN models. It was hypothesized that differences in the FFV distributions could be used to explain the higher experimental O_2 solubility in PEN relative to PET. The analysis showed that there was no statistical difference between the FFV distributions for O_2 sized penetrants.

Clustering analysis was performed based upon the tetrahedra formed in Delaunay Tessellation calculation to examine the connectivity of free volume pockets and the development of clusters of free volume involving several tetrahedra. These

results show that there is a statistically larger number of small (containing less than 10 tetrahedra/cluster and between 20-30 Å³ in volume) clusters in PEN. It is this difference in small clusters which provides for the 30% higher O₂ solubility in PEN.

Molecular models of bis-trifluoromethyl carbinol or Hexafluoroalcohol Substituted Polynorbornene (HFA-PNB) were also performed. For the 2,3-erythro di-isotactic stereoisomer of HFA-PNB, it was found that the molecular weight trend seen in the experimental wide angle x-ray diffraction (WAXD) pattern could be simulated with molecular dynamics simulations on a small molecular weight model. This indicated that the intramolecular alignment of the chains were responsible for the property change observed in the WAXD results.

The free volume of a representative high molecular weight amorphous model of HFA-PNB was also characterized in order to examine the shape of the free volume cavities and to use that information to draw correlations with the mean lifetime of ortho-positronium (o-Ps) from Positron Annihilation Lifetime Spectroscopy (PALS). Delaunay Tessellation and clustering analysis indicated that the free volume clusters in high molecular weight HFA-PNB are slightly non-spherical. Correcting lifetimes for the somewhat non-spherical shape of these free volume clusters was insufficient to reproduce experimentally measured positron annihilation lifetimes because the clusters contained many tortuous connections within the clusters. Inclusion of this connectivity information does produce a more accurate estimate of the measured life times. This indicates that the o-Ps does sample many tetrahedra in these clusters, but does not freely sample every section of these clusters.

CHAPTER I

INTRODUCTION

1.1 Motivation and Goals

Fractional free volume is important in understanding gas transport through polymeric films. The amount and distribution of fractional free volume will dictate how gaseous molecules will be transported through the material. So, the free volume will determine the usefulness of a polymer for a barrier or membrane application. A polymer's free volume is the difference between the specific polymer volume in the glassy or rubbery states and the volume associated with a crystalline solid at the same temperature (1). Molecular chain motions and chemical structure will affect fractional free volume and its distribution within a polymer (2).

One way to visualize this notion is through the diagram demonstrated by Figure 1-1 that was developed by Simha and Boyer (3) in which V_l and V_g represent the specific volume of a polymer in the liquid and glassy states respectively, and V_o represents the volume occupied by the atoms in the polymer chain with the area between the curves representing the free volume.

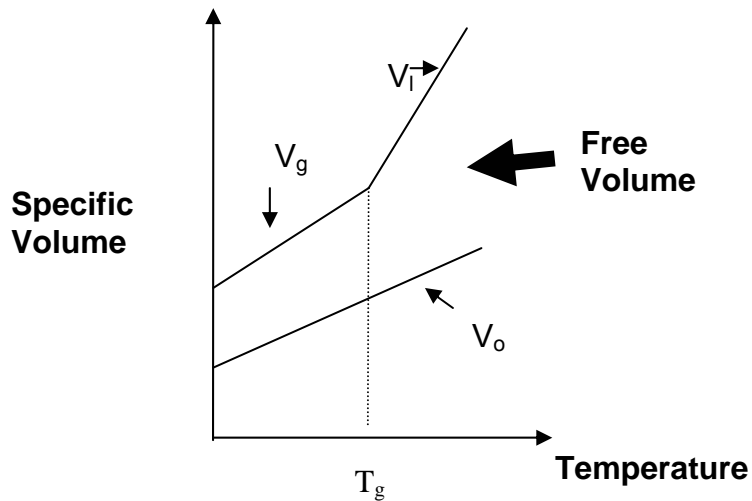


Figure 1-1: Free volume curve

Free volume is usually determined from group additivity correlations (4) or it must be inferred indirectly from experimental measurements such as Positron Annihilation Lifetime Spectroscopy (PALS) (5), Small Angle X-Ray Scattering (SAXS) (6), spin probe methods (7), photochromic probes (8), and inverse gas chromatography (9). Of these methods PALS gives the most detailed characterization of free volume, but it is difficult to produce the free volume distribution. It is this distribution of free volume that is of interest in understanding the separation of gaseous mixtures, since it will dictate which molecules are excluded and which molecules may have an enhanced solubility based on their ability to condense in the free volume pockets. While two polymers may have the same total free volume, they may have vastly differing transport properties based upon the free volume distribution. As illustrated in Figure 1-2, these two hypothetical polymers will have very different uses due to the different availability of free volume to particular penetrants and the connectivity of that free volume.

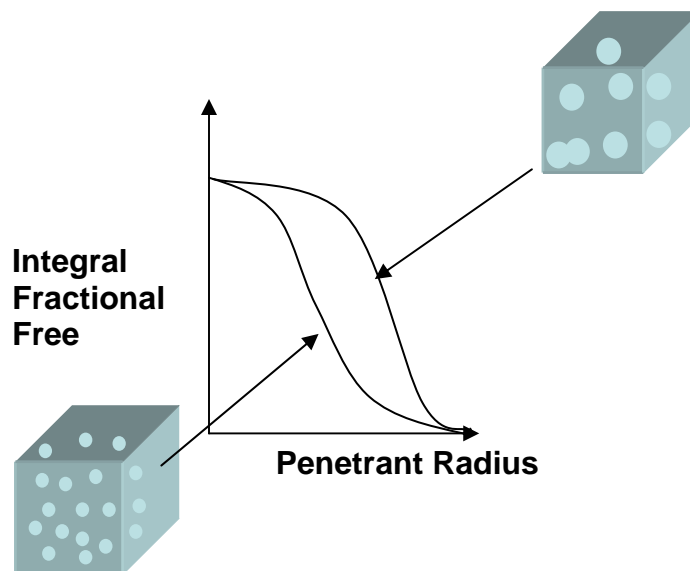


Figure 1-2: Two hypothetical polymers with the same total fractional free volume but a different free volume distribution

This distribution will be influenced by stereochemistry, rigidity of the polymeric backbone, and side groups. It is a connection between structure and the free volume distribution which we seek to elucidate in this study.

The goal of this work is to directly extract the amount and distribution of free volume in an amorphous bulk polymer. This will be achieved through the development of accurate molecular models of a polymer. The molecular structure will then be geometrically analyzed by Delaunay Tessellation to estimate the distribution of the free volume. Delaunay Tessellation analysis will be explained in Chapter 3. These distributions will then be compared to experimental gas transport trends. Additionally, these distributions will facilitate a better interpretation of PALS data which is currently hindered by assumptions made to correlate raw data into free volume estimates. Overall, this study will allow for the direct correlation of structural chemical changes in a polymer with its effect on free volume. With the increasing ability to control polymer chemistry

and structure through novel catalytic systems, the proliferation of molecular level insight will become key in tailoring polymeric systems for specific uses.

In order to study the effects of molecular structure on free volume distribution two amorphous glassy polymer systems have been chosen for characterization. Polyethylene terephthalate (PET) and polynorbornene (PNB) are commercially important polymers for applications ranging from barrier materials to gas separations.

1.2 Polyethylene Terphthalate

Polyethylene Terephthalate (PET) has become an important polymer in the past few decades (Figure 1-3). PET is a thermoplastic polyester and has wide ranging uses from clothing to packaging. (10)

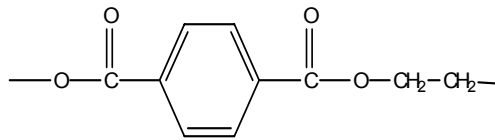


Figure 1-3: PET repeat unit

PET is used extensively in food packaging for ovenable food trays and primarily in bottles for beverage packaging, and numerous other food and personal care products (11). In 1997, the North American production of PET was over 1.8 billion pounds for plastic bottles alone (9). PET's widespread use as a food packaging material is due to its relatively good oxygen barrier performance and cost efficiency (10), however, there are emerging applications for which PET's oxygen permeability is too high. One such application is the single layer plastic beer bottle. Contemplated since the 1960's, a

plastic beer bottle offers superior break resistance, lower shipping weight, and lower materials cost (12). Currently, there are some plastic beer bottles in the marketplace, but they are often multilayer structures or contain an oxygen scavenging layer. These bottles are often very expensive and difficult to recycle. One such material which meets the oxygen permeability requirements of a single layer structure for beer is polyethylene naphthalate (PEN) (Figure 1-4). However, PEN is cost prohibitive due to the expensive monomer dimethyl-2,6-naphthalenedicarboxylate.

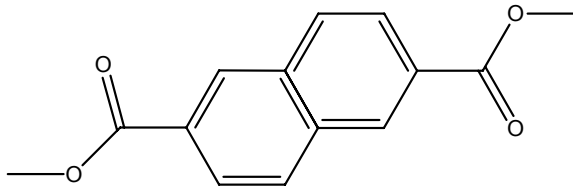


Figure 1-4: 2,6 PEN repeat unit

As shown in Table 1-1, the structurally similar PET and PEN have oxygen permeabilities which differ by a factor 3. Although differences in diffusivity are primarily responsible for the differences in permeability, there are some differences between the systems in solubility. Since chemical interactions with oxygen penetrant molecules will be very similar for both polymers, the differences in total free volume and its distribution are attributed to the differences in O₂ solubility. Therefore it is hypothesized that:

Table 1-1: Comparison of selected PET and PEN properties

<u>Property</u>	<u>PET</u>	<u>PEN</u>
Glass Transition Temperature, T_g ($^{\circ}\text{C}$) (12)	76	119
Crystalline Melting Temperature, T_m ($^{\circ}\text{C}$) (12)	255	265
O_2 Permeability ($\text{cc cm/m}^2 \text{ day atm}$)(13)	0.469	0.157
Amorphous Density (g/cc)	1.3350	1.3316

Hypothesis 1: A comparison of free volume and free volume distribution developed from accurate molecular models of PET and PEN should predict a higher fractional free volume in PEN for the same gaseous penetrant.

The validation of this solubility trend in PET versus PEN may lead to the development of lower cost PET derivatives with reduced permeabilities making them more suitable for new barrier applications.

1.3 Polynorbornene

Polynorbornene (PNB) is one of a series of new cyclic olefin polymers that have been synthesized using homogenous catalyst systems that result in a vinyl-like polymerization (15). In contrast to the Ring Opening Metathesis Polymerization (ROMP), these metallocene (16) and metal-coordinated catalysts (17) allow polymerizations in which the bicycloheptane is retained in the backbone resulting in a regular structure and alternating non-rotatable bonds as shown in Figure 1-5. All work being considered in this proposal is based on work with structures produced with metallocene and metal-coordinated catalysts.

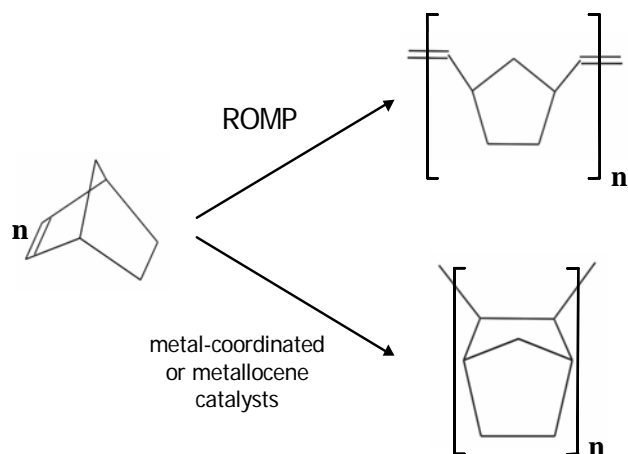


Figure 1-5: PNB by various polymerization routes

The unique structure results in properties of PNB (18) that can be useful in applications such as microelectronics fabrication (19), membrane separation (20, 21), pharmaceutical packaging, contact lenses, Digital Video Disks (DVDs) and high impact plastics (15). Our current interest in PNB concerns its ultra high free volume. This large amount of fractional free volume results in high permeability coefficients, which allow high membrane throughput. At the same time, PNB belongs to a class of polymers, consisting mainly of polyacetylenes (22) (Figure 1-6) which have high selectivities for condensable components over noncondensable components in gaseous streams (23). This ability makes PNB an attractive candidate material for separating small amounts of organics from non-condensable gas streams in environmental applications like hydrogen refinement.

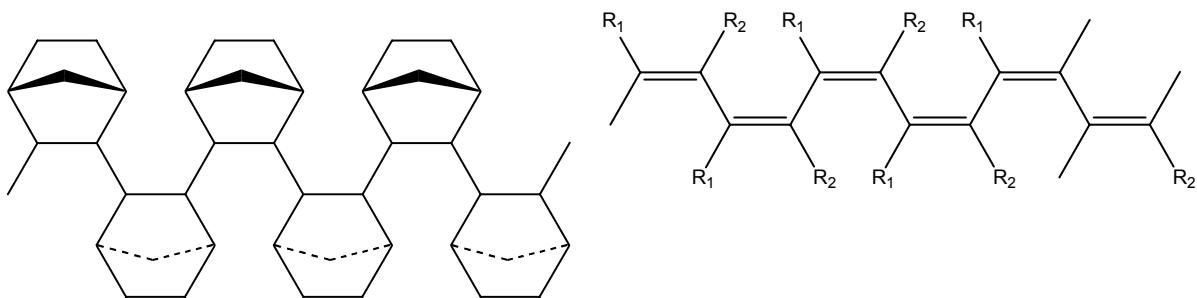


Figure 1-6: Erythro di-isotactic isomer of 2,3 poly(norbornene) (left) and the cis-transoid configuration of substituted poly(acetylene). Note that each backbone structure has alternating non-rotatable bonds in common.

PNB is capable of forming two stereoisomers based upon the catalytic system used in the polymerization (Figure 1-7). Ahmed et al. found that PNB produced with palladium based catalysts have a measured scaling of intrinsic molecular weight that was consistent with 2,3-erythro di-isotactic polynorborne, in which the bridgehead carbons point in alternating directions. Nickel based catalytic systems form a polymer which is approximately 75% 2,3-erythro di-isotactic and 25% 2,3-erythro di-syndiotactic, with the bridgehead carbons pointing in the same direction (24,25). All the proposed work presented in this proposal will be based on 2,3-erythro di-isotactic PNB.

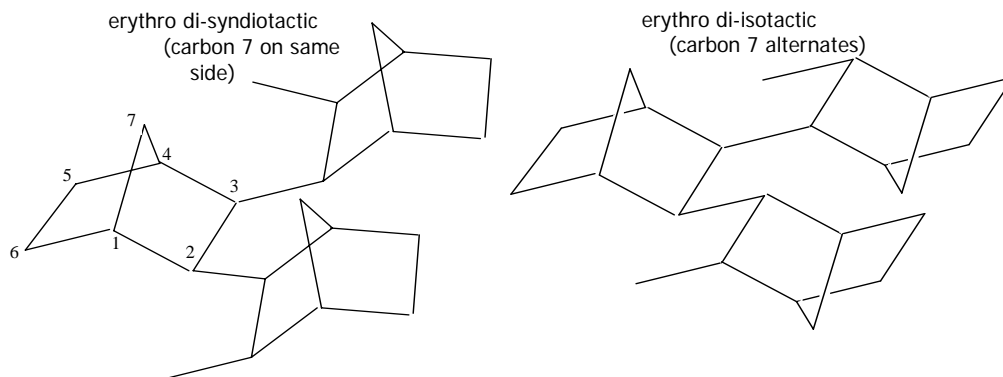


Figure 1-7: Stereochemical configurations of erythro (exo-exo) PNB

The described selectivity behavior of PNB has been attributed to differences in the solubility selectivity of gaseous components in this system (26). It is believed that the condensable components fill free volume pockets with a condensed phase and exclude the non-condensable components. This type of behavior is believed to require large pockets of free volume. Therefore, a free volume characterization of a series of PNB derivatives will allow a greater understanding of the structure-property relationships for this class of polymers.

One of the reasons that PNB is believed to exhibit such unusual gas transport properties is due to its unique structure. Early modeling work performed by Ahmed et al. (24) and Chung et al. (27) has suggested that PNB has a helical structure which is periodically interrupted by a kink in the backbone. The probability of a kink forming is 0.2% (27). At lower molecular weights the fraction of kinks will be very low and chain packing is more efficient resulting in lower free volume. Contrast this with the higher molecular weight region where the fraction of kinks is much higher and ordered packing is hindered resulting in larger pockets of free volume. As part of the analysis of PNB's structure – property relationships we also aim to prove that :

Hypothesis 2: The microvoids found in PNB are highly nonspherical.

The nonspherical nature of these microvoids is a source of error when one attempts to determine the free volume distribution from PALS data. This is due to the common use of a spherical cavity assumption (29) used to calculate free volume from PALS lifetime data. Given the helical kink conformation of PNB, we hypothesize its free volume elements are elongated and are not accurately represented by the spherical shape. By using a more representative ellipsoidal shape which can be found through a Delaunay Tessellation of the PNB, the free volume calculated from PALS data should be more representative of the free volume distribution found in the structure.

1.4 Molecular Modeling Introduction

In order to model a macromolecule, one must have a reasonably complete description of the molecular system. Currently, the most detailed description comes from quantum mechanics in the form of the time independent Schrödinger equation

$$H\Psi(R, r) = E\Psi(R, r) \quad [1.1]$$

where H is the Hamiltonian, Ψ is the wavefunction (which is a function of R the nuclei positions, and r the electrons' positions), and E is the total energy. In order to begin to approach a solvable form of the Schrödinger equation, the first approximation made is the Born - Oppenheimer Approximation. This reduces the system into electronic and nuclear parts. This approximation assumes that the motion of the electrons is decoupled from that of the nuclei due to the relative differences in mass and velocity (30). The resulting electronic form of the Schrödinger equation is

$$H\Psi(r; R) = E(R)\Psi(r; R) \quad [1.2]$$

Where Ψ is only dependent upon the position of the nuclei and $E(R)$ is defined as the potential energy surface. The nuclear form of the Schrödinger equation is

$$H\Theta(R) = E\Theta(R) \quad [1.3]$$

where $\Theta(R)$ is the wavefunction for the nuclei.

Equation [1.2] can be solved for electrons using first principle or *ab initio* methods. One such method is Hartree-Fock, which assumes that Ψ can be described as a product of molecular orbitals. Each molecular orbital is itself a linear combination of atomic orbitals. To select the atomic orbitals, a tool called a basis set is used. In a basis set the atomic orbitals are described by atom-centered Gaussian functions.

In order to decrease the computational cost of the Hartree-Fock method, the Semi-empirical approach was employed. This approach involves using experimental parameters such as atomic ionization potentials in the electron integrals necessary to compute the Hartree-Fock energy. This significantly reduces the computation time needed for calculations but the applicability is limited by the Semi-Empirical parameter set chosen (31).

Another *ab initio* level method is Density Functional Theory (DFT). The key to this approach is that the energy of the system can be described by charge density instead of using electron wavefunctions. This can be generalized in the equation

$$E_t[\rho] = T[\rho] + U[\rho] + E_{xc}[\rho] \quad [1.4]$$

Where $T[\rho]$ is the kinetic energy of a system of noninteracting particles of density ρ , U is the energy due to Coulombic interactions, and $E_{xc}[\rho]$ includes the many body contributions to the total energy. The system is solved by minimizing the total energy with respect to the charge density. DFT separates itself from the Hartree-Fock method in that DFT includes electron to electron correlation through the empirical exchange function or E_{xc} whereas Hartree-Fock includes only an average electron charge

distribution that is seen by each individual electron (32). There are also other methods that account for electron correlation such as Moller-Plesset Perturbation Theory and Configuration Interaction (32).

ab initio, semi-empirical, and DFT methods were used in this work for the characterization of PET, for the fitting of the rotational isomeric states model, and to reparameterize the force field used for energy relaxation of structures.

The next level of describing the molecular system employs the assumption that quantum effects are negligible due to the relative mass of the nuclei as compared to the electron. This allows us to move from the Schrödinger equation to Newton's equation of motion

$$F_i = -\frac{dU}{dR} = m \frac{d^2 R}{dt^2} \quad [1.5]$$

where F_i is force, U is potential energy, m is the nucleus mass, R is the position of the nucleus and t is time. The integration of this equation is known as molecular dynamics (MD). Most of the simulation work presented will use this approach for polymer modeling.

1.5 Molecular Dynamics

The numerical integration of Equation [1.5] comprises the process known as molecular dynamics. Writing Equation [1.5] for a system results in

$$F_i = -\nabla_i U = m_i \frac{d^2 r_i}{dt^2} \quad [1.6]$$

where F_i is the force exerted on atom i , m_i is the mass of atom i , and r_i is the position of atom i . Using a potential energy function called a force field (often parameterized by *ab initio* calculations described in the previous section), the integrated equation is used to calculate the positions and velocities of all atoms in the system over a particular time.

Because of the kinetic aspect of the molecular dynamic simulation, MD is very adept at sampling the local phase space of a system and locating various lower energy states in the vicinity of the initial state.

By using statistical mechanics, microscopic information calculated via molecular dynamics can be used to define macroscopic quantities such as internal energy, temperature, pressure, and enthalpy. Using this link, one can define particular statistical mechanical ensembles for a simulation. These ensembles include constant number, volume, and energy (NVE); constant number, pressure, and temperature (NPT); constant number, pressure, and enthalpy (NPH); and constant number, volume, and temperature (NVT). Associated with each constant property is a controller algorithm used to maintain the property value (33).

1.6 Molecular Mechanics

Molecular Mechanics is the case of molecular dynamics in which the temperature is 0 K or there is no kinetic energy in the system. In this methodology the potential energy of the system is minimized with respect to the atomic positions. Using the aforementioned force field, the energy of the system is calculated and atomic positions are shifted until a minimum energy is achieved. The application of the force field allows the potential energy of the system to be represented by one explicit function. The negative gradient of the potential energy or forces in the system is used to guide the minimization process. This is carried out using a number of well known mathematical algorithms such as steepest decent, conjugant gradient, and Newton Raphson, (34) each having their own intricacies in computational cost and stage of the minimization in which they are most effective.

1.7 Force Field

The heart of both the molecular mechanics and the molecular dynamics processes is the force field. A force field is a set of equations (often parameterized using quantum level calculations) that describe the potential energy of a molecular system. Often force fields are limited in the systems to which they are applicable due parameters which are specific to only 1 type of system or which are too generic to be of use (35).

Most force fields contain energy contributions for both bonded and non-bonded interactions as expressed in

$$E = E_{Bonded} + E_{Nonbonded} \quad [1.7]$$

where E_{Bonded} is the energy related to the bonded interactions and $E_{Nonbonded}$ is related to the nonbonded interactions. These energies are subdivided into more specific interactions.

The bonded interactions are defined by

$$E_{Bonded} = E_{Bond} + E_{Angle} + E_{Torsion} + E_{Inversion} + E_{Crossterms} + E_{Restraints} \quad [1.8]$$

where E_{Bond} is bond stretching, E_{Angle} is angle bending, $E_{Torsion}$ is the intrinsic torsion potential, $E_{Inversion}$ is the energy associated with one atom having three single bonds with three other atoms, $E_{Crossterms}$ is the energy associated with mixed term interactions such as $Bond_1$ - $Bond_2$ or $Bond_1$ - $Angle_1$ - $Bond_2$ and $E_{Restraint}$ is the energy associated with an restraint derived externally to the system.

The non-bonded interactions are defined by

$$E = E_{Coulombic} + E_{Dispersion} \quad [1.9]$$

where $E_{Coulombic}$ is coulombic interactions, and $E_{Dispersion}$ is the electron dispersion effect, typically modeled by van der Waals interactions.

Each of the specified energy terms has a specific form. For example, the bond stretching and angle bending terms are quadratic harmonic functions. The selected forms are

sometimes specific to a particular forcefield, but can also be parameterized for particular polymers.

1.8 Polymer Glasses

Polymer glasses are viewed as having a random or amorphous structure. This means that there is no long range order in these materials. In the molecular modeling area most of the methods for forming representations of these systems are based upon the work of Theodorou and Suter (36). The modeling framework used in this work is summarized below

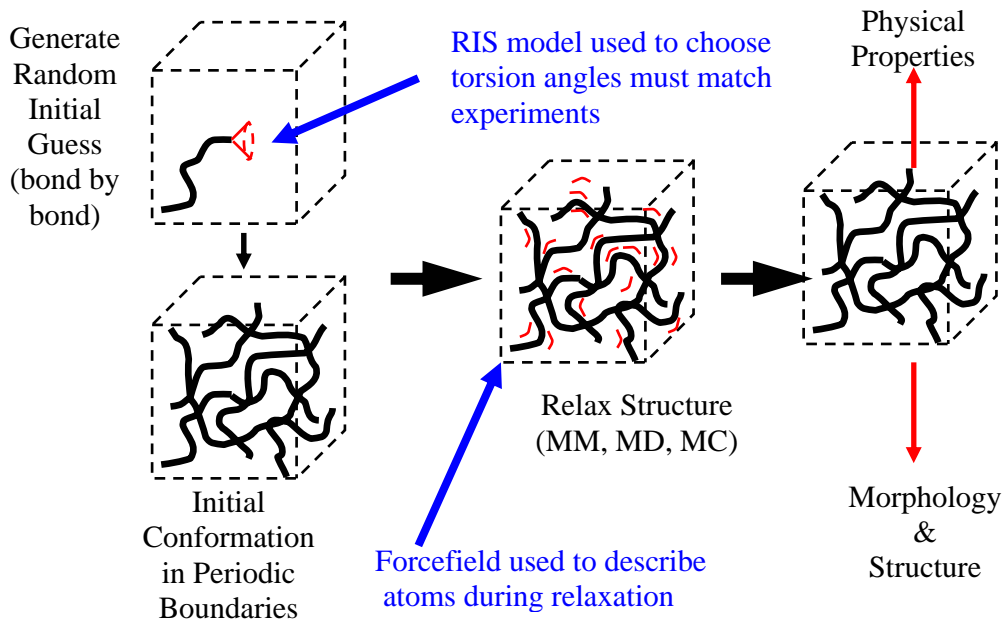


Figure 1-8: Polymer glass modeling protocol

Using the algorithm similar to that developed by Theodorou and Suter the polymer is grown inside periodic boundary conditions which mimic the bulk view of the polymer. The structure for an amorphous glass is random; however the backbone polymer torsions are selected according to a Rotational Isomeric States (RIS) model (37). The model is then relaxed using various methods such as molecular mechanics or molecular dynamics and one can draw structure property correlations. This method is limited since it can only be used as is for truly amorphous systems. If the system has any order but is not crystalline (often referred to as having intermediate order) (38), then either the RIS model must incorporate that structure or the relaxation technique used must be rigorous enough to sample enough conformations to find the semi-ordered low energy state. Polynorbornene falls into the latter class of polymers while the polyesters fall into the former.

REFERENCES

1. D. Paul; Y. Yampol'ski, Polymeric Gas Separation Membranes, CRC Press, London, 1994
2. D.Van Krevelen, *Properties of Polymers-Correlation with Chemical Structure*. p 41,1972
3. A. Bondi, *Physical Properties of Molecular Crystals, Liquids, and Glasses*, 1968
4. R. Simha; F.Boyer, *Journal of Chemical Physics*, V37, pp 1003, 1962
5. D. Shrader; Y. Jean, Positron and Positronium Chemistry, Elsevier, Amsterdam, 1988
6. J. Bartos; J. Mueller; J. Wendorff, *Polymer*, V31(9), pp 1678-1684, 1990
7. A. Wasserman; A. Kovarskii, Spin Probes and Labels in Physical Chemistry of Polymers, Nauka, Moscow, 1986
8. J. Royal; J. Torkelson, *Macromolecules*, V23(14), pp 3536-3538, 1990
9. Y. Yampolskii; N. Kaliuzhnyi; S. Durgar'yan, *Macromolecules*, V19, pp 846-850
10. D. Mastio, *Plastics World*, V55, p 59, 1997
11. <http://www.epa.gov>- Technical website for Air pollution Information, PET process overview.
12. A. Brody, *Food Technology*, V52, p 32, 1998
13. R. Po; E. Occhiello; G. Giannotta; L. Pelosini; L. Abis, *Polymers for Advanced Technologies*, V7, p 365, 1996
14. Eric Baer and Anne Hiltner Barrier Research Group at Case Western Reserve University
15. J. Schut, *Plastics Technology*, March 2000
16. M. Arndt; R. Engehausen; W. Kaminsky; K. Zoumis, *Journal of Molecular Catalysis A: Chemistry*, V101(3), 1995
17. B. Goodall; D. Barnes; G. Benedikt; L. McIntosh; L. Rhodes, *Polymeric Materials Science and Engineering*, V76 pp 56-57, 1997
18. S. Ahmed; P. Kohl; P. Ludovice, *Computational and Theoretical Polymer Science*, V10 (1,2), pp 221-233, 1997

19. H. Ito; G. Wallraff; N. Fender; P. Brock; W. Hinsberg; A. Mahorowala; C. Larson; H. Truong; G. Breyta; R. Allen, *Journal of Vacuum Science and Technology, B: Microelectronics Nanometer Structure*, V 19(6), pp 2678-2684, 2001
20. S. Thrasher, "Polymeric Membranes for Organic Vapor Recovery," Ph.D. Thesis, Georgia Institute of Technology, 1998
21. B. Wilks; W.Chung; P. Ludovice; M. Rezac; P. Meakin; A. Hill, *Journal of Polymer Science, Part B: Polymer Physics*, V41 (18) , pp2185-2199, 2002
22. K. Nagai; T. Masuda; T. Nakagawa; B. Freeman; I. Pinnau, *Progress in Polymer Science*, V26, pp 721-798, 2001
23. I. Pinnau; L. Toy, *Journal of Membrane Science*, V116, pp 199-209, 1996
24. S. Ahmed; S. Bidstrup; P. Kohl; P. Ludovice, *Journal of Physical Chemistry*, V102(49), pp 9783-9790, 1998
25. B. Goodall; G. Benedikt; L. McIntosh; D. Banres; L. Rhodes, International Patent WO95/14048,1995
26. B. Freeman; I Pinnau, *Trends in Polymers*, V5(5), pp 167-173, 1997
27. W. Chung; P. Ludovice, Manuscript in Preparation
28. B. Wilks, "Free Volume and Free Volume Distribution Impact on Transport Properties in Amorphous Glassy Polymers," Ph.D. Thesis, Georgia Institute of Technology, 2002
29. S. Tao, *Journal of Chemical Physics*, V56, p5499, 1972
30. A. Leach, Molecular Modeling Principles and Applications, Prentice Hall, New York, p35, 2001
31. A. Leach, Molecular Modeling Principles and Applications, Prentice Hall, New York, p86, 2001
32. A. Leach, Molecular Modeling Principles and Applications, Prentice Hall, New York, p128, 2001
33. M. Allen; D. Tildesley, Computer Simulation of Liquids, Oxford University, New York, pp 33, 1987
34. A. Leach, Molecular Modeling Principles and Applications, Prentice Hall, New York, p252, 2001
35. Accelrys Inc., Cerius² Users Guide-Forcefield Based Simulations, San Diego, CA, 1997
36. D. Theodorou and U. Suter, *Polymer Preprints Division of Polymer Chemistry American Chemical Society*, V25(1), p180, 1984

37. P. Flory, Statistical Mechanics of Chain Molecules, New York, 1969
38. J. Van Order; P. Ludovice, *Annual Technical Conference - Society of Plastics Engineers (56th Annual)*, V2, pp 1716-1719

CHAPTER II

POLYESTER MODELING

The goal of this work is to characterize the static free volume and its distribution in amorphous PET and PEN below the T_g of these materials. This study will not address differences in gaseous transport properties related to dynamic chain motions. Due to the similar chemical nature of PET and PEN, our hypothesis for this research is:

Hypothesis 1: A comparison of free volume and free volume distribution developed from accurate molecular models of PET and PEN should predict the higher fractional free volume found in PEN for the same gaseous penetrant.

In order to test this hypothesis, the specific tasks to be carried out are:

1. Investigate the lower ethylene glycol trans fraction found experimentally in PET in comparison to the conformations simulated by Lyons (1) which is believed to be a possible source of inaccuracy in those models. A combination of quantum calculations, molecular mechanics, and dynamics will be used.
2. Develop a new Rotational Isomeric States (RIS) model for PET through quantum calculations which will allow the development of an accurate initial conformation of the polymer.
3. Use the aforementioned RIS model to simulate accurate bulk structures of PET and PEN which will be validated by experimental data such as

solubility parameters, Fourier Transform Infrared Spectra (FTIR), and Wide Angle X-ray Diffraction (WAXD) patterns.

4. Analyze these simulated structures using Delaunay Tessellation to develop free volume distributions which will be compared to experimental barrier properties for PET/PEN. (This section of the work will be discussed in Chapter 3)

2.1 PET-Previous Experimental and Simulated Work

Previous work has been performed with the aim of characterizing the free volume of PET through the use of molecular modeling. Lyons et al. (1) produced molecular models of PET, PEN, PET-co-PEN (25%, 50%), and PET-co-IPA (2.5%, 10%). These models were validated by comparing the simulated solubility parameters and WAXD patterns to experimental values. The solubility parameter is a measure of the cohesive interactions in a material. Lyons found reasonable fits of the solubility parameters of PET and PEN with 2% and 5% errors, respectively. He also was able to reproduce the broad amorphous halo seen in PET's and PEN's WAXD patterns.

Lyons also checked the models for the Trans/Gauche torsional content of the ethylene glycol linkage of amorphous PET. Experimental values of the trans content measured by 2D-NMR are 14 ± 5 % (2). However, the thermal history of the material and the experimental method used will strongly affect this value (3). The RIS model used to create the initial configuration of PET developed by Flory yields a trans content of 35% (4). Lyons built a bulk polymer model in a periodic boundary cell and then relaxed it using molecular mechanics. The models produced contained a trans content of 43%. Therefore, these models do not accurately represent the true structure of PET and needed refinement.

Free volume characterization of the models produced by Lyons was performed with both a Stochastic Monte Carlo Sampling method (5) and the Deterministic Delaunay Tessellation (6) method. The stochastic model randomly grew spheres in the polymeric structure. The distribution of these spheres gave an estimate of the free volume distribution. The Delaunay Tessellation method tiled the spaces between the atoms into tetrahedrons, which could then be used to derive a free volume distribution. While the stochastic method generated errors due to convergence limitations, the Delaunay Tessellation approach develops errors at small penetrant radii due to the ignoring of multiple atomic overlaps. However, both methods give the same results for the large radii of interest for gaseous penetrants. Lyons found that there were insignificant differences between the total free volumes or distributions for PET and PEN, Figure 2-1.

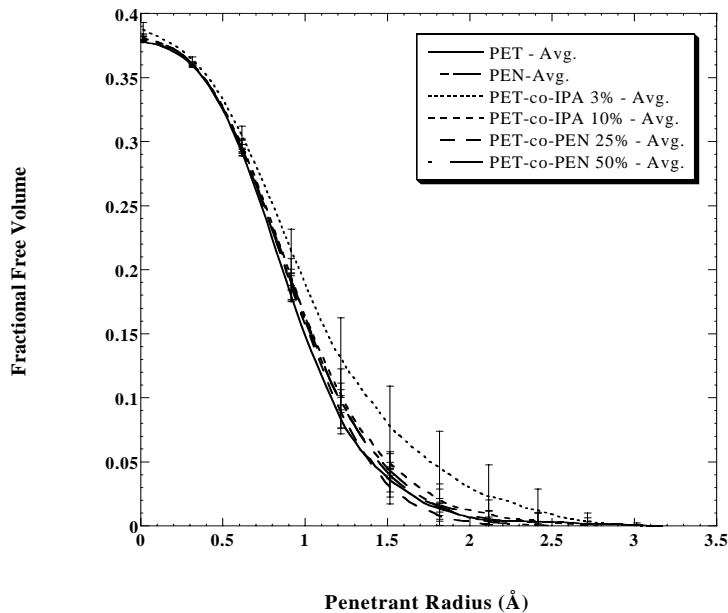


Figure 2-1: Lyon's free volume analysis for PET, PEN and selected copolymers. Note that there is no significant difference in the curves

This did not correlate with the experimental solubility data for amorphous samples of the polymer. As shown in the experimental barrier data in Figure 2-2, the solubility of oxygen in PET is notably smaller than in PEN. However due to the concerns dealing with the accuracy of the model, particularly the trans/gauche ratio of the ethylene glycol bond, no concrete conclusions were made. This represents the starting point for the work contained within this thesis.

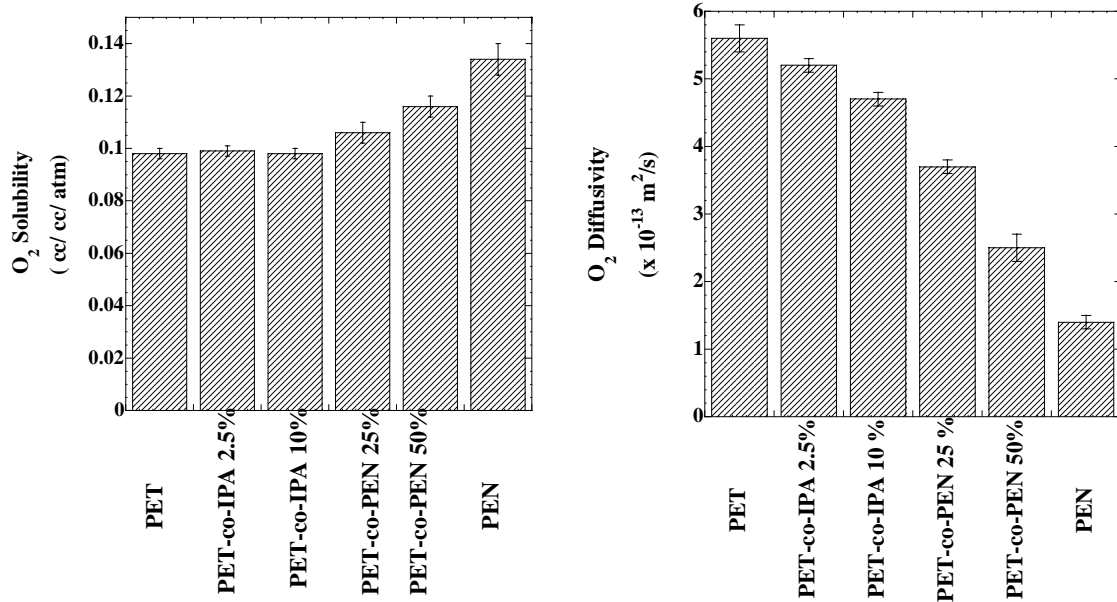


Figure 2-2: Experimental barrier data obtained from Dr. Eric Baer and Dr. Anne Hiltner’s Barrier Research Group at Case Western Reserve University.

2.2 Verification of the Ethylene Glycol Trans/Gauche Fraction in PET

The first task in this work was to verify that indeed the models created by Lyons were inaccurate. This meant verifying the ethylene glycol bond’s torsional probability. This section will explore the origins of this bond’s low trans fraction conformation.

In order to validate the experimental values of the torsional state probabilities of the ethylene glycol bond, *ab-initio*, semi-empirical, molecular dynamics (300 K), and molecular mechanical (0 K) calculations were performed on an isolated ethylene glycol molecule using Hyperchem molecular modeling software. Using a Boltzmann factor for the energies of the trans and gauche torsional states found in PET, it has been calculated that for PET to have a trans fraction of 14%, the energy difference with the gauche states must be approximately 0.8 kcal/mol.

2.2-1 *ab – initio* Calculations

To calculate the energy difference between the torsional states of the ethylene glycol bond (OCCO), geometry optimizations of an isolated ethylene glycol molecule (Figure 2-3) were performed.

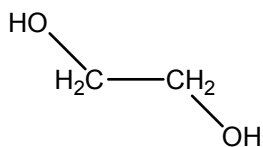


Figure 2-3: Isolated ethylene glycol molecule used in *ab -initio*, semi-empirical, molecular mechanics and molecular dynamics work

Molecules of ethylene glycol were created with the OCCO torsion in either the trans (180°) or gauche (65°) local minimum conformation. All other bond lengths, angles, and torsions were defined by an initial energy minimization of the structure using the default Hyperchem forcefield, MM+. An unconstrained geometry optimization was then performed on each structure. Using the default Polak-Ribiere minimization algorithm (7), the optimization continued until the Root Mean Square (RMS) energy gradient of

0.0100kcal/(Angstrom Mol) was reached. The total energies and changes in the ethylene glycol torsion were then extracted. This calculation was repeated using *ab-initio* quantum calculations for 3 levels of Basis Sets available in Hyperchem; the minimal basis set STO-3G which is composed of 3 Gaussian orbitals; the 6-31G* basis set which has a polarization function for non – hydrogen atoms and a split valence with the atomic core represented as a single Gaussian made of 6 primitive Gaussian orbitals and the valence electrons represented as two functions, a Gaussian composed of 3 primitives and a Gaussian composed of 1 primitive; and the 6-31G** basis set which is the 6-31G* basis set with polarization on all atoms. The results of the calculations are shown in Table 2-1.

Table 2-1: *ab-initio* results for ethylene glycol geometry optimizations. The angle value in parentheses represents the final torsion angle value after minimization.

Basis Set	Torsion Angle (degrees)	Total Energy (kcal/mol)	Energy Difference With Trans State
STO-3G	180	-141791.14	-
	65(74.3)	-141790.39	+0.75
6-31G*	180	-143663.15	-
	65(72.5)	-143661.52	+1.63
6-31G**	180	-143663.15	-
	65(72.5)	-143661.52	+1.63

2.2-2 Semi-Empirical Calculations

In a further attempt to reproduce the sign and magnitude of the of the torsional state energy differences, semi empirical calculations were also performed on ethylene glycol. These unconstrained geometry optimizations were also performed using the Polak-Ribiere minimization algorithm, and to a RMS energy gradient of 0.0100kcal/(Å mole). The same initial trans and gauche molecular structures were used. Various semi empirical methods were compared for this study. Many of these methods are characterized as Neglect of Differential Overlap (NDO) methods. (8) In the calculations of the electron-electron interactions, there are steps in which there are some overlaps of electron density between atomic orbitals. These NDO methods describe to what degree these overlaps are ignored and replaced with various empirical parameter sets. The methods used in this work were: Complete Neglect of Differential Overlap (CNDO); Intermediate Neglect of Differential Overlap (INDO); Modified Neglect of Differential Overlap Version 3 (MINDO-3); and Zerner's version of INDO (ZINDO). The other sets of semi empirical methods used (MNDO, MNDO/d, AM1 and PM3) are classified as Neglect of Diatomic Differential Overlap methods which use the INDO classification with additional electron repulsion integrals. The results of the semi empirical calculations are listed in Table 2-2.

Table 2-2: Semi empirical geometry optimization calculations on ethylene glycol. The angle value in parentheses represents the final torsion angle value after minimization.

Computational Method	Torsion Angle (degrees)	Total Energy (kcal/mol)	Energy Difference With Trans State	Bond Angles (degrees)
CNDO	180	-34973.52	-	109.8
	65(58.0)	-34973.49	+0.03	109.7
INDO	180	-33587.24	-	108.0
	65(61.7)	-33587.25	-0.01	109.2
MINDO3	180	-22283.59	-	108.0
	65(82)	-22283.77	-0.18	111.0
MNDOd	180	-22745.57	-	108.5
	65(70.8)	-22745.66	-0.09	110.4
MNDO	180	-22745.57	-	108.5
	65(70.9)	-22745.67	-0.1	110.4
AM1	180	-22609.38	-	106.2
	65(2.44)	-22613.33	-3.95(H-Bonding?)	111.0
PM3	180	-21152.89	-	106.7
	65(70.9)	-21156.23	-3.34	112.9
ZINDO1	180	-32007.02	-	107.5
	65(45.1)	-32008.20	-1.17	108.4

Neither semi-empirical nor *ab initio* methods were capable of reproducing the ethylene glycol torsional states energy difference, perhaps due to the computational limitation of using ethylene glycol for a model compound rather than a larger, more representative molecule that would include more structural effects

The quantum calculations were also used to investigate the location of the gauche torsional angles for ethylene glycol. The local energy minimum associated with the torsional states were found to be $\pm 65^\circ$. Reported literature values of this torsional state has been confirmed at $70^\circ \pm 9^\circ$ by 2-D NMR (2).

The quantum calculations also showed that the bond angles for the ethylene glycol bond vary between 108° and 111° for the trans and gauche states respectively and are not constant. These findings were considered in the later development of the Rotational Isomeric States model for PET.

2.2-3 Molecular Mechanics Calculations

To again test the torsional environment of the ethylene glycol bond, a number of forcefields were also screened. The Amber (9) and MM+ (10) forcefields were considered for this work.

Using the same initial ethylene glycol model used for the previous studies, a geometry optimization was performed. For each torsion angle, the angle was first set and restrained to the appropriate angle using a restraint with a force constant of 1000. Using the Polak-Ribiere algorithm and an RMS gradient termination of $0.01 \text{ kcal}/\text{\AA} \text{ mol}$ the geometry optimization was performed. The results (shown below-scaled to the trans state) indicate a global minimum at a torsion angle of 180° , and two local minima at $\pm 66^\circ$ for the MM+ forcefield and $\pm 65^\circ$ for the Amber forcefield.

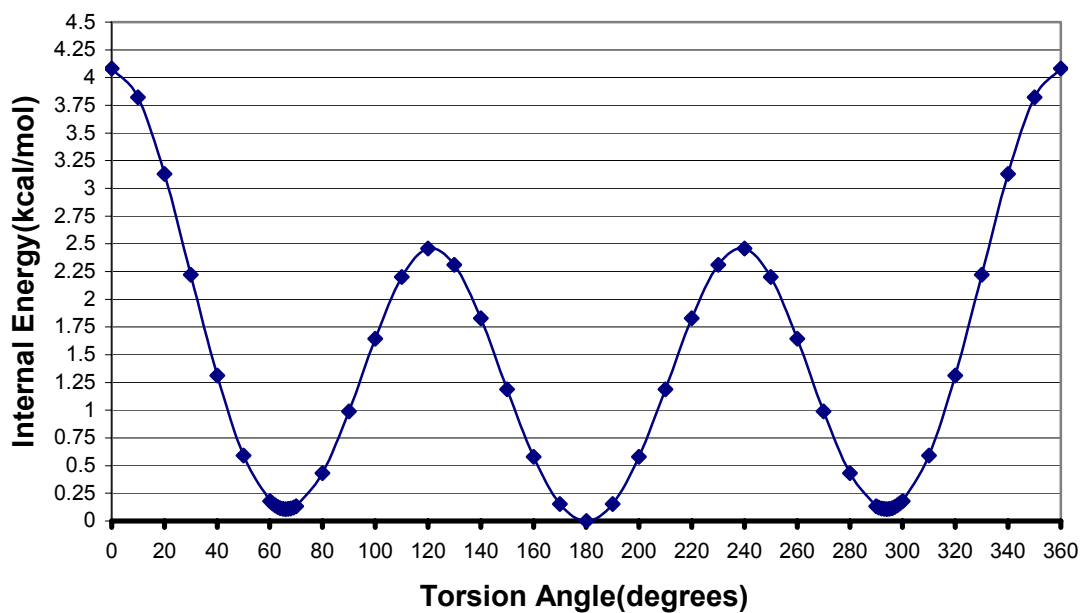


Figure 2-4: Torsional potential for ethylene glycol using the MM+ force field

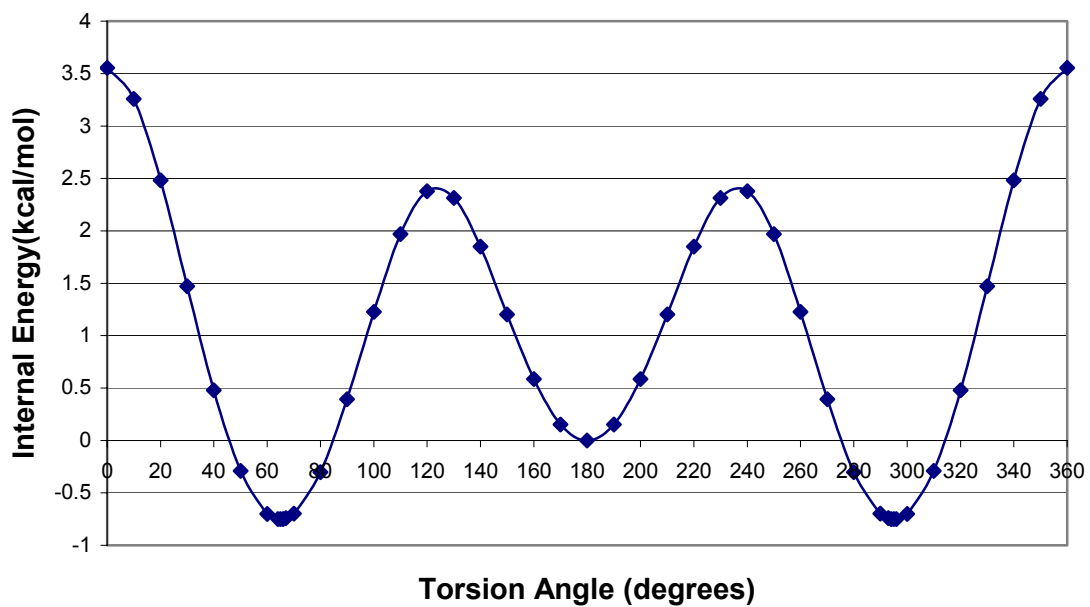


Figure 2-5: Torsional potential for ethylene glycol using the Amber force field

The MM + results indicate that the trans state is approximately 0.108 kcal/mol lower in energy than the gauche states at 66° while the Amber results show global minima at the gauche states of 65° which are 0.751 kcal/mol lower in energy than the trans state. Since the Amber results show both the correct trend and show magnitudes closer to the expected scales of the conformational preferences it is believed that the torsion potential for the OCCO bond in the Amber forcefield is a better representation for the ethylene glycol bond in PET.

2.2-4 Molecular Dynamics Calculations

To complete the examination of the ethylene glycol torsion potential, molecular dynamics simulations were performed on an isolated molecule at 300K. The shape of the internal energy plot versus the torsion angle should show similar trends as the correct molecular mechanics simulation except the MD simulations will include some local entropy effects. The simulations were performed by first setting and then restraining the torsion angle using a harmonic restraining function with a force constant of 1000 (kcal/Å² mole). In order to maintain a constant temperature during the simulation the default temperature controller in HYPERCHEM was used. This controller employs a simulated heat bath which is coupled with the system. Controlling this coupling is a bath relaxation parameter which was set at the program default of 0.01 picoseconds (ps). The simulations were carried out for 300 picoseconds.

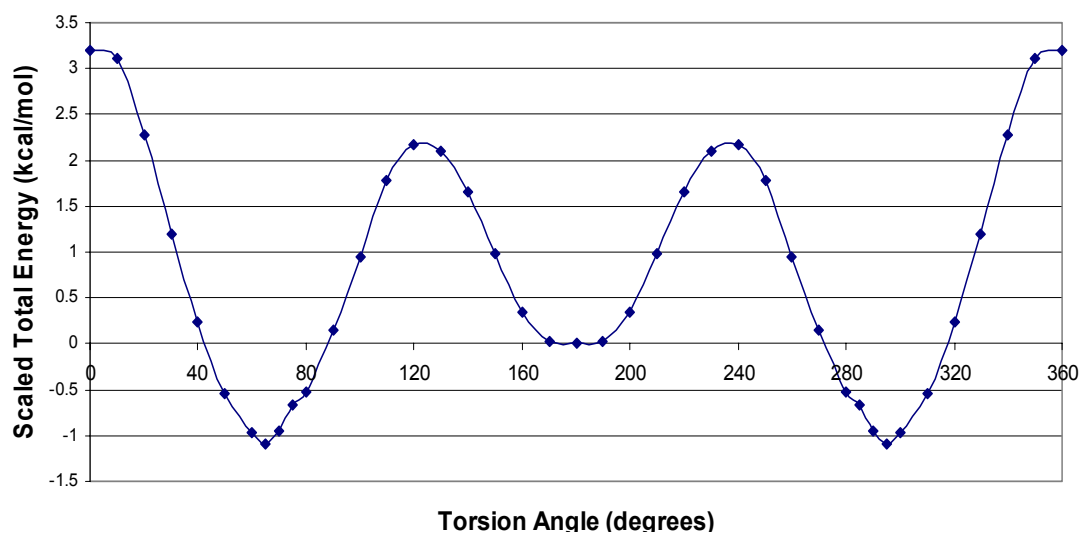


Figure 2-6: Molecular dynamics (300K) and performed on an isolated constrained EG molecule

The internal energy versus torsion angle results (relative to the trans state for the ethylene glycol bond) indicate global minima in potential energy at $\pm 65^\circ$, and a local minima at 180° . As expected, the energies of the gauche conformation are lower than the energies of the trans states by approximately 1kcal/mol.

The results of these studies along with the literature analysis do indicate that there is reason to suspect that the ethylene glycol bond found in PET has a trans torsional fraction that is very different from the simulated Lyon models and that this inaccuracy may be the cause of the lack of difference between the fractional free volume curves calculated by Lyons. To correct this flaw a new Rotational Isomeric States model for both PET and PEN must be developed.

2.3 Rotational Isomeric States Models

The Rotational Isomeric States (RIS) model, originally developed by Flory (11), describes polymer conformations in terms of a Markov model of torsional state probabilities. Typically a 1st order Markov model is used, but flexible polymers, such as poly(ethylene oxide) require a 2nd order treatment (12). The vast majority of conformational changes in polymer chains occur due to changes in the backbone torsion angles, RIS models are useful in characterizing polymer conformations. The RIS model is also useful in generating initial conformations for molecular simulation (13).

RIS models for polymers are based upon the division of each monomeric unit into specific backbone torsions. The first order Markov chain is then represented by a conditional probability matrix where the matrix U_i represents the probability of torsional state i (columns) as a function of torsional state $i-1$ (rows).

$$U_i = \begin{bmatrix} P_{tt} & P_{tg+} & P_{tg-} \\ P_{g+t} & P_{g+g+} & P_{g+g-} \\ P_{g-t} & P_{g-g+} & P_{g-g-} \end{bmatrix} \quad [2.1]$$

where each probability P can be expressed such as

$$P_{tt} = \iint_{\phi_1=180^\circ \pm \delta, \phi_2=180^\circ \pm \delta} e^{-(E_t - E_o)/kT} d\phi \quad [2.2]$$

where E_t is the energy of the selected conformation and E_o is the energy of the reference state, k is the Boltzmann factor, and T is the temperature.

These statistical weight matrices are the heart of the matrix generator method developed by Flory (11) to calculate the unperturbed chains; $\langle r_o^2 \rangle$ the mean square

unperturbed end-to-end distance, and $\langle r_o^2 \rangle$ the mean square unperturbed radius of gyration. In this method, the configuration partition function for a chain of length n is

$$Z = \prod_{i=1}^n U_i \quad [2.3]$$

where

$$U_1 = [1 \quad 0 \quad \dots \quad 0] \quad [2.4]$$

$$U_n = \begin{bmatrix} 1 \\ 0 \\ \dots \\ 1 \end{bmatrix} \quad [2.5]$$

$\langle r_o^2 \rangle$ can be calculated by

$$\langle r_o^2 \rangle = \frac{1}{Z} \prod_{i=1}^n G_i \quad [2.6]$$

where

$$G_i = [u_{i1}g_1 \quad u_{i2}g_1 \quad \dots \quad u_{in}g_1]_1 \quad [2.7]$$

$$G_i = (U_i \otimes I_A) \begin{bmatrix} g_i & 0 & 0 \\ 0 & g_i & 0 \\ 0 & 0 & g_i \end{bmatrix} \text{ for } 1 < i < n \quad [2.8]$$

$$G_n = \begin{bmatrix} u_{n1}g_n \\ u_{n2}g_n \\ \dots \\ u_{nm}g_n \end{bmatrix}_n \quad [2.9]$$

$$(U_i \otimes I_A) = \begin{bmatrix} u_{11}I_A & u_{12}I_A & \dots \\ u_{21}I_A & u_{22}I_A & \dots \\ \dots & \dots & \dots \end{bmatrix}_i \text{ for } 1 < i < n \quad [2.10]$$

$$g_1 = \begin{bmatrix} 1 & 2l_1^T T_1 & l_1^2 \end{bmatrix} \quad [2.11]$$

$$g_i = \begin{bmatrix} 1 & 2l_1^T T_i & l_i^2 \\ 0 & T_i & l \\ 0 & 0 & 1 \end{bmatrix} \text{ for } 1 < i < n \quad [2.12]$$

$$g_n = \begin{bmatrix} l_n^2 \\ l_n \\ 1 \end{bmatrix} \quad [2.13]$$

$$T_1 = \begin{bmatrix} -\cos \theta & \sin \theta & 0 \\ \sin \theta & \cos \theta & 0 \\ 0 & 0 & -1 \end{bmatrix} \quad [2.14]$$

$$T_i = \begin{bmatrix} -\cos \theta & \sin \theta & 0 \\ -\sin \theta \cos \varphi & -\cos \theta \cos \varphi & -\sin \varphi \\ -\sin \theta \sin \varphi & -\cos \theta \sin \varphi & \cos \varphi \end{bmatrix} \text{ for } i > 1 \quad [2.15]$$

$$l_i = \begin{bmatrix} Length_i \\ 0 \\ 0 \end{bmatrix} \quad [2.16]$$

where u are the respective components of the \mathbf{U} statistical weight matrix, I_A is an identity matrix the size of \mathbf{g} , \otimes is the direct product, θ_i is the bond angle, φ_i is the torsion angle, and the $length_i$ is the bond length.

By extension $\langle s_o^2 \rangle$ can be calculated by

$$\langle s_o^2 \rangle = \frac{1}{(1+n)^2 Z} \prod_{i=1}^n H_i \quad [2.17]$$

$$H_1 = [u_{11}h_1 \quad u_{12}h_1 \quad \dots \quad u_{1n}h_1]_1 \quad [2.18]$$

$$H_1 = (U_i \otimes I_A) \begin{bmatrix} h_i & 0 & 0 \\ 0 & h_i & 0 \\ 0 & 0 & h_i \end{bmatrix} \text{ for } 1 < i < n \quad [2.19]$$

$$H_n = \begin{bmatrix} u_{n1}h_n \\ u_{n2}h_n \\ \dots \\ u_{nm}h_n \end{bmatrix}_n \quad [2.20]$$

$$h_1 = [1 \quad g_1 \quad l_1^2] \quad [2.21]$$

$$h_i = \begin{bmatrix} 1 & g_{i1} & l_i^2 \\ 0 & g_i & g_{ij} \\ 0 & 0 & 1 \end{bmatrix} \text{ for } 1 < i < n \quad [2.22]$$

$$h_n = \begin{bmatrix} l_n^2 \\ g_n \\ 1 \end{bmatrix} \quad [2.23]$$

Also by extension $\langle u_o^2 \rangle$ can be calculated by replacing the l_i matrix in the $\langle r_o^2 \rangle$ calculation with

$$m_i = \begin{bmatrix} \text{Dipole Strength}_i \\ 0 \\ 0 \end{bmatrix} \quad [2.24]$$

2.3-1 Original RIS Model for Polyethylene Terephthalate

The original RIS model of PET developed by Flory (4) is based upon the division of each monomeric unit into six specific backbone torsions as seen in Figure 2-7. The first order Markov chain is represented by the conditional probability matrices seen in Equations (2.25-2.30) where the matrix U_i represents the probability of torsional state i as a function of torsional state $i-1$. The parameters γ , σ_x , σ_η , and $\omega_{\eta x}$ represent various intramolecular interactions in the polyester chain. The statistical weight parameter γ is associated with Bond 2, a virtual bond which spans the terephthaloyl unit, and is defined as $\gamma = \exp(-E_\gamma/RT)$, E_γ being the energy of the cis state relative to the trans state. In order for the aromatic ring to be planar with the ester groups, Bond 2 must occupy either the cis (0°) or trans (180°) state. The statistical weight parameter associated with Bonds 4 and 6 (COCC) is σ_x , the weight of a gauche torsional state ($\pm 70^\circ$) in respect to the normalized trans state, having the form $\sigma_x = \exp(-E_{\sigma_x}/RT)$. Bond 5 (OCCO) has the statistical weight parameter σ_η , the weight of a gauche state versus a normalized trans state, where $\sigma_\eta = \exp(-E_{\sigma_\eta}/RT)$. The final parameter is $\omega_{\eta x}$ which governs the four bond interactions for bonds 4, 5, and 6 and is used to calculate the probability of having adjacent torsional bonds with opposing gauche states.

$$U_1 = \begin{bmatrix} 1 & 0 & 0 \\ 1 & 0 & 0 \\ 1 & 0 & 0 \end{bmatrix}$$

[2.25]

$$U_2 = \begin{bmatrix} 1 & \gamma \\ 0 & 0 \\ 0 & 0 \end{bmatrix}$$

[2.26]

$$U_3 = \begin{bmatrix} 1 & 0 & 0 \\ 1 & 0 & 0 \end{bmatrix}$$

[2.27]

$$U_4 = \begin{bmatrix} 1 & \sigma_x & \sigma_x \\ 1 & 0 & 0 \\ 1 & 0 & 0 \end{bmatrix}$$

[2.28]

$$U_5 = \begin{bmatrix} 1 & \sigma_\eta & \sigma_\eta \\ 1 & \sigma_\eta & \sigma_\eta \omega_{\eta x} \\ 1 & \sigma_\eta \omega_{\eta x} & \sigma_\eta \end{bmatrix}$$

[2.29]

$$U_6 = \begin{bmatrix} 1 & \sigma_x & \sigma_x \\ 1 & \sigma_x & \sigma_x \omega_{\eta x} \\ 1 & \sigma_x \omega_{\eta x} & \sigma_x \end{bmatrix}$$

[2.30]

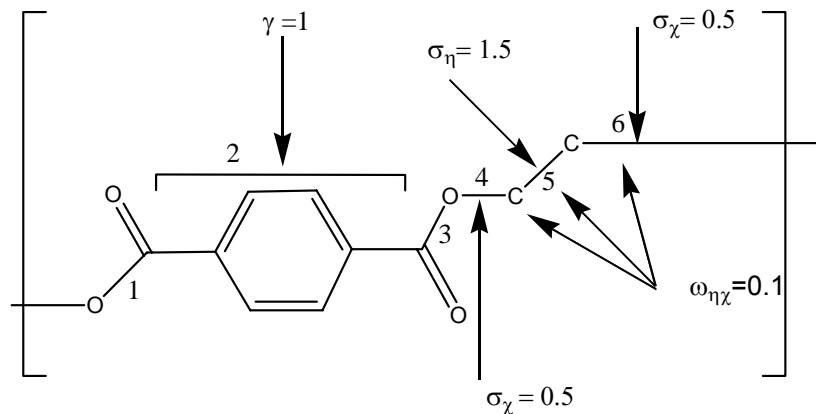


Figure 2-7: PET RIS bond assignments. The Greek letters represent the statistical weight parameters for each bond and Flory's assigned values for them.

2.3-2 Development of New RIS Model for PET

The new RIS model includes re-parameterized values based on fits to both experimental and now computational quantum chemistry results. These results were simply not available when Flory and co-workers developed the initial PET RIS model. The RIS model assumes that all other geometric parameters other than the torsional states are fixed. These include all of the bond length and bond angle values. In this study we used the same values for the bond lengths, bond angles and local energy minima for the torsional states that Flory used. These values compared reasonably well to those obtained from computational quantum chemistry results as discussed in later sections.

The four parameters required to specify the RIS model in Equations (2.25-2.30) must be fit to conformational behavior of the PET polymers. Originally Flory determined these parameters by assuming physically reasonable values for three of the parameters and then he fit the fourth parameter to reproduce the characteristic ratio C_∞ , which is the ratio of the mean squared unperturbed end-to-end distance $\langle r_0^2 \rangle$ to the same value for a freely jointed chain of the same geometry

$$C_\infty = \frac{\langle r_0^2 \rangle}{nl^2} \quad [2.31]$$

where n and l are the number of backbone bonds and the average length of these bonds respectively. Flory assumed that $\omega_{\eta x} = 0.1$ which reflects the low probability of a $g \pm g \mp$ conformation in Bonds 4, 5, and 6. The γ parameter was assumed by Flory to be 1. This assumption was made on the basis of the calculated dipole moments of dimethyl and diethyl terephthalate which approximated the experimental values of 2.30 debye (D) and 2.42 D when an equal cis/trans weighting was assumed. The σ_x statistical weight parameter was set to 0.5 to mirror the steric overlaps of the carbonyl and methylene

groups which was explored by Flory in his study of polymethylene (14). The final parameter σ_{η} was chosen as 1.5 since the interaction which it governs is similar to the interaction in polyethylene oxide which had been studied earlier by Flory (15-16). These assumptions made by Flory were checked using the ability of the matrix generator model to predict the characteristic ratio, which they did within 3% of the assumed experimental value of 4.1 (4).

In contrast to Flory's approach, we attempt to reduce the number of assumptions made using a combination of experimental and computational results. We fit the four RIS parameters to three experimental data points including the characteristic ratio, the gauche population of the ethylene oxide bond (Bond 5 in Figure 2-7), and the dipole moment ratio. The characteristic ratio lies in a fairly broad range of experimental values in the literature, 4.1 ± 0.4 (17-21). The amorphous gauche population of the ethylene glycol bond is 86% as determined from FTIR spectroscopy on PET (22). This value was measured on a quenched sample with no crystallinity and with no annealing. Even with annealing at high temperature and time, the samples still remain primarily gauche (22). The third experimental parameter used was the dipole moment ratio D_{∞} of PET

$$D_{\infty} = \frac{\langle \mu_0^2 \rangle}{N_D m_0^2}, \quad [2.32]$$

which is the dimensionless ratio of the mean squared average of the dipole moment of the unperturbed polymer $\langle \mu_0^2 \rangle$ divided by the product of the number of monomeric dipoles N_D and the magnitude of the monomer dipole m_0 . Here we use the value obtained from dielectric measurements by Boyd and co-workers of 0.30 ± 0.2 (23).

Using the three aforementioned experimental values leaves one additional parameter to be determined before the four RIS parameters may be estimated. We

used computational quantum chemistry results to determine this fourth parameter. In order to investigate the sensitivity of the PET conformation to the RIS parameters we also used some of Flory's original values along with a fit to the experimental quantities discussed above.

Initially, Density Functional Theory (DFT) and Hartree Fock calculations were carried out using QCHEM (24) software on three different model compounds to determine the bond lengths, bond angles and local energy minima associated with the torsional states. Dimethyl terephthalate was used to determine the relative cis-trans populations of bond number 2. Methyl benzoate was used to determine the magnitude and geometry of the monomer dipole moment and the dimer compound (seen in Figure 2-8) was used to determine the torsional states of Bonds 4, 5 and 6. This third model compound was also used to verify the bond lengths and bond angle assumed in the RIS model.

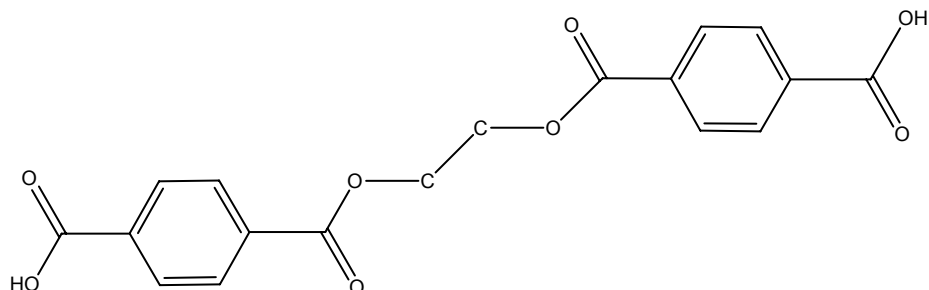


Figure 2-8: Model compound selected for PET. This model compound was used in the QCHEM quantum software package to study the torsional state probabilities for RIS bonds 4, 5, and 6.

Quantum calculations were first carried out concerning the state of Bond 2. Using measured dipole moments of methyl and ethyl benzoate, Flory was able to calculate dipole moments of dimethyl terephthalate (DMT) and diethyl terephthalate with equal cis/trans weighting (4). In order to confirm this assumption and hence determine a value for γ , DFT geometry calculations were performed for DMT. All calculations were carried out using the 6-31G** basis set. The exchange-correlation functional chosen was the Becke's 3 parameter Exchange Functional with Lee-Yang-Parr Correlation (25). Convergence was achieved when the Self-Consistent Field (SCF) energy tolerance of 1.0×10^{-8} was met and the tolerance for the gradient (3.0×10^{-4} hartrees /angstrom) and either the atomic displacement (1.2×10^{-3} angstroms) or total energy (1.0×10^{-6} hartrees) are met, not varying beyond the tolerance value between calculational steps. A Boltzman factor energy expression at 298K was then used with the energy difference between the cis and trans states to calculate the relative populations. It was found that even though the dipole moment of the trans conformation is 0, the energy difference between the two isomers is only 0.028 kcal/mol. Using a Boltzman factor energy expression at 298K, this only results in a trans fraction probability of 0.51. In comparison, basic Hartree Fock *ab-initio* calculations using the same basis set give a trans fraction of 0.53.

This basic quantum calculational procedure was also used to determine the dipole moment and angle associated with the ester bonds in PET. The only addition was that Hartree- Fock calculations were also performed with the Møller-Plesset 2 (MP2) (26) electron correlation correction. The dipole moment was directly calculated and the dipole moment angle was calculated from the net dipole moment vector.

A third set of quantum calculations were performed to verify the geometric assumptions concerning bond angles, lengths, and torsions in PET. In order to examine the flexible torsions found in PET, the model compound shown in Figure 2-2 was

selected for calculations. With the three flexible torsions in PET, Bonds 4, 5 and 6, each having 3 variable states, there are 27 possible different conformations of the model compound. DFT geometry optimizations of each of the conformations was carried out in order to determine the state probabilities for each bond. The same convergence criteria as listed above were used in these calculations and the same Boltzmann factor weighting method was used to calculate torsional populations.

The bond angles and torsions assumed by Flory were also checked using the values extracted from the quantum calculations for this model compound. As shown in Table 2-3, they compare very well to the assumed values.

Table 2-3: Bond angles and bond lengths derived from DFT calculations at B3LYP/6-31G** level of theory. Averages and confidence intervals represent data extracted over 10 sampled conformations.

Bond Angles, °	Flory Assumed Value	Quantum Results @ 95% confidence	Bond Lengths, Å	Flory Assumed Value	Quantum Results @ 95% confidence
O-C(=O)-C	114°	112.02±0.242°	C-C	1.53	1.518±0.002
C'-O-C	113°	116.17±0.261°	O-C	1.44	1.441±0.001
O-C-C	110°	109.40±1.03°	O-C	1.34	1.355±0.003
O-C(=O)-O	125°	122.16±1.25°	C-H	1.09	1.091±0.001
C-C-H	109°	109.14±0.536°	C=O	1.22	1.229±0.023

The geometries and conformational energies for the ethylene oxide torsion (Bond 5 from Figure 2-7) and adjacent bond torsions (Bonds 4 and 6 from Figure 2-7) were also extracted from these calculations. The results from calculations on this compound are compared to those values assumed in Flory's original RIS model in Table 2-4. Note that gauche angle of 70° for the ethylene oxide local minimum assumed by Flory is approximately consistent with the quantum calculations at 66.2° . However, the 88.3° gauche state angle for the adjacent bond obtained from these results differs from the value of 70° assumed by Flory. Using ab initio optimized geometries, Yoon and coworkers also found that the equivalent (COCC) bond in dimethoxyethane to be 80° , also higher than the value assumed by Flory.

Table 2-4: Local energy minima of torsion angles as assigned by Flory for PET and from DFT calculations at B3LYP/6-31G** level of theory. Averages and confidence intervals represent data extracted over 10 sampled conformations.

RIS BOND	Flory Assumed Value	Quantum Results @ 95% confidence
Bond 1 & Bond 3	Trans = 180°	-
Bond 2	Cis = 0°	-
	Trans = 180°	-
Bond 4 & Bond 6	Trans = 180°	178.4±0.002
	Gauche= ±70°	88.3±2.321
Bond 5	Trans = 180°	174.4±4.821
	Gauche= ±70°	66.2±1.751

Table 2-5: Relative energy minima of RIS Bond torsion angles from DFT calculations at B3LYP/6-31G** level of theory.

RIS BOND	State	Relative Energies (kcal/mol)	Relative Boltzmann Populations
Bond 4 & Bond 6	Trans	0.5457	0.3978
	Gauche	0.3003	0.6022
Bond 5	Trans	1.3020	0.1109
	Gauche	0.0696	0.8890

The relative energies (in relation to the all trans configuration) of the RIS states for Bonds 4, 5 and 6 were also extracted from the aforementioned quantum calculations on the compound seen in Figure 2-8. These results for Bonds 4, 5 and 6 are summarized Table 2-5. Because only the local conformational minima were examined, no entropic correction for the curvature of the energy with torsional angle was included. However, the entropic effect of the neighboring bonds was included by averaging the results for each state of each bond (i.e. Bonds 2,4,5 and 6) over the local energy minima of the other three bonds. Table 2-5 shows the relative populations derived from the Boltzmann factors for these states at 300K. The expected high fraction of the gauche conformation in bond 5 is reproduced by the DFT calculations (~89% gauche). This value is close to the experimental value of 86% gauche obtained by Keonig and co-workers using FTIR Spectroscopy (22).

The DFT calculations also suggest a significant gauche effect in the bonds adjacent to the ethylene oxide bond (Bonds 4 and 6 from Figure2-7). Evidence that the

gauche effect in Bonds 4 and 6 is not that pronounced was found in the fitting of the RIS parameters discussed below. Such a large gauche population of Bonds 4 and 6 causes the chain to contract and makes it impossible to match the dipole moment ratio and characteristic ratio. Boyd and co-workers also found this in their reformulation of the potential energy function for PET (23). They contended that either a high trans fraction must be associated with Bonds 4 and 6 or with Bond 2. Boyd claimed that it was unreasonable to assume the trans fraction in Bond 2 was significantly higher than 50% and this is consistent with our quantum calculations on dimethyl terephthalate which predict this bond is 53% trans at 300K. This unexpected high gauche fraction may be a result of improper level of electron correlation and performing Hartree-Fock calculations with MP2 correlation. However it would be extremely difficult to perform this calculation with this size model compound.

While the experimental value of the dipole moment was used in the fitting of the RIS parameter, the value of the monomer dipole (m_0 from equation [2.32]) is required for this fit. Flory and Boyd both assumed a value for this dipole of 1.89 D and that it was rotated 122.7° from the projection of the C-C bond between the benzene ring and the carbonyl carbon as seen in Figure 2-9. Flory found these values through dielectric constant measurements, a data analysis method devised by Smith and Guggenheim on dimethyl terephthalate, and a geometric analysis (27). Quantum calculations on methyl benzoate were not able to reproduce these parameters as indicated by the results in Table 2-6. The angle of this dipole moment appears physically unrealistic given that all of the angles predicted by the calculation are less than the 114° angle made by the vector parallel to the C=O bond in Figure 2-9. Given that the adjacent ester oxygen should be more electron withdrawing than the phenyl ring, one would expect the dipole moment of this group to be rotated at an angle greater than 114° . While the angle does appear to increase as the size of the basis set is increased it does not exceed this 114°

angle. Therefore, we will use the same parameters employed by Flory and Boyd in the calculation of the dipole moment ratio.

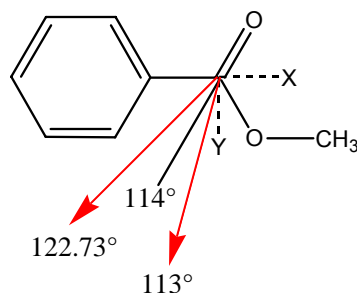


Figure 2-9: Methyl benzoate and its calculated dipole moment of 1.89 debye at 107°.

Table 2-6: Results of *ab-initio* calculations on methyl benzoate

Calculation	Dipole Moment (debye)	Angle
DFT, 6-31G**	1.8508	107.2 °
DFT, 6-31+G**	2.0148	109.0 °
HF, 6-31G**	2.0477	107.3 °
HF, 6-31G**,MP2	2.0721	113.1 °
HF, 6-31+G**,MP2	2.2068	113.3 °

In order to fit the RIS parameters to the selected Characteristic Ratio, Dipole Ratio and torsional state probability for the ethylene glycol linkage, the aforementioned

matrix generator method developed by Flory was used. This method allows for the calculated of chain statistics such as end to end distance, radius of gyration, and mean dipole moment using bond lengths, angles, torsions, individual bond dipoles, number of bonds, and the statistical weight matrices for the determination of backbone torsions angles. The method was integrated into a MATLAB routine that performs a nonlinear constrained minimization to solve for the statistical weight parameters. The routine `fmincon` (28) was used to minimize the sum of the squared residuals of the target parameters. The routine employs a Sequential Quadratic Programming Method (29) for solutions. The default option set was used in all solutions. The initial guess used for these minimizations were varied between the lower bound of 0 placed on all parameters, the original parameter values chosen by Flory and the upper bound of 10 (chosen to be outside of a reasonable set of parameters) on all parameters.

In the original attempts to solve for the parameters it was noted that the response of the characteristic ratio to changing parameters was parallel to that of the OCCO torsion state probability, i.e. in lowering the trans fraction of the ethylene glycol linkage, the characteristic ratio was also lowered beyond the experimental range. Boyd showed that C_∞ was a strong function of σ_η . Due to this response and since Boyd's work and independent studies in this work all suggested that C_∞ was also a function of γ , it was decided that multiple fits of the statistical weight parameters would be performed. In the first fit γ is considered to be fixed at 1 as specified by Flory, making the cis/trans ratio equal to 1. Values will be solved for the other 3 parameters. In the second fit, γ is fixed such that the trans fraction of this bond is 0.53. In the final variation $\omega_{\eta x}$ will be set constant at 0.1, Flory's value, and σ_x , σ_η , and γ will be solved. The overall targets for this analysis are $C_\infty = 4.1 \pm 0.4$, $D_\infty = 0.3 \pm 0.2$, and $\text{Probability}_{\text{Bond 5 = Trans}} = 0.13$. The data shown below represents the best fits of these targets. The values in parentheses

represent the changes seen with a Bond 4/6 gauche state of 70° as assumed by Flory versus the 90° used here.

Table 2-7: Using a MATLAB nonconstrained minimization routine, statistical weight parameters were selected that most closely matched the overall targets. The resulting bond probabilities were not fixed or targets in the routine but were defined by the parameter selection.

1) $\gamma = 1$ (fixed) \rightarrow Probability _{Bond 2= Trans} = 0.50		
Best Fit of Targets	Resulting Parameters	Resulting Bond Probabilities
$C_\infty = 3.7$	$\sigma_\eta = 3.7657$ (2.6543)	Probability _{Bond 4 = Trans} = 0.73 (0.84)
$D_\infty = 0.30$	$\sigma_x = 0.3207$ (0.1524)	
Probability _{Bond 5 = Trans} = 0.17 (0.19)	$\omega_{\eta x} = 0.0027$ (0.1105)	

2) $\gamma = 1.127$ (fixed) \rightarrow Probability _{Bond 2= Trans} = 0.53		
Best Fit of Targets	Resulting Parameters	Resulting Bond Probabilities
$C_\infty = 3.7$	$\sigma_\eta = 4.8546$ (3.3192)	Probability _{Bond 4 = Trans} = 0.72 (0.83)
$D_\infty = 0.30$	$\sigma_x = 0.3503$ (0.1749)	
Probability _{Bond 5 = Trans} = 0.14 (0.165)	$\omega_{\eta x} = 0.0068$ (0.0209)	

3) $\omega_{\eta x} = 0.1$ (fixed)		
Best Fit of Targets	Resulting Parameters	Resulting Bond Probabilities
$C_\infty = 4.1$	$\sigma_\eta = 5.1655$ (5.9534)	Probability _{Bond 4 = Trans} = 0.69 (0.57)
$D_\infty = 0.30$	$\sigma_x = 0.3829$ (0.6267)	Probability _{Bond 2= Trans} = 0.62 (0.76)
Probability _{Bond 5 = Trans} = 0.13	$\gamma = 1.6072$ (3.2076)	

All the above results can be compared with Flory's results, shown in Table 2-8.

Table 2-8: Using Flory's original geometric parameters, the above values were calculated using the aforementioned matrix generation method.

Property	Calculated Value
C_{∞}	4.20
D_{∞}	0.568
Probability _{Bond 2 = Trans}	0.500
Probability _{Bond 4/6 = Trans}	0.593
Probability _{Bond 5 = Trans}	0.357

Table 2-7 shows that in variation 3, the best fit of the targets is achieved. However, this is achieved by forcing Bond 2 into a 62% trans configuration. Based on previous literature and the quantum calculations used in this work, it was felt that this large deviation from a 1/1 cis/trans configuration could not be justified. Therefore, the second variation was selected as the best solution for the parameter set. Comparing the values to Flory's, it can be seen that the higher characteristic ratio found by Flory, results in a higher trans fraction of the ethylene oxide bond. Also the new RIS parameters does a better job of fitting the dipole moment ratio, primarily by increasing the COCC trans fraction.

Using these targets Figure 2-10 was constructed which shows the response of both the characteristic ratio and the dipole moment ratio as the number of monomeric units increase. Both of these calculated values fall with the error range given in literature for these targets. The partial derivative of each target with respect to each statistical

weight parameter is also shown in Table 2-9. These derivatives show the natural dependence of the characteristic ratio and the ethylene glycol trans fraction to the σ_η parameter and the dipole moment ratio to the σ_x parameter. The derivatives are also reasonably low enough for the assumption that the parameters chosen are an acceptable fit to the target values.

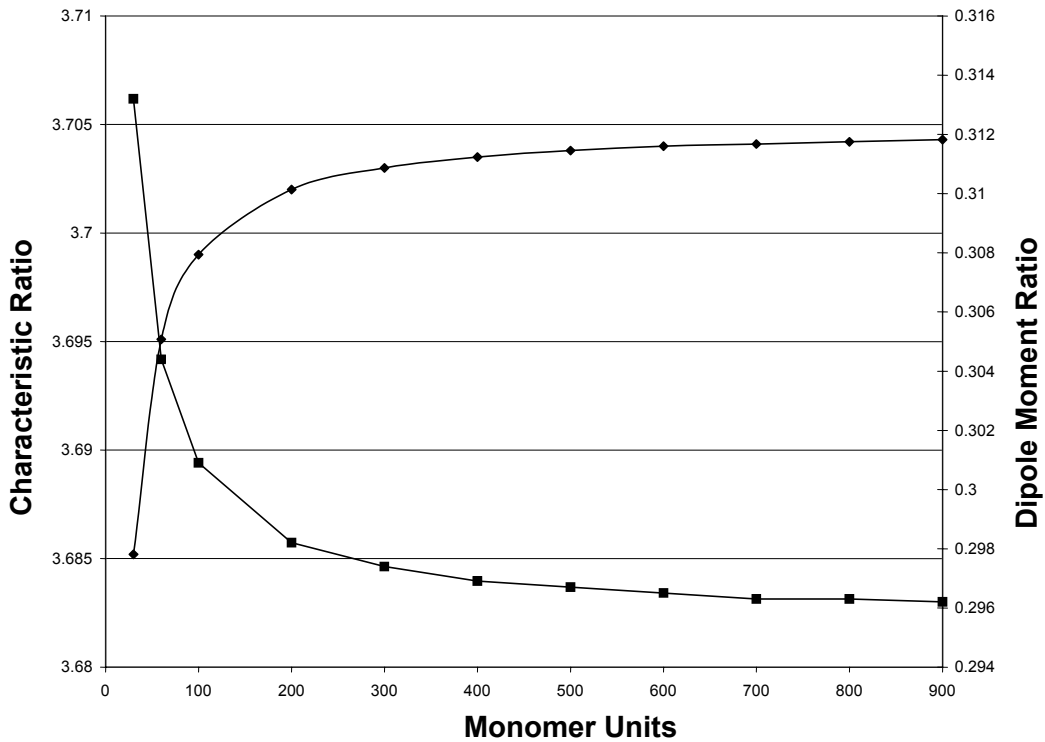


Figure 2-10: Response of characteristic ratio (diamonds) and dipole moment ratio (squares) to an increase in the number of monomeric units

Table 2-9: Derivative analysis shows the dependence of each target on the basic statistical weight parameters.

Normalized Derivatives	$/\partial\sigma_n$	$/\partial\sigma_x$	$/\partial\omega$
$\partial C_\infty /$	-0.1814	0.0672	-0.0020
$\partial D_\infty /$	-0.0719	0.4746	0.0055
$\partial EG_\infty /$	-0.8600	0.2601	-0.0030

Due to the inconclusive nature of the ab-initio calculations, the response of the Dipole Moment ratio to the angle of the dipole was investigated. The strength of the dipole was accepted from Flory's work based on the experimental dipole measurements quoted in that work. As shown in Figure 2-11, the dipole moment ratio is a function of the statistical weight parameter σ_x and the dipole moment angle.

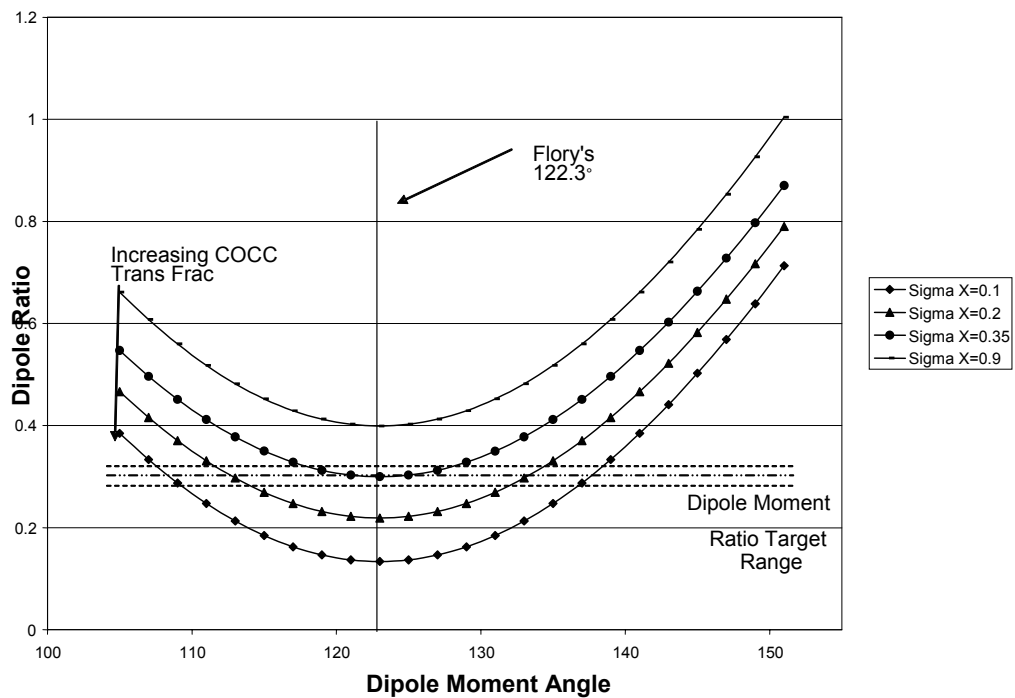


Figure 2-11: Response of dipole moment ratio of PET. Note that in order to achieve the target dipole moment ratio at smaller angles, the COCC trans fraction must increase.

This analysis confirms that selecting a smaller angle would necessitate an increase of σ_x and the OCCO trans fraction which was believed to be unwarranted.

2.3-3 New RIS Model for PET & PEN

The new Rotational Isomeric States model for PET is summarized below.

Table 2-10: Summary of new PET RIS model

RIS Model Parameter	Flory Assumed Value	New Value
γ	1	1.127
σ_x	0.5	0.350
σ_η	1.5	4.855
$\omega_{\eta x}$	0.1	0.00680
Bond 4/6 Gauche Torsion State	70°	90°

Earlier work has shown that the RIS model for PEN can be extrapolated from the PET RIS model via a reassignment of the statistical weight matrices (30). The RIS bond assignments for PEN are shown in Figure 2-12 and the reassignment of the matrices is shown in Table 2-11.

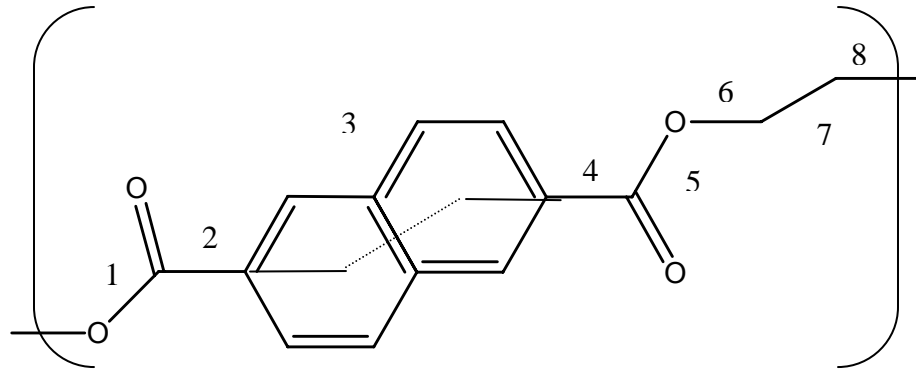


Figure 2-12: PEN RIS bond assignments

Table 2-11: Statistical weight matrices assignment for PET and PEN

RIS BOND NUMBER	Statistical Weight Matrix Assignment	
	PET	PEN
1	U_1	U_1
2	U_2	U_2
3	U_3	Bond always remains trans
4	U_4	U_2
5	U_5	U_3
6	U_6	U_4
7	-	U_5
8	-	U_6

The key difference between the two RIS models is the state of the ethylene glycol bond. FTIR results from collaborators at Case Western Reserve University have

shown us that the OCCO bond in PEN is 27% trans as compared to the 14% seen in PET. This is incorporated in the new PEN RIS model by adding this raw torsional probability directly into the RIS ratio format that is required in the model building stage. All other parameters are the same as the PET RIS model with the mapping of statistical weight matrices as explained in Table 2-11.

2.4 Bulk Models for Polyesters

Using the developed RIS models for PET and PEN, bulk amorphous simulations of both materials were carried out. All simulations were carried out using Accelrys's Cerius2 modeling software. All simulations employed periodic boundary conditions of cubic symmetry P1 to mimic the bulk environment of the polymer. Thirty initial conformations consisting of 1 chain of 120 monomeric units were built using the Amorphous Builder module set at the Cerius2 defaults to the representative densities of PET and PEN of 1.335 and 1.3316 g/cc, respectively. Once the models were built, the Characteristic Ratio C_∞ and torsional state populations of the ethylene glycol bond and the adjacent bonds (RIS bonds 5 and 4/6) were calculated and compared to the expected values to gauge the accuracy of the build process. Using the polymer analysis tools in Cerius2, the end to end distance $\langle r_0 \rangle$ and the radius of gyration $\langle s_0 \rangle$ were extracted from each model. Each value was then used to calculate a Characteristic Ratio using the following equations.

$$C_\infty = \frac{\langle r_0 \rangle^2}{nl^2} \quad [2.33]$$

$$C_\infty = \frac{6\langle s_0 \rangle^2}{nl^2} \quad [2.34]$$

Using Ceruis2's Dihedral Distribution tool, the torsional angles associated with the selected bonds were calculated and a distribution of torsional angles was formed.

The torsional states were then defined as

$$\text{Trans} \quad -180 \leq \phi \leq -125 \quad \& \quad 123 \leq \phi \leq 180$$

$$\text{Gauche} \quad -124 \leq \phi \leq 124$$

The results of the built models are summarized in Table 12.

Table 2-12: Chain building statistics for PET and PEN models. Confidence limits shown represent 95% on 30 models for PET and 17 models for PEN

POLYMER	C_∞ (Based on <s_o>)	C_∞ (Based on <r_o>)	Trans Torsional Fraction BOND 5	Trans Torsional Fraction BOND 4	Trans Torsional Fraction BOND 6
PET	4.25±0.77	4.66±1.45	85.7%±1.3%	70.2%±1.8%	71.1%±1.7%
PEN	8.84±2.51	9.70±4.73	75.2%±1.8%	70.7%±2.0%	73.1%±2.1%

Note that the C_∞ calculated based upon the radius of gyration is closer to the literature values for PET (17-21) and has a much smaller Confidence Interval for the produced models. This is due a lower variation of chain dimension parameters because they are based on all atoms in the chain rather than just the chain ends. This C_∞ and the selected torsional fractions all fall reasonably close to the expected values as defined in the RIS Model section of this chapter and are therefore deemed to be acceptable initial conformations.

2.4-1 Forcefield Development PET

In the selection of a forcefield for this work, the PCFF (Polymer Consistent Forcefield) (17) was chosen as a starting point. The key modifications to the forcefield would be the intrinsic torsion potentials for the OCCO and COCC torsions. To accomplish this task the Conformer Search module in Cerius2 was used. The Grid Scan search method was used with the program defaults.

For the OCCO torsion, a model compound (Figure 2-13) was selected to represent a segment of the PET chain symmetric about this bond.

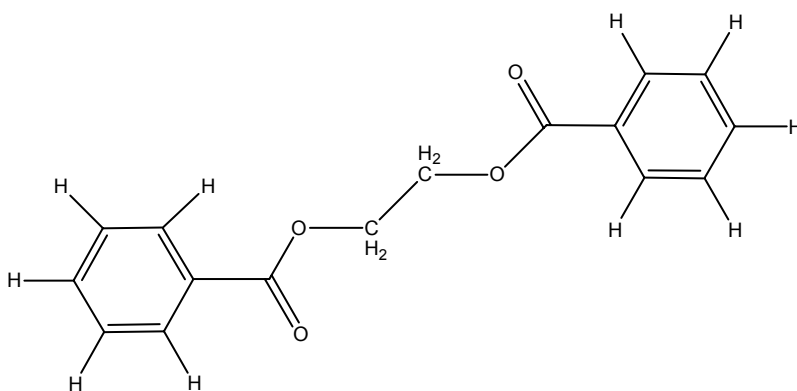


Figure 2-13: Model compound representing a portion of the PET chain symmetric about the ethylene glycol bond

The compound was placed in the extended or all trans position. The OCCO bond was then varied from 0° to 360° in 10° increments. The total energy was calculated for each of these conformations and a conformational map was produced. Examining the decomposed version of the potential, it is seen that it is the 1st fold coefficient or the K1 coefficient which drives the energy difference between the gauche and trans energy

states (Figure 2-14). Therefore starting with the initial parameter set from the PCFF the 1st fold potential coefficient was changed until an energy difference of 0.7 kcal/mol (representing a trans fraction of 14%) between the local minima trans and gauche states was reached.

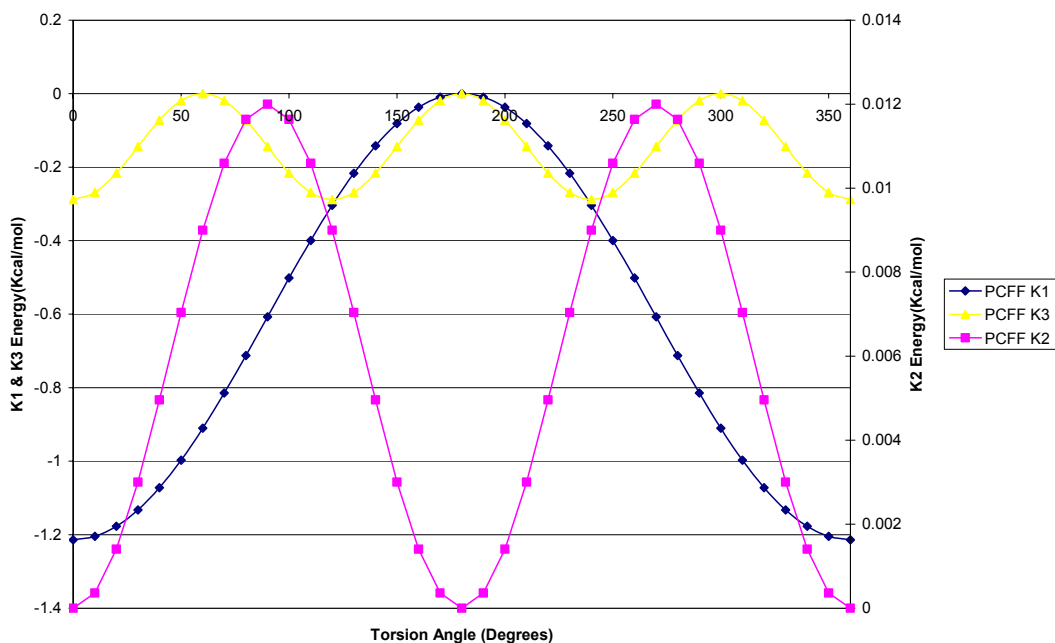


Figure 2-14: Decomposed OCCO intrinsic torsion potential

$$E_{torsion} = 0.5 \sum_{j=1}^3 (k_{\phi,j} (1 - d_j \cos(n_j \phi))) \quad [2.35]$$

Table 2-13: Initial and final forms of the OCCO intrinsic torsional potential

Initial Intrinsic Torsion Potential Parameters			
	n	k	d
j=1	1	-1.214	-1
j=2	2	0.012	1
j=3	3	-0.2882	-1
Final Intrinsic Torsion Potential Parameters			
	n	k	d
j=1	1	-5.0	-1
j=2	2	0.012	1
j=3	3	-0.2882	-1

Using the new torsional potential, energy minimization was performed on 10 of the built PET models. The steepest descent, conjugate gradient, and Cerius2's Smart Minimizer algorithms (31) were used to relax the models until a root mean square force of 0.01 kcal/(mol Å) was reached. The resulting C_{∞} and ethylene glycol torsion fractions are listed in Table 2-14.

Table 2-14: PET build first relax data

POLYMER	C_{∞} (Based on $\langle s_o \rangle$)	C_{∞} (Based on $\langle r_o \rangle$)	Trans Torsional Fraction BOND 5	Trans Torsional Fraction BOND 4	Trans Torsional Fraction BOND 6
PET	5.27±1.55	5.82±3.30	68.6%±2.3%	40.8%±3.9%	39.6%±2.6%

The results indicate that the relaxed OCCO bonds are much higher in trans fraction than the initial conformation. This result points to the intrinsic torsion potential being incorrectly parameterized for the bulk amorphous PET model. However since PCFF with this modified potential was used to verify the energy of the local minima, this could not be the case. In an attempt to discover the cause of the increase in trans fraction, differences between the isolated chain model compound and the bulk structures were examined and it was discovered that it was the process of modeling the bulk itself that lead to the shift in trans fraction.

To understand how the torsion distribution was being affected by the bulk model, a series of PET models were built at densities lower that of amorphous PET. Since the same RIS was used for each of these builds, each build had the same torsion

distribution, the same as the full set of initially built models. However, when the models were relaxed with the same modified PCFF force field, the results were very different. As Figure 2-15 shows, as the density of the model decreases (i.e the closer it approximates the isolated chain state) the less the OCCO torsion deviates from the built, and correct conformation.

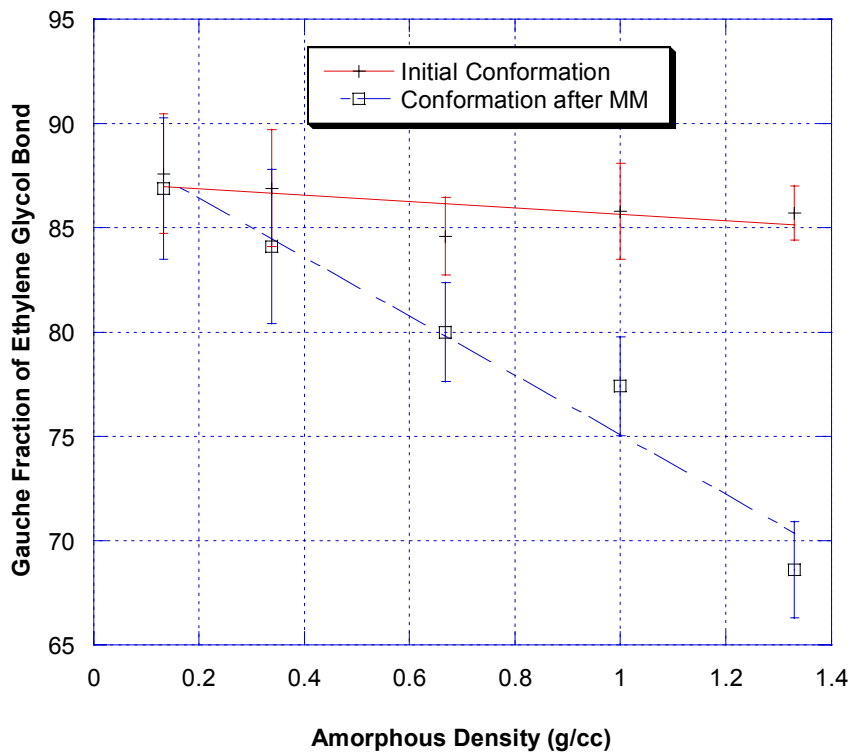


Figure 2-15: Amorphous density versus ethylene glycol gauche torsion fraction for PET. The lines for each data set represent a linear fit of the data.

The explanation for this finding is that due to the dense amorphous structure and the highly gauche conformation of the OCCO bond, the total energy associated with

each individual OCCO bond is much higher, due to the more numerous intermolecular interactions. This effect is similar to the “condensed phase effect” that Yoon noted for poly(oxyethylene) (POE). (32) In POE, Yoon found that simulated melt chains were more elongated than simulated phantom or isolated chains. This elongation was theorized to be due to lower gauche^(+/-) gauche^(-/+) conformations of the C-C-O torsion pair in the melt. According to Yoon, these conformations were disfavored in the melt due to intermolecular O···CH interactions. Due to the similarity of the PET and PEO structures, it is reasonable to theorize that the same effect is being noted in PET relaxations. To overcome this factor the K1 coefficient had to be substantially increased (Table 2-15).

Table 2-15: Final form of the OCCO intrinsic torsion potential [2.35] used for PET relaxation

Final Intrinsic Torsion Potential Parameters			
	n	k	d
j=1	1	-15.0	-1
j=2	2	0.012	1
j=3	3	-0.2882	-1

Due to there not being an ideal symmetric model compound which could be used for the COCC bond and because of the aforementioned role that the bulk plays in developing the torsion distribution, the intrinsic potential for this bond was parameterized by a series of trial and error bulk simulations in which the K1 coefficient was systemically

varied until the correct torsion fraction was achieved. This type of trial and error analysis was also used to parameterize the OCCO and COCC intrinsic torsion potentials for PEN models. The initial and final forms of the PET COCC potential are shown in Table 2-16, and the final forms of the PEN potentials [2.34] are shown in Table 2-17.

Table 2-16: Initial and final COCC intrinsic torsion potentials for PET

Initial Intrinsic Torsion Potential Parameters			
	n	k	d
j=1	1	0	1
j=3	3	-0.3864	1
Final Intrinsic Torsion Potential Parameters			
	n	k	d
j=1	1	-4.0	1
j=3	3	-0.3864	1

Table 2-17: Final OCCO and COCC intrinsic torsion potentials for PEN

Final OCCO Intrinsic Torsion Potential Parameters			
	n	k	d
j=1	1	-49.0	-1
j=2	2	0.012	1
j=3	3	-0.2882	-1
Final COCC Intrinsic Torsion Potential Parameters			
	n	k	d
j=1	1	-12.0	-1
j=3	3	-0.3864	1

Using the modified PCFF forcefields, the initial PET and PEN builds were relaxed in using the aforementioned method. The final relaxed models were checked for the C_{∞} and the appropriate torsion fractions (Table 2-18).

Table 2-18: Relaxed model statistics for PET and PEN models. Confidence limits shown represent 95% on 30 models for PET and 17 models for PEN

POLYMER	C_{∞} (Based on $\langle s_o \rangle$)	C_{∞} (Based on $\langle r_o \rangle$)	Trans Torsional Fraction BOND 5	Trans Torsional Fraction BOND 4	Trans Torsional Fraction BOND 6
PET	4.25±0.77	4.63±1.44	85.4%±1.1%	69.3%±1.7%	70.6%±1.5%
PEN	8.82±2.51	9.64±4.69	73.4%±2.0%	71.7%±1.3%	71.6%±1.7%

As a final check of the validity of the relaxed PET and PEN models, the solubility parameter was calculated for each model. The solubility parameter is a measure the intermolecular interactions within a molecular system. The solubility parameter is defined in Hildebrand and Scatchard (33) as

$$\delta_i = \left(\frac{\Delta U_i^v}{V_i^L} \right)^{1/2} \quad [2.35]$$

Where ΔU_i^v is the energy change upon vaporization of a saturated liquid to the idea gas state or cohesive energy, and V_i^L is the molar volume. The cohesive density is considered a measure of the strength of the intermolecular interactions binding the molecules in one phase. A negative cohesive energy would indicate that the material prefers the isolated or gaseous state more than the condensed state.

When considering molecular modeling one can define the solubility parameter as

$$\delta = \left(\frac{\Delta U_{simulated}}{V_{system} N_A} \right)^{1/2} \quad [2.36]$$

where $\Delta U_{simulated}$ is the energy difference between the material in the isolated and bulk states, V_{system} is the volume of the molecular system in the bulk, and N_A is Avogadro's number. The energy difference $\Delta U_{simulated}$ can be calculated by finding the energy of the model with periodic boundary conditions (which represents the bulk state) and without periodic boundary conditions (which represents the isolated chain state). The simulated solubility parameters are then compared with the experimental values for the material, a polymer in this case, in a poorly hydrogen bonding solvent; 21.9 MPa^{1/2} for PET and PEN (34). The results are summarized in Table 2-19.

Table 2-19: Simulated solubility parameters for 30 PET models and 17 PEN models

POLYMER	δ (MPa ^{1/2})	Percent Error from Experimental value
PET	21.17±2.53	-3.3%
PEN	12.40±4.23	-43.4%

The results indicate a good fit for the PET models, but the values for PEN are very different from the expected value. When closely examining the PEN results (Table

2-20), it is noted that several of the models have an incorrect sign for the energy difference and hence a solubility parameter could not be calculated.

Table 2-20: Detailed PEN model solubility parameter results

Model #	E_{Isolated Chain} (Kcal/mol)	E_{Bulk} (Kcal/mol)	Delta E	δ (MPa^{1/2})	RMS force (kcal/mol Å)
1	30900	31190	-290	-	30.56
2	33140	35120	-1980	-	38.54
3	32140	33830	-1690	-	38.87
4	26360	23940	2420	21.54	20.18
5	34790	37710	-2920	-	40.00
6	33500	36760	-3260	-	43.56
7	33130	35670	-2540	-	40.17
8	31850	34110	-2260	-	42.93
9	31000	30900	100	4.38	30.24
10	29170	29000	170	5.71	33.67
11	28390	27500	890	13.06	27.30
12	33670	37000	-3330	-	43.93
13	29620	29390	230	6.64	28.57
14	29900	29440	460	9.39	25.90
15	28160	25650	2510	21.94	14.96
16	29050	28060	990	13.78	26.82
17	27730	26540	1190	15.11	27.91

It should also be noted that these models also have the higher root mean square force in the isolated chain energy calculations. This would indicate that these models are experiencing stresses larger than the other models. It should be noted that Lyons experienced the same issues with PEN models in his work. The problem is associated with the more rigid PEN chain and the difficulty in building an amorphous structure in a self avoiding chain framework and hence is not unexpected, and is not indicative of an inaccurate model. The results indicate that for elongated polymers the simulated solubility parameter may be more of an indication of a structure that is not completely energetically relaxed rather than a structure that is inaccurate. For completeness all of the subsequent work was calculated with and without the models with negative solubility parameters and no difference was seen in the results. Therefore all PET and PEN models will be used in the Free Volume Analysis portion of this work.

Illustrations of the final PET and PEN molecular models used for the analysis are shown below in Figure 2-16.

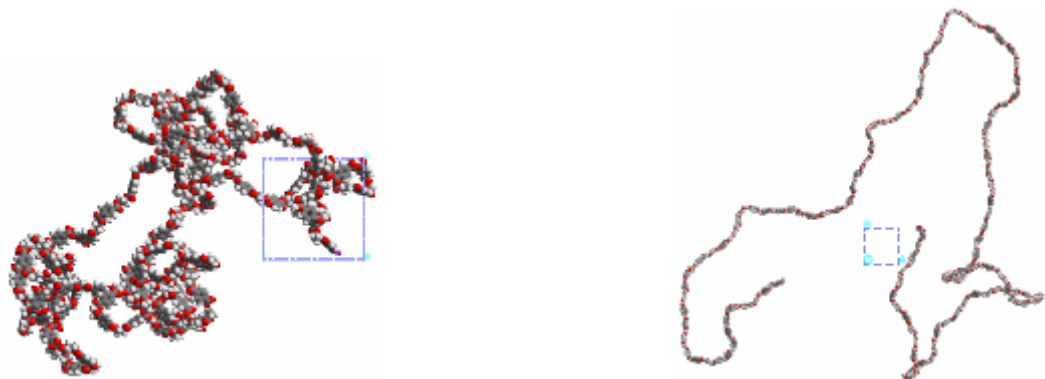


Figure 2-16: PET (left) and PEN (right) molecular models comprised of 120 monomeric units each. The PEN model was zoomed-out to show the elongated conformation of the entire chain.

REFERENCES

1. E. Lyons, "Computer Simulation of Poly(ethyleneTerephthalte) and Derivatives Structure and Their Ramifications for Gas Transport," Masters Thesis, Georgia Institute of Technology, 2000
2. K. Schmidt-Rohr; W. Hu; N. Zumbulyadis, *Science*, V280, p714, 1998
3. C. McDowell; B. Freeman; G. McNeely; M. Haider; A. Hill, *Journal of Polymer Science, Part B: Polymer Physics*, V36, p2981, 1998
4. A. Williams; P. Flory, *Journal of Polymer Science, Part A-2*, V5, pp 417-424, 1967
5. V. Shah; S. Sterr; P. Ludovice, *Macromolecules*, V22, p 4660, 1989
6. S. Arizzi; U. Suter, *Journal of Polymer Science Part B: Polymer Physics*, V30, pp 415 – 426, 1992
7. Hyperchem Inc., Computational Chemistry-Practical Guide, p 59, 2002
8. A. Leach, Molecular Modeling Principles and Applications, Prentice Hall, New York, p87, 2001
9. A. Wilkinson; P.Weiner, Computer Simulation of Biomolecular Systems, Volume 3, p83-96
10. N. Allinger, *Journal of the American Chemical Society*, V99, p8127-8134, 1977
11. P. Flory, *Macromolecules*, V7, pp 381-392, 1974
12. D. Yoon, *Macromolecules*, V26, pp 5213-5218, 1993
13. D. Theodorou and U. Suter, *Polymer Preprints Division of Polymer Chemistry American Chemical Society*, V25(1), p180, 1984
14. P. Flory; A. Williams, *Journal of Polymer Science: A-2*, V5, p399, 1967
15. P. Flory; J. Mark, *Journal of the American Chemical Society*, V87, p1415, 1965
16. P. Flory; J. Mark, *Journal of the American Chemical Society*, V88, p3702, 1966
17. H. Sun, *Journal of Computational Chemistry*, V15, p752, 1994
18. M. Greenfield; D. Theodorou, *Macromolecules*, V26, pp 5461-5472, 1993
19. T. Nakano; Y. Okamoto, *Chemical Review*, V101, pp 4013-4038, 2001

20. M. Allen; D. Tildesley, Computer Simulation of Liquids , pp 126-131, 1987
21. J. Fried; D. Goyal, *Journal of Polymer Science: Part B: Polymer Physics*, V36, pp 519-536, 1998
22. J. Koenig; S. Lin, *Journal of Polymer Science: Part B: Polymer Physics*, V20, pp 2277-2295, 1982
23. R. Boyd; M. Hedenqvist; R. Bharadwaj, *Macromolecules*, V31, pp 1556-1564, 1998
24. QChem Users Guide Version 2.0, 2000
25. R. Parr; W. Yang, Density-Functional Theory of Atoms and Molecules, Oxford University Press, 1989
26. C. Moller; M. Plesset, *Physical Review*, V46, pp618-622, 1934
27. P. Flory; E. Saiz; J. Hummel; M. Plavsic, *Journal of Polymer Chemistry*, V85, pp 3211-3215, 1981
28. MATLAB Software Version 6, Help Manual, The MathWorks, Inc.
29. K. Schittowski, *Annals of Operations Research*, V5, pp. 485-500, 1985
30. J. Youk; W. Jo; D. Yoo, *Polymer Bulletin*, V39, p257, 1997
31. Accelrys Inc., Cerius² Users Guide-Forcefield Based Simulations, San Diego, CA , 1997
32. D. Yoon; G. Smith; R. Jaffe; R. Colby; R. Krishnamoorti; L. Fetters, *Macromolecules*, V29, pp 3462-3469, 1996
33. J. Prausnitz; R. Lichtenthaler; E. Gomes de Azevedo, Molecular Thermodynamics of Fluid-Phase Equilibria, 3rd Edition, Prentice Hall, New Jersey, 1999
34. F. Rodriguez, Principles of Polymer Systems, New York p28, 34 1989

CHAPTER III

POLYESTER FREE VOLUME ANALYSIS

3.1 Free Volume Basics

Free volume is believed to play a key role in the gas transport properties of polymeric materials. However there are several competing theories concerning its role (1,2). Coinciding with the many theories of free volume are the various methods for estimating free volume. Some of these methods are correlations such as the group additivity methods developed by Bondi (3) and Krevelen (4). There are also numerous experimental methods used to “measure” free volume, and of these Positron Annihilation Lifetime Spectrometry (PALS) is one of the most robust.

PALS is based upon the interaction of positrons (the antiparticles of electrons) and electrons in condensed matter. When positrons and electrons combine to annihilate, photons are released which are detected as the lifetime of the positron in the material. (5) This lifetime represents a measure of the electron density in that material (6). When positrons are generated for a PALS experiment, usually through the decay of an unstable isotope such as Na_{22} , a positronium complex (a bound electron – positron pair) is formed. There are several forms of positronium differing by the spin states. It is the ortho-positronium (triplet spin state) which has the longest decay (~100 ns) and has been found to best correlate with free volume (7).

In a PALS experiment, a polymer sample is bombarded with positrons and the ortho-positronium lifetime (τ_3) and intensity (I_3) (relative number of annihilations) are

determined. By making a spherical assumption about the free volume cavities Tao (8) has shown that

$$\tau_{sphere} = \frac{1}{2} \left(1 - \frac{R}{R_0} + \frac{1}{2\pi} \sin \left(\frac{2\pi R}{R_0} \right) \right)^{-1} \quad [3.1]$$

where τ_{sphere} is τ_3 assuming a spherical cavity, R is the radius of the spherical void and $R_0 = R + \Delta R$, $\Delta R = 1.656\text{\AA}$ (an empirical parameter). The free volume cavity size V_f can then be determined by

$$V_f = \frac{4\pi R^3}{3} \quad [3.2]$$

The fractional free volume f can also be found by

$$f = CV_f I_3 \quad [3.3]$$

where C is an arbitrarily chosen scaling factor constant which is 1.5 for spherical cavities (9).

3.2 PET & PEN PALS

Polyethylene terephthalate and polyethylene naphthalate have been studied extensively to characterize their barrier properties and to understand how those properties change with processing and copolymerization (10-12). As part of that work the free volume of these materials have been analyzed using PALS and are summarized below (13).

Table 3-1: PALS experimental results for PET and PEN. Experiments were performed at 25° C

Polymer	o-PS lifetime τ_3 (ns)	Intensity I₃ (%)	R (nm)	Fractional Free Volume f (nm ³ %)
PET	1.59±0.02	23.0±0.2	0.245±0.02	2.14±0.09
PEN	1.56±0.02	22.8±0.2	0.241±0.02	2.02±0.09

These results indicate that there is not a difference in fractional free volume in these materials. These results will be used for comparison to the modeled fractional free volume distribution.

3.3 Modeling Free Volume via Simulations

Significant research has been done in the vein of understanding polymeric free volume size, shape, and distributions via molecular modeling (14-18). One technique that has been used extensively by researchers such as Theodorou and Greenfield (18) is Delaunay tessellation. Delaunay tessellation allows one to deterministically examine the free volume of a polymer model by grouping atoms into tetrahedra and then calculating the simple geometric volume to measure the free volume between the atoms.

The Delaunay tessellation algorithm was developed by Tanemura and Ogawa (19) and described by Arizzi (17) for periodic structures. The algorithm is summarized below.

1. An initial atom i is selected
2. The next atom j is selected to be closer to i than any other atom
3. A third atom k is selected such that the radius of a circle circumscribed around atoms i, j, k is minimized, defining a face
4. The final atom l is selected such that the radius of a sphere circumscribed around atoms $i, j, k,$ and l is minimized, defining a Delaunay tetrahedron
5. All other Delaunay tetrahedron are found with atom i as a vertex
6. Algorithm is repeated for all atoms in system

After all the polymer structure is completely tessellated, the free volume can then be calculated by subtracting out the volume occupied by the atoms. Since each vertex of the tetrahedron is the center of an atom with a representative van der Waal radius, a correction must be performed to the simple geometric volume of the tetrahedron $V_{tetrahedron}$. The unoccupied free volume V_f is defined by Figure 3-1 and Equation [3.4].

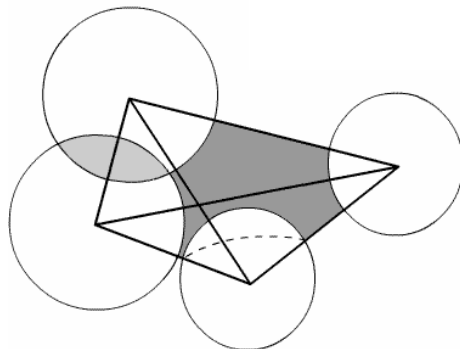


Figure 3-1: Illustration of tetrahedron free volume

$$V_f = V_{tetrahedron} - V_{occupied} + V_{overlap} \quad [3.4]$$

where $V_{occupied}$ is the volume occupied by the atomic radii, and $V_{overlap}$ is the double or triple counted volume due to atomic radii overlaps that must be added back to V_f . A detailed discussion of the correction for triple overlap can be found in reference 20. Quadruple overlap is an important consideration except at the zero size limit of penetrant radii.

In order to develop the full fractional free volume distribution, associated with each tetrahedron, free volume must be the size of a spherical penetrant which can access that free volume. The largest size of that spherical penetrant $R_{penetrant}$ is defined by

$$R_{penetrant} = R - R_{average} \quad [3.5]$$

where R is the circumradius of the largest tetrahedron face, and $R_{average}$ is the average atomic radius of each atoms at the vertices.

One of the limitations of the free volume distribution developed by using the described Delaunay tessellation method is that it only considers the availability of solitary tetrahedron to spherical penetrants. There is no element of the analysis which addresses the connectivity of single tetrahedron into larger structures which may be accessible to larger penetrants. This idea of clustering Delaunay tetrahedrons was first described in work by Arizzi, Mott, and Suter (17) on atactic polypropylene and polycarbonate. The clusters are defined by analyzing neighboring tetrahedron and grouping them together if the faces are large enough to allow the passage of a penetrant of a given size. These clusters can then be analyzed for distributions, shapes and sizes. Repeating the analysis for penetrants of various sizes can also be used for correlations

with various gaseous penetrant data. A description of the clustering algorithm employed in the present work is shown in Figure 3-2.

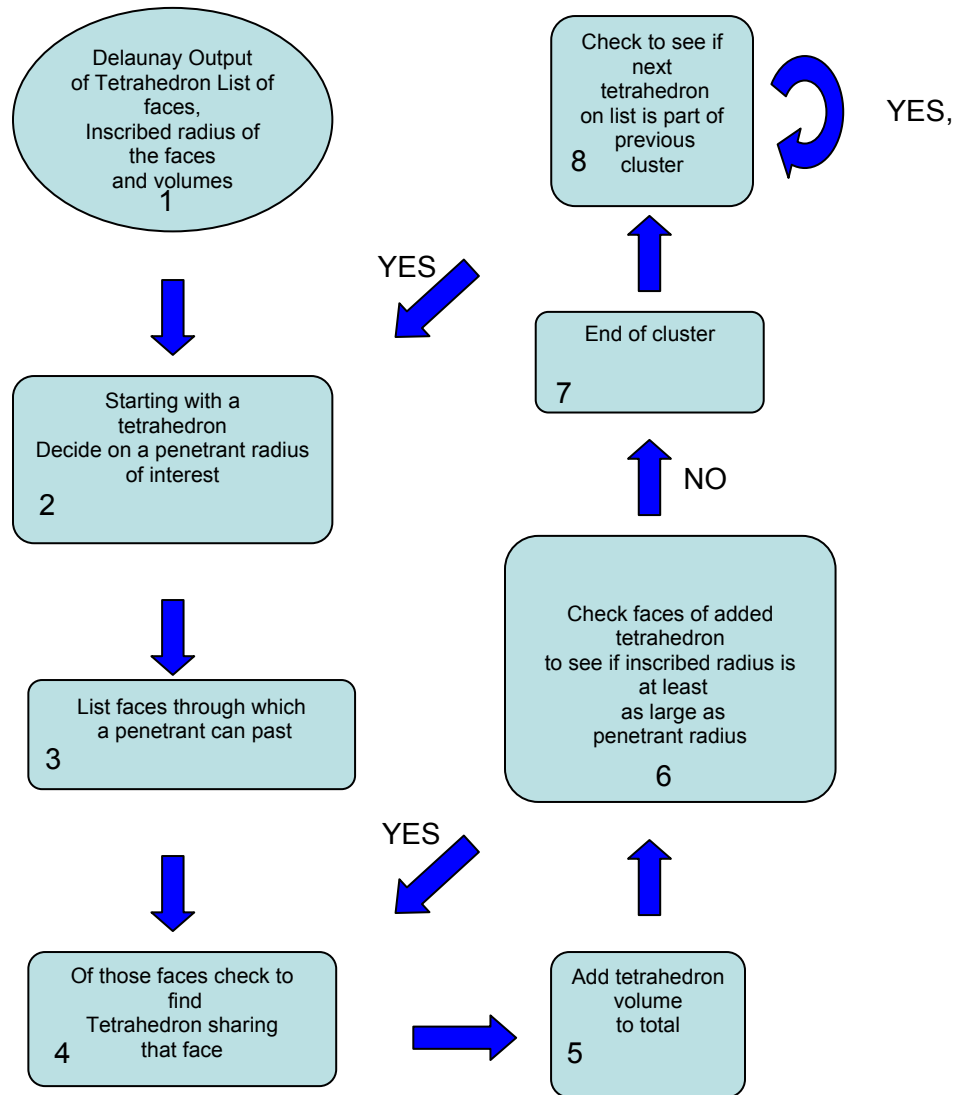


Figure 3-2: Tetrahedron Clustering Algorithm

Using the previously described free volume analysis methods; the developed molecular models of PET and PEN were analyzed.

3.4 Simulated Polyester Free Volume Results

Using the aforementioned free volume analysis methods, 30 amorphous bulk PET models at experimental density and 17 amorphous bulk PEN models at experimental density were analyzed.

The average number of tetrahedron defined for the model structures are shown in Table 3-2 and the distributions of the volumes of those tetrahedra are shown in Figures 3-3 and 3-4.

Table 3-2: Number of defined tetrahedron using Delaunay tessellation at the 95% confidence level

Polymer	Number of Models	Average Number of Delaunay Tetrahedron
PET	30	18824±33
PEN	17	18700±22

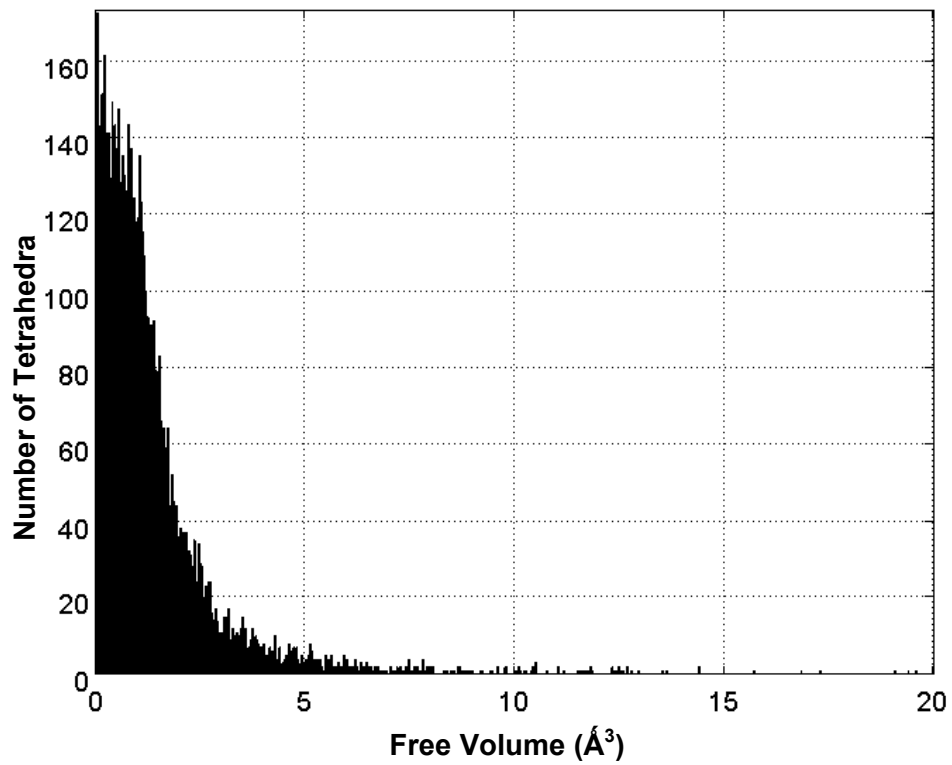


Figure 3-3: Free volume distribution among tetrahedron for representative PET model

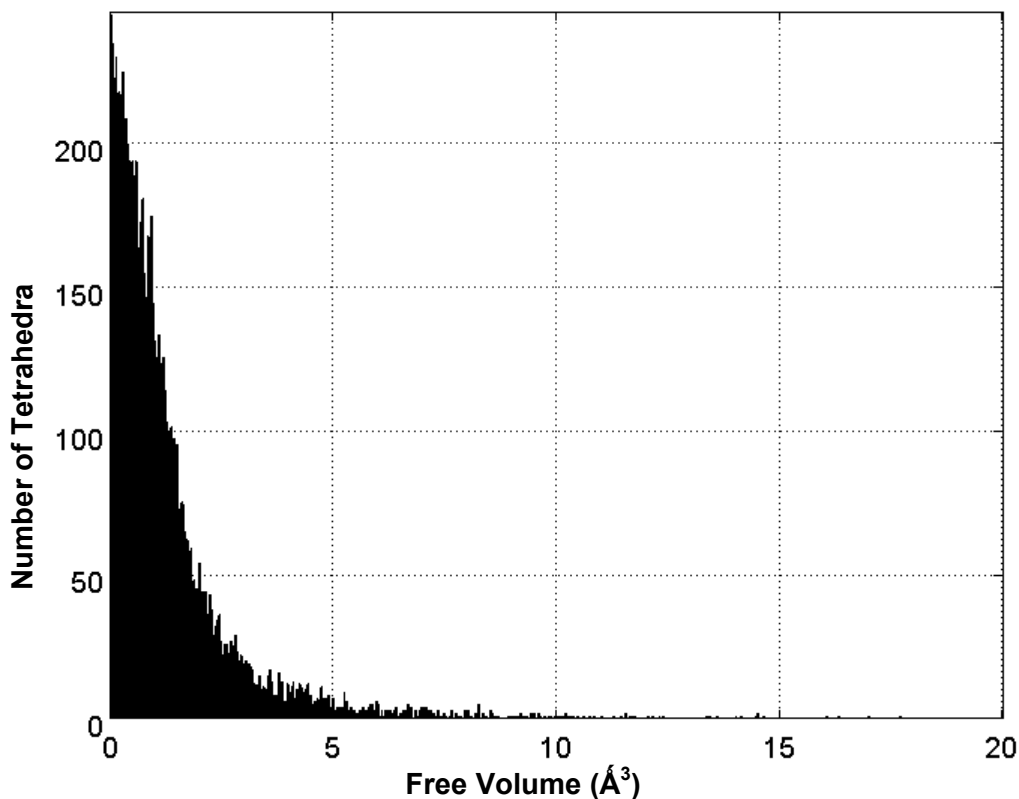


Figure 3-4: Free volume distribution among tetrahedron for representative PEN model

Figures 3-3 and 3-4 indicate that there are more tetrahedra in the PEN structures than the PET structures. However these figures do not account for the volume difference between the PET and PEN models. When normalizing for volume differences, as in Table 3-2 ,PET actually has more tetrahedra per structure. However, most of these tetrahedra are very small, smaller than 1\AA^3 and therefore may play minor roles in gas transport.

Figures 3-5 and 3-6 are histograms for PET and PEN respectively of the total free volume of tetrahedra arranged by the penetrant radii that can access that free volume.

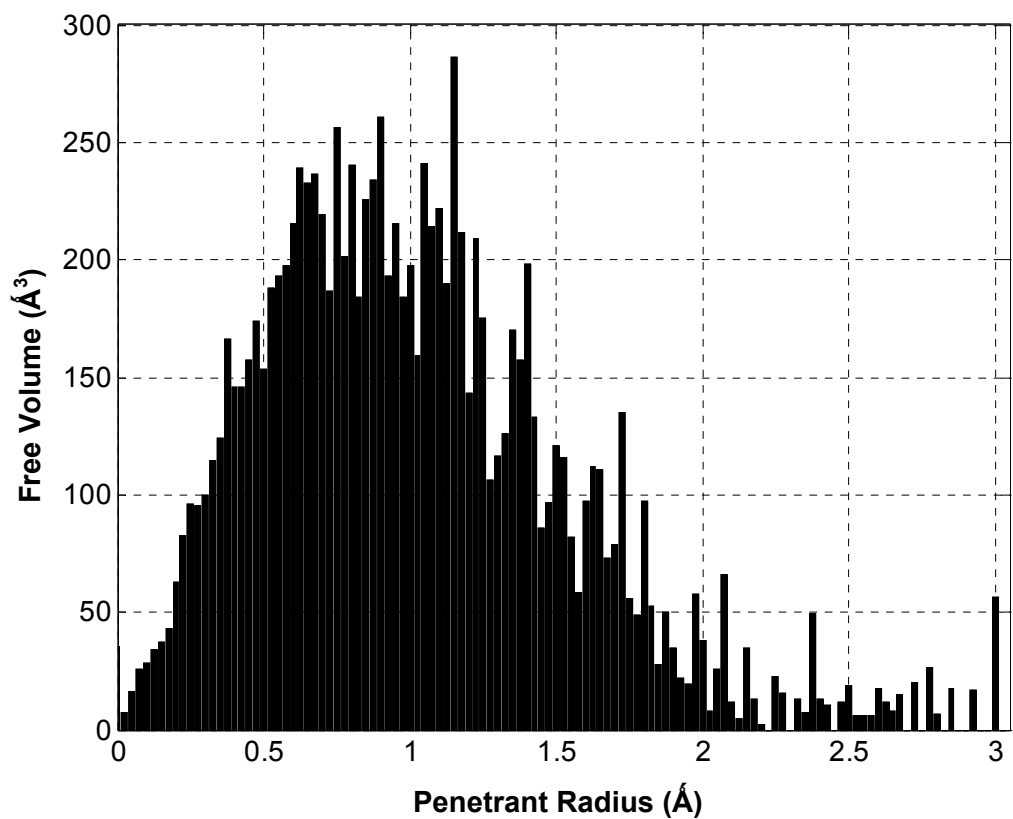


Figure 3-5: Histogram of total free volume within tetrahedra by penetrant radius for a representative PET model

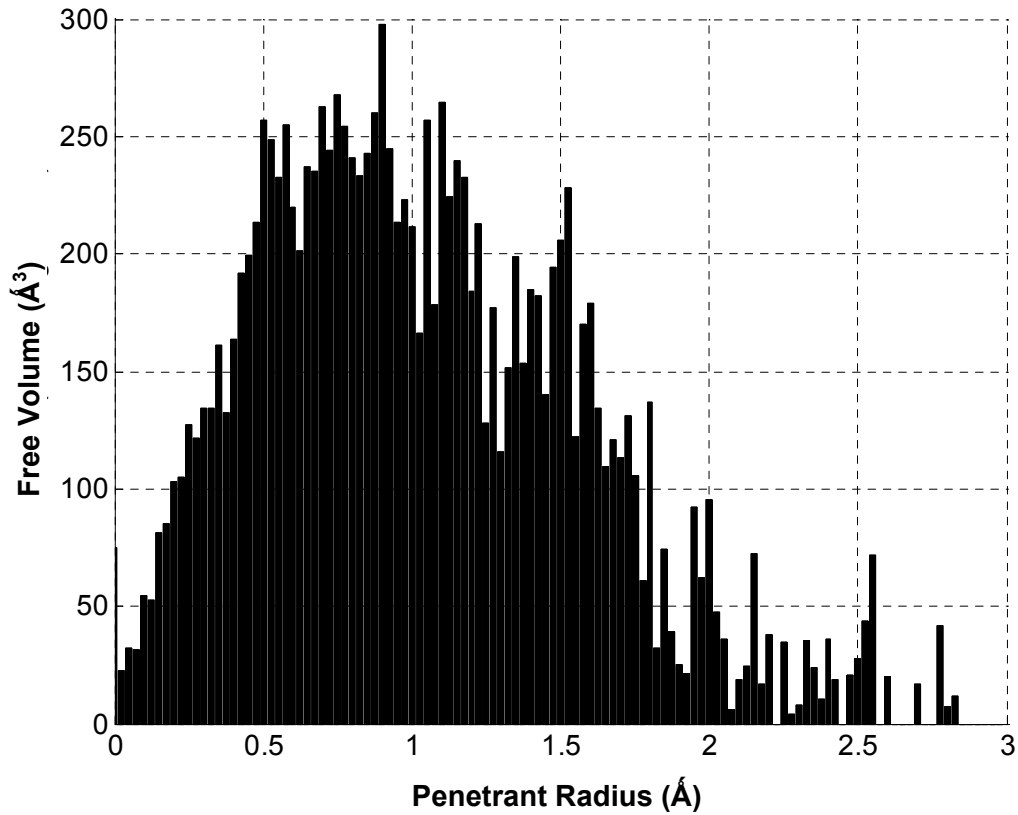


Figure 3-6: Histogram of total free volume within tetrahedra by penetrant radius for a representative PEN model

In order to understand the true differences between these distributions a statistical analysis was performed using various dimensionless moments. The mean \bar{r} , standard deviation σ , skewness γ_3 , and kurtosis γ_4 of all of the model distributions were calculated according to the following formulas

$$\bar{r} = \frac{\sum_i V(r_i)r_i}{\sum_i V(r_i)} \quad [3.6]$$

$$\sigma = \sqrt{\frac{\sum_i V(r_i)(r_i - \bar{r})^2}{\sum_i V(r_i)}} \quad [3.7]$$

$$\gamma_3 = \frac{\sqrt{\frac{\sum_i V(r_i)(r_i - \bar{r})^3}{\sum_i V(r_i)}}}{\sigma^3} \quad [3.8]$$

$$\gamma_4 = \frac{\sqrt{\frac{\sum_i V(r_i)(r_i - \bar{r})^4}{\sum_i V(r_i)}}}{\sigma^4} - 3 \quad [3.6]$$

where $V(r_i)$ is the total free volume for a penetrant of radius r_i . The assignment of the histogram is performed by assigning penetrant radii to bins of 0.03 Å wide therefore r_i is the average bin value and penetrant radius and also the first dimensionless moment. While the standard deviation (or 2nd dimensionless moment about the mean) is a commonly used measure of the breath of a distribution, the skewness and kurtosis (3rd and 4th dimensionless moments about the mean, respectively) are also useful in comparing distributions. The skewness is a measure of how asymmetric the distribution is compared to a normal distribution. A skewness value of 0 represents a normal distribution and a value smaller larger than 0 represents a skew to the right or having an asymmetric tail to the left. The kurtosis is a measure of the peakedness of a distribution. A kurtosis value of 0 represents a normal distribution and values less than 0 represent a flatter than normal distribution. The values for these statistical measures are summarized in Table 3-3.

Table 3-3: Average total free volume distribution statistics with 95% confidence intervals

Polymer	Average Penetrant Radius (Å)	Average Standard Deviation	Average Skewness	Average Kurtosis
PET	1.060 ± 0.013	0.328 ± 0.027	4.071 ± 0.304	31.981 ± 3.998
PEN	1.062 ± 0.013	0.323 ± 0.027	2.805 ± 0.344	25.861 ± 2.919

From Table 3-3, it can be seen that the two polymers distributions are very similar in the average penetrant radius and its standard deviation. The main differences in the distributions are the skewness and kurtosis. While both distributions are skewed to the left and are much more peaked than a normal distribution, PEN's free volume distributions seem to be slightly more normal than the values for PET. These results are much different from those derived by Lyons (21) and represent the difference in the structures produced in this work concerning free volume.

The true test of Hypothesis 1 is to examine the integral fractional free volume distributions of the two polymers. These results are summarized in Figure 3-7.

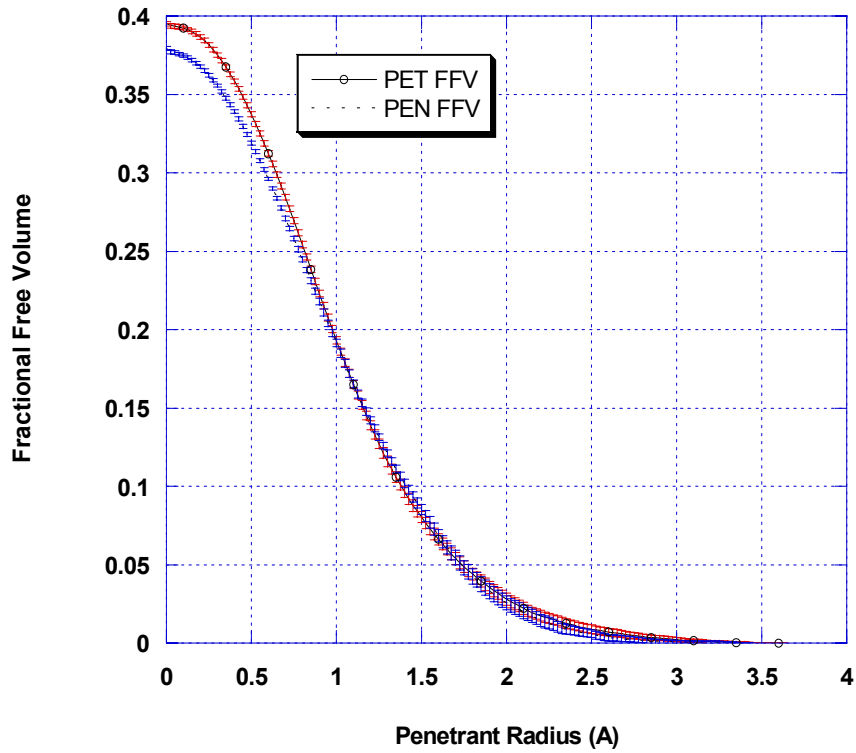


Figure 3-7: Fractional free volume distribution curves for PET and PEN with 95% confidence interval error bars.

The graph indicates that there is a difference in the free volume curves below a penetrant radius size of approximately 0.8 Å. This curve indicates that PET has more total fractional free volume than PEN. This matches the same fractional free volume trend as predicted by Krevelen's Group contribution method, as shown in Table 3-4. Neither set of data is corrected for thermal effects (22).

Table 3-4: Total simulated fractional free volume results for PET and PEN at the 95% confidence level compared to group contribution method

Polymer	Average Total FFV	FFV by Group Contribution
PET	0.395 ± 0.001	0.346
PEN	0.379 ± 0.001	0.339

Even though PET does have the larger total fractional free volume, the curves become indistinguishable for larger penetrant radii, particularly in the size range for gaseous penetrants (23) (Table 3-5).

Table 3-5: Table of gas diffusant radii

Penetrant Gas	Radius (Å)
H ₂	1.464
O ₂	1.675
N ₂	1.740
CH ₄	1.895

These results would seem to indicate that there is not a significant difference in fractional free volume available to PET versus that which is available to PEN in the range of interest of oxygen solubility and hence the free volume distributions can not explain the experimental trends. However this model of free volume does not take into account the connectivity of those free volume cavities.

In order to understand the connectivity of the free volume elements in these materials, clustering analyses were performed for penetrant radii size approximating the ortho-Ps from PALS experiments (1.06 Å) (14) and O₂ (1.675 Å) (23). The results are summarized in Table 3-6 and 3-7 and Figures 3-8 through 3-10.

Table 3-6: Average largest clusters for PET and PEN at o-Ps and O₂ penetrant radii at 95 % confidence limits

Polymer	Average Largest Cluster of o-Ps per model (Number of Tetrahedra)	Average Largest Cluster of O₂ per model (Number of Tetrahedra)
PET	358.733 ± 59.883	101.933 ± 19.608
PEN	337.304 ± 79.609	76.188 ± 22.628

Table 3-7: Average number of clusters for PET and PEN at o-Ps and O₂ penetrant radii at 95 % confidence limits

Polymer	Average Number of o-Ps clusters per model	Average Number of O₂ clusters per model
PET	92.833 ± 4.006	27.700 ± 2.361
PEN	88.408 ± 2.922	35.076 ± 3.191

Table 3-6 shows there is no difference for either o-Ps or O₂ size penetrants in the size of the largest clusters of tetrahedral. However Table 3-7 shows, that while there is a statistical difference in the number of clusters with at least one face large enough for O₂ to penetrate, there is no difference for PALS size penetrants. T-test results shown in Table 3-8 show that the difference between the means for the O₂ sized penetrants is significant at the 99% confidence level and below

Table 3-8: T-test results for the difference between the mean number of PET and PEN clusters for O₂ sized penetrants.

Difference between means	Confidence Level	Degrees of Freedom	T-value	Standard Deviation	Confidence Interval
7.376	0.990	32.000	2.733	2.025	5.546
7.376	0.980	32.000	2.445	2.025	4.959
7.376	0.970	32.000	2.268	2.025	4.600
7.376	0.960	32.000	2.138	2.025	4.336
7.376	0.950	32.000	2.035	2.025	4.125
7.376	0.940	32.000	1.948	2.025	3.949
7.376	0.930	32.000	1.873	2.025	3.797
7.376	0.920	32.000	1.806	2.025	3.662
7.376	0.910	32.000	1.747	2.025	3.541

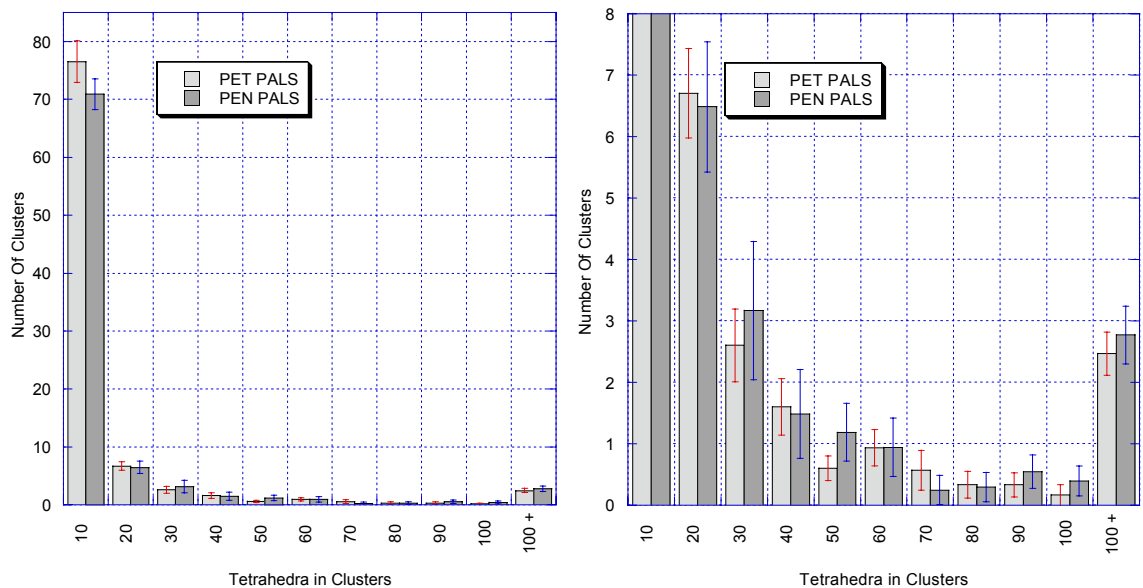


Figure 3-8: Distribution of tetrahedron per cluster of o-Ps radius size for PET and PEN. Error bars represent 95 % confidence interval. Right graph is a close up view of the graph on left

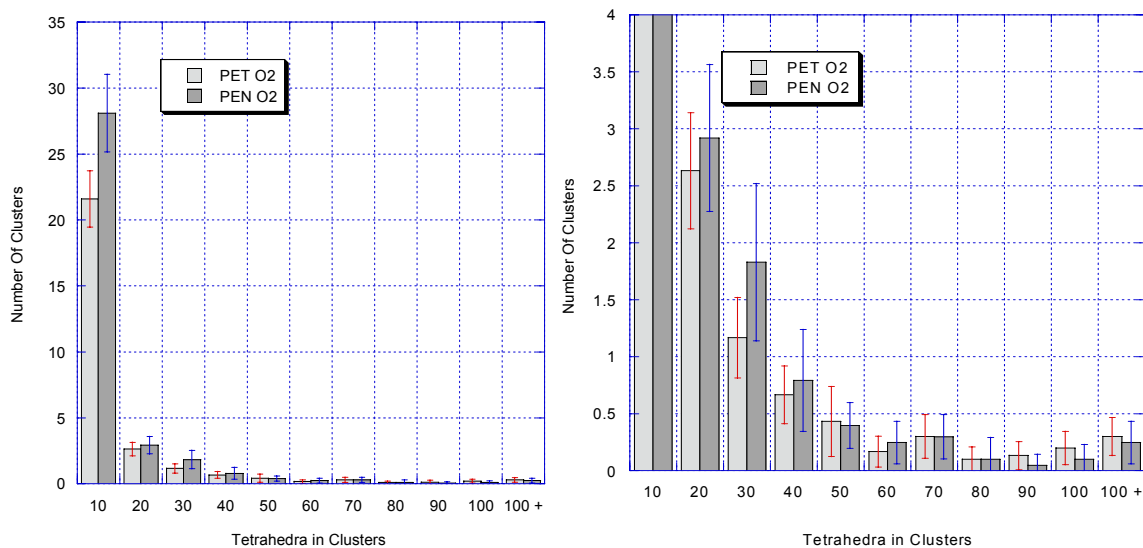


Figure 3-9: Distribution of tetrahedron per cluster of O₂ radius size for PET and PEN. Error bars represent 95 % confidence interval. Right graph is a close up view of the graph on left

Breaking down the distribution of clusters in Figures 3-8, it can be seen that there are no statistical differences in the PALS clusters for clusters composed of any number of tetrahedral, holding with the results seen in Table 3-7. However in Figure 3-9 one can see that the difference in the total number of O₂ sized clusters is a difference for clusters containing a small number of tetrahedrons, less than 10.

When examining the volume of clusters, one may expect that since it is the clusters containing a smaller number of tetrahedra that is different for the two materials, that it would be expressed in a difference of small volumes. Actually, as shown in Figure 3-10, the volume difference is between 20 and 30 Å³.

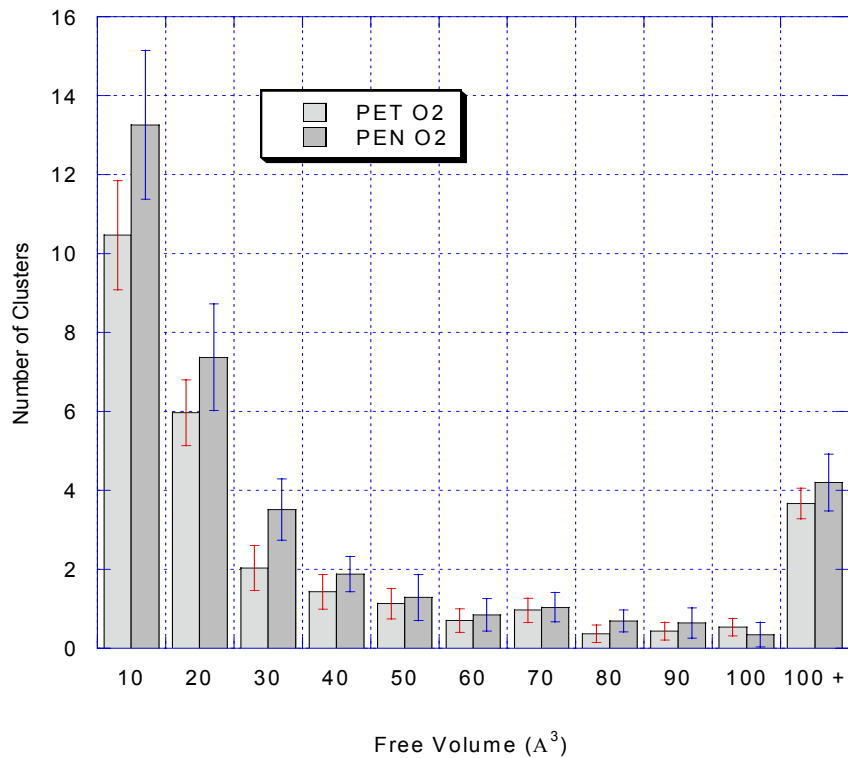


Figure 3-10: Cluster volume distribution for PET and PEN at O₂ size penetrant radius. Confidence limits are at 95 %

In correlating these results with the experimental solubility data it can be noted that for O₂ there are more clusters of free volume in PEN than PET. These clusters of free volume are composed of less than 10 tetrahedra per cluster and have a volume in the range of 20 and 30 Å³. It is these clusters of free volume which are responsible for the higher O₂ solubility in PEN.

REFERENCES

1. T. Aminabhavi; U. Aithal, *Review of Macromolecular Chemical Physics*, V28, pp421-474, 1988
2. M. Cohen; D. Turnbull, *Journal of Chemical Physics*, V31, p1164, 1959
3. A. Bondi, Physical Properties of Molecular Crystals, Liquids, and Glasses, 1968
4. D. Van Krevelen, Properties of Polymers-Correlation with Chemical Structure, 1972
5. R. Pethrick, *Progress In Polymer Science*, V22, pp1-47, 1997
6. A. Hill in Polymer Characterization Techniques and Their Applications to Blends, Oxford University Press
7. W. Brandt; S. Berko; W. Walker, *Worldwide Physics Review*, V120, pp1289-1295, 1960
8. S. Tao, *Journal of Chemical Physics*, V56, pp5499-5510, 1972
9. A. Hill; S. Weinhold; G. Stack; M. Tant, *European Polymer Journal*, V32, p843, 1996
10. A. Polyakova; R. Liu; D. Schiraldi; A. Hiltner; E. Baer, *Journal of Polymer Science Part B: Polymer Physics*, V39, pp 1889-1899, 2001
11. R. Liu; A. Hiltner; E. Baer, *Journal of Polymer Science Part B: Polymer Physics*, V42, pp 493 -504, 2004
12. Y. Hu; R. Liu; L. Zhang; M. Rogunova; D. Schiraldi; S. Nazarenko; A. Hiltner; E. Baer, *Macromolecules*, V35, pp 7326 – 7337, 2002
13. E. McGonigle; J. Liggat; R. Pethrick; S. Jenkins; J. Daly; D. Hayward, *Polymer*, V42, pp 2413 – 2426, 2001
14. M. Greenfield; D. Theodoru, *Macromolecules*, V26, pp 5461 – 5472, 1993
15. S. Misra; W. Mattice, *Macromolecules*, V26, pp 7274 – 7281, 1993
16. D. Rigby; R. Roe, *Macromolecules*, V23, p 5312 – 5472, 1990
17. S. Arizzi; U. W. Suter, *Journal of Polymer Science Part B: Polymer Physics*, V30, pp 415 – 426, 1992
18. D. Theodoru in Diffusion in Polymers, Marcel Dekker Inc, pp 67 – 142, 1996
19. M. Tanemura; T. Ogawa, *Journal of Computational Physics*, V51, p 191, 1983

20. W.Chung , “Molecular Modeling of Structure-Property Relationship for Palladium Catalyzed Poly(Norbornene) and Its Derivatives ,” PhD. Thesis, Georgia Institute of Technology, 2003
21. E. Lyons, “Computer Simulation of Poly(ethyleneTerephthalte) and Derivatives Structure and Their Ramifications for Gas Transport,” MS. Thesis, Georgia Institute of Technology 2000
22. D. Van Krevelen, *Properties of Polymers-Correlation with Chemical Structure*. p 41,1972
23. J. Hirschfelder; C. Curtis; R. Bird, Molecular Theory of Gases and Liquids, John Wiley and Sons, 1964

CHAPTER IV

HEXAFLUROALCOHOL SUBSITUTED POLYNORBORNENE MODELING

The goal of this work is to examine the molecular level structure of bis-trifluoromethyl carbinol or Hexafluroalcohol Subsituted Polynorbornene (HFA-PNB) and to draw correlations between structure and gas transport characteristics. Polynorbornenes are an interesting class of materials for microelectronic applications because of their low dielectric constant, low optical birefringence, and high radiation sensitivity. HFA-PNB is being considered for the next class of photoresist materials required to meet demands for smaller semiconductor feature sizes. In particular HFA-PNB's transparency to the 157 nm wavelength makes it a promising material for the next generation of optical lithography (1-4).

Structurally HFA-PNB is a very intriguing material largely due to the helical/kink structure proposed by Chung (5). The structure of PNB is theorized to be composed of aligned segments that deviate due to kinks as shown in Figure 4-1. As the molecular weight of the polymer grows, the probability of kinks increases and this is theorized to create irregular elongated microvoids.

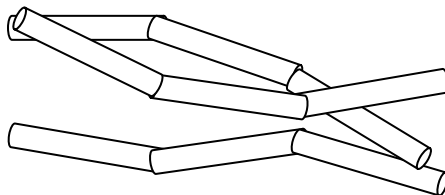


Figure 4-1: PNB helical /kinked structure forming irregular free volume pockets

Hypothesis 2: The microvoids found in PNB are highly nonspherical.

One method of proving this hypothesis will be to see if using a non spherical model developed through molecular modeling with raw PALS data will result in more accurate calculated free volumes.

When determining free volume from PALS lifetime and intensity data, most models assume a spherical microvoid (6) which results in an ortho-positronium (o-Ps) lifetime of

$$\tau_{sphere} = \frac{1}{2} \left(1 - \frac{R}{R_0} + \frac{1}{2\pi} \sin \left(\frac{2\pi R}{R_0} \right) \right)^{-1} \quad [4.1]$$

where R is the radius of the spherical void and $R_0 = R + \Delta R$, $\Delta R = 1.656\text{\AA}$ (an empirical parameter that accounts for the thickness of the electron layer around an atom). This rudimentary assumption fails for materials with irregular structures such as polymers. Some attempts have been made to more accurately describe irregular free volume microvoids through use of correlations that use ellipsoid shapes and cubical shapes (7,8). As found with other high free volume polymers (9), we believe the spherical correlations will result in notably different free volume distributions. We believe that the pockets of free volume in PNB are more accurately represented by a prolate ellipsoid. Jean (7) found that the ratio of lifetimes of o-PS in an ellipsoid to that calculated in a sphere was:

$$\frac{\tau_{ell.}}{\tau_{sphere}} = 1 + 0.4\varepsilon - 4.16\varepsilon^2 + 2.76\varepsilon^3 \quad [4.2]$$

where ε is the eccentricity of the ellipsoid which is $\frac{\sqrt{a^2 - b^2}}{a}$ in which a and b are the major and minor axes of the ellipsoid, respectively. From the geometric analysis of the

PNB structure, we can find average values of a and b which can then be used to calculate o-Ps lifetimes and can be correlated with experimentally measured values. This will confirm the shape of the microvoids.

4.1 HFA-PNB Previous Experimental and Simulated Work

Chung (10) has done considerable work into the structural behavior of substituted polynorbornenes (PNB). Chung's work dealt with palladium catalyzed PNB substituted with alkyl, HFA, and methyl acetate groups. All of the palladium catalyzed PNB structures are believed to adopt the 2,3-erythro di-isotactic form, in which the bridgehead carbons point in alternating directions (Figure 4-2)

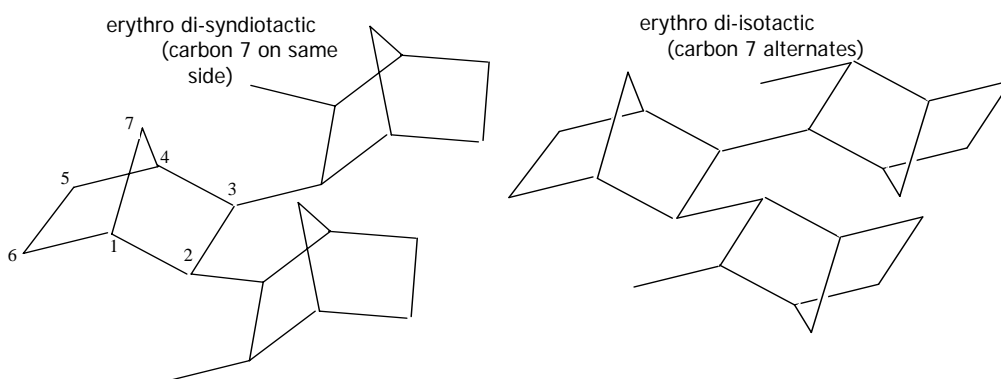


Figure 4-2: Stereochemical configurations of PNB

with the substituent groups located on the 5 or 6 carbons. With this structure, Chung found that this form of PNB most likely had formed a helical structure with occasional kinks in which the rotatable bond alternated between 240° and 120° to form right or left

handed helices. Using this structure expressed in an RIS model, Chung was able to develop simulated structures of PNB which replicate the wide angle X-ray diffraction patterns of this class of polymers.

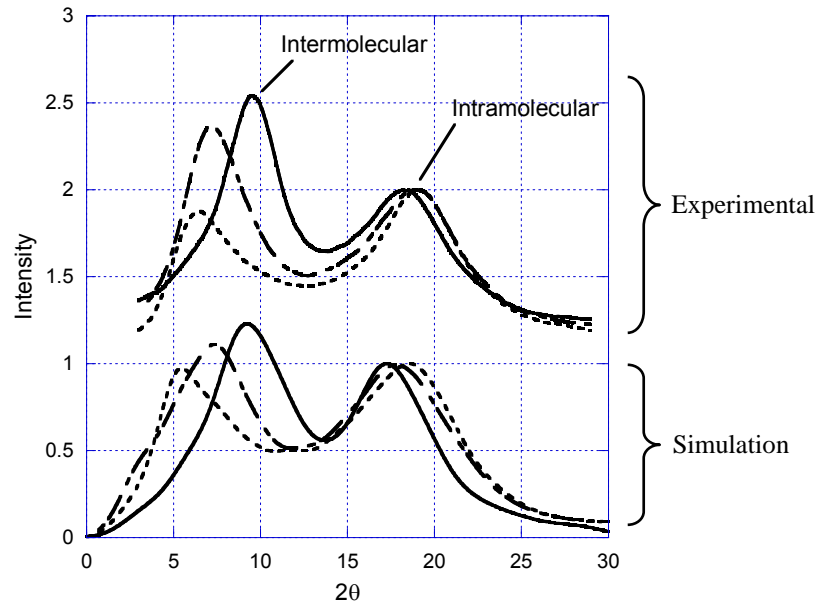


Figure 4-3: Chung's comparison between simulated and experimental WAXD patterns for methyl (solid), butyl (short-long dash), and hexyl (dotted) PNB

Chung also developed models of HFA substituted PNB in which he was able to show the shift in the low angle or intermolecular peak as a function of alignment.

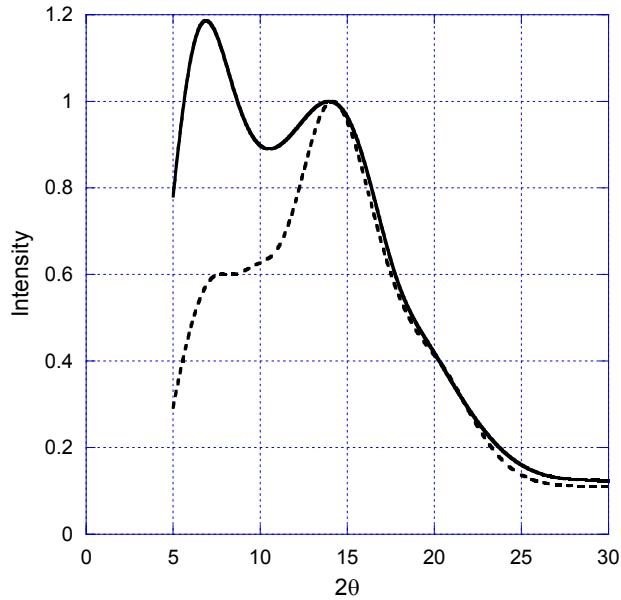


Figure 4-4: Simulated WAXD patterns for HFA-PNB. The solid line represents a periodic model composed of 4 perfect chains and the dotted line represents 2 amorphous chains

To develop these simulated WAXD patterns Chung used 2 models. The first periodic model was composed of 4 chains of 40 monomers of HFA-PNB perfectly aligned (Figure 4-5). The second periodic model was composed of 2 chains of 100 monomers of HFA-PNB and was completely amorphous (Figure 4-6).

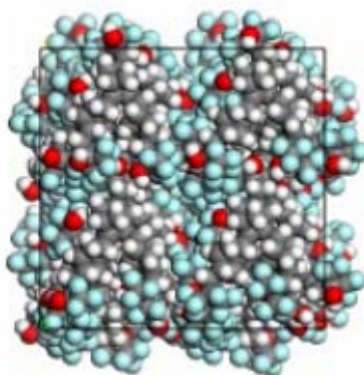


Figure 4-5: 4 Chain perfect HFA-PNB periodic model used by Chung

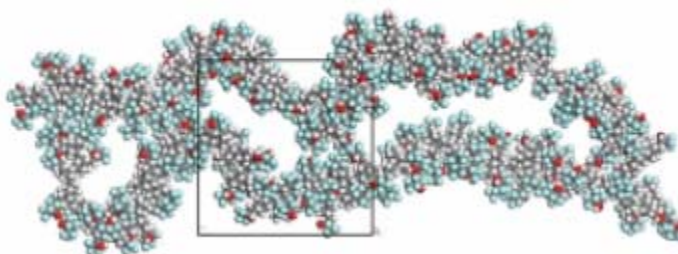


Figure 4-6: 2 Chain amorphous HFA-PNB periodic model used by Chung

The work described in this chapter uses these two models as a basis for the free volume microvoid shape analysis.

4.2 HFA-PNB Simulated Intermediate Models

In order to examine how the free volume cavities in HFA-PNB evolve over as the structure of polymer changes, a series of models intermediate to the structures developed by Chung were produced. These models show how the free volume

chain was then fixed and molecular dynamics was performed on the other 3 chains at 500 K, and 700 K. The effect of MD on chain alignment can be seen in Figure 4-8

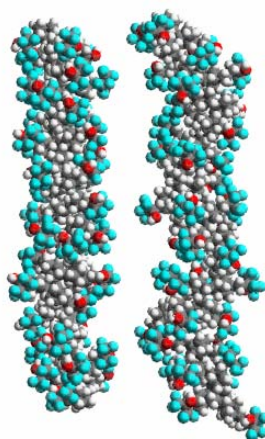


Figure 4-8: Shown on the left is the initial 40 monomer HFA-PNB chain developed by Chung for the "Perfectly Aligned" model. On the right is the same chain after MD at 700 K for 100ps. Note the elongation and more irregular structure of the second chain.

In order to produce the intermediate models constant number of particles, volume, and temperature (NVT) molecular dynamics was performed using the Cerius2 program. The force field used for this work was the same employed by Chung for HFA-PNB (10). This force field is based upon the work of Ahmed for the bi-cyclo heptane ring with Dreiding force field parameters for the HFA side chains. The Nose'-Hoover thermostat was used with a thermal bath coupling parameter of 0.100 picoseconds. For each temperature an NVT simulation was carried out for 100 picoseconds with a time step of 1 femtosecond. At the end of each simulation molecular mechanics were carried out on all 4 chains to an RMS force of 0.01 kcal/(mol Å) using the steepest decent, conjugate gradient, and Cerius2's Smart Minimizer algorithms (11). The simulated

WAXD pattern was then calculated using the Diffraction-Crystal tool in Cerius2. The defaults for the Diffraction-Crystal tool were used to calculate the Powder X-ray pattern. An isotropic temperature factor (B_{iso}) was applied to account for the kinetic motion in the static model. A value of 10 \AA^2 has been found to work well for polymeric systems. The resulting simulated WAXD patterns are shown in Figure 4-8

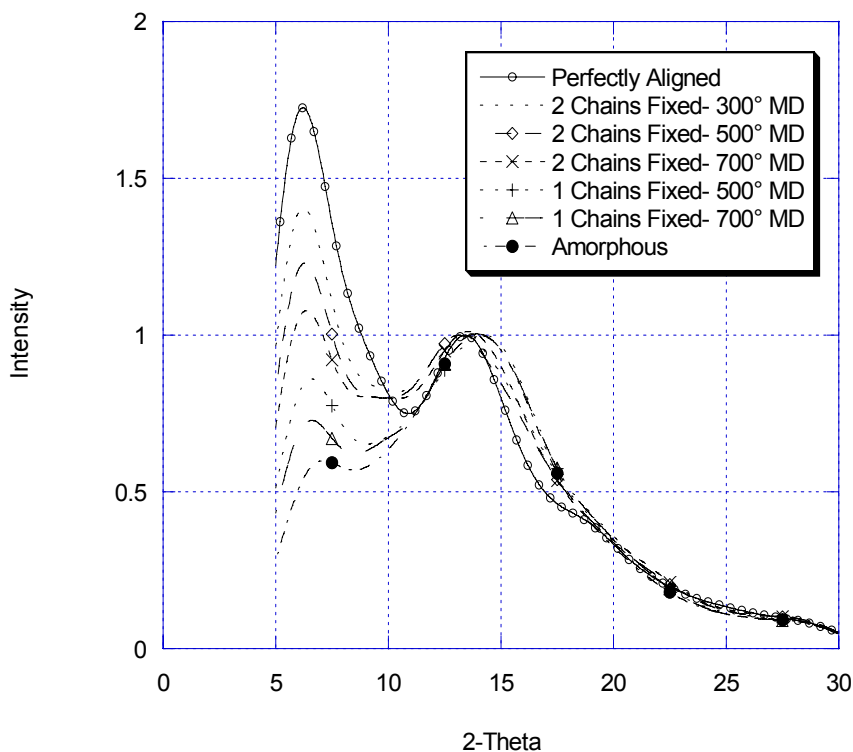


Figure 4-9: Simulated WAXD patterns of HFA-PNB representing various stages of chain alignment. Data was cutoff at 5 \AA^{-1} due to extraneous low 2 theta peaks.

The simulated WAXD patterns in Figure 4-9 match the experimental WAXD patterns in trend and peak positions. However the simulated WAXD patterns also emphasize how insensitive the WAXD patterns are to model structure, a simple slight misalignment of chains is enough to replicate the change in the intermolecular peak

height. Due to this it was deemed that the perfect and intermediate models do not contain the structural detail necessary for free volume modeling. Therefore only the amorphous model was used for free volume modeling.

REFERENCES

1. T. Bloomstein; M. Rothschild; R. Kunz; D. Hardy; R. Goodman; S. Palmacci, *Journal of Vacuum Science and Technology B*, V16, p 3154, 1998
2. T. Bloomstein; M. Rothschild; J. Curtin; D. Downs; T. Fedynyshyn; D. Hardy; R. Kunz; V. Ilberman; J. Sedlacek; R. Uttaro; A. Bates; C. Perski, *Journal of Vacuum Science and Technology B*, V17, p 3262, 1999
3. J. Mulkens; T. Fahey; J. McClay; J. Stoeldraijer; P. Wong; M. Brunotte; B. Mecking, *Optical Microlithography Proceedings SPIE*, V4691, p 613, 2002
4. Y. Bae; K. Douki; T. Yu; J. Dai; D. Schmaljohann; H. Koerner; C. Ober, *Chemistry of Materials*, V14, p 1306, 2002
5. W. Chung; P. Ludovice, PMSE Preprints, V89, pp289-290, 2003
6. S. Tao; *Journal of Chemical Physics*, V56, p5499, 1972
7. Y. Jean; H. Shi, *Journal of Non-Crystalline Solids*, V172-174, pp806-814, 1994
8. B. Jasinska; A. Koziol; T. Goworek, *Journal of Radioanalytical and Nuclear Chemistry*, V210(2), pp 617-623, 1996
9. D. Hofmann; M. Heuchel; Y. Yampolskii; V. Khotimskii; V. Shantarovich, *Macromolecules*, V35, pp 2129-2140, 2002
10. W. Chung , "Molecular Modeling of Structure-Property Relationship for Palladium Catalyzed Poly(Norbornene) and Its Derivatives ," PhD. Thesis, Georgia Institute of Technology, 2003
11. Accelrys Inc., Cerius² Users Guide-Forcefield Based Simulations, San Diego, CA, 1997

CHAPTER V

HFA-PNB FREE VOLUME

As earlier hypothesized, it is believed that HFA-substituted polynorbornene, has very elongated and irregular shapes to its free volume cavities. In order to test this hypothesis the following analysis was performed.

1. PALS experiments were performed to experimentally determine the fractional free volume in HFA-PNB samples, and the mean size and distribution of free volume cavities. These will be extracted from the ortho-Positronium (oPs) lifetime (τ_3) intensity (I_3) data.
2. Using the amorphous HFA-PNB model developed by Chung (1), a Delaunay Tessellation will be performed to calculate the free volume and its distribution.
3. Clustering of tetrahedra with faces large enough for o-Ps to pass through will be performed. These clusters will be used to examine the larger shape of free volume cavities.
4. The free volume distribution obtained from Delaunay analysis on both tetrahedra and clusters will be compared with PALS experimental data.

5.1 HFA-PNB Positron Annihilation Lifetime Spectroscopy Experiment

In order to form comparisons with simulated free volume results, PALS was carried out on a series of HFA samples. The HFA-PNB samples used for PALS testing were provided by Promerus Electronic Materials. The monomer, α , α - bis(trifluoromethyl)bicyclo[2.2.1]hept-5-ene-2-ethanol (HFANB) (2), was polymerized

with cationic palladium catalysts (3-5). The molecular weights of the samples were controlled using varying amounts of chain transfer agent (hexane) (6). The molecular weights were then determined using gel permeation chromatography (GPC) using four ultrastyrigel columns in tetrahydrofuran at 50° C. A polystyrene calibration curve was used for molecular weight determination. The molecular weights are listed in Table 5-1.

Table 5-1: The M_w and polydispersity index for HFA-PNB samples

Molecular Weight (M_w)	Polydispersity Index
5029	1.4
10425	1.72
13191	1.81
27049	2.05
91967	2.29
180108	2.68

Sample films for PALS analysis were made from polymer solutions containing 20 weight % solids dissolved in propylene glycol methyl ether acetate (PGMEA) overnight. Films were spuncast onto 2 inch silicon (100) wafers at speeds ranging from 2000 to 3500 revolutions per minute, to a film thickness of 900 nm. Films were then post-applied baked at 130°C for 90 seconds.

The PALS testing was performed by the Jean research group at the University of Missouri- Kansas City (7), The instrument used was the UMKC Slow Positron Beam

with a Na^{22} source used for positron generation. (8) An illustration of the instrument is shown in Figure 5-1.

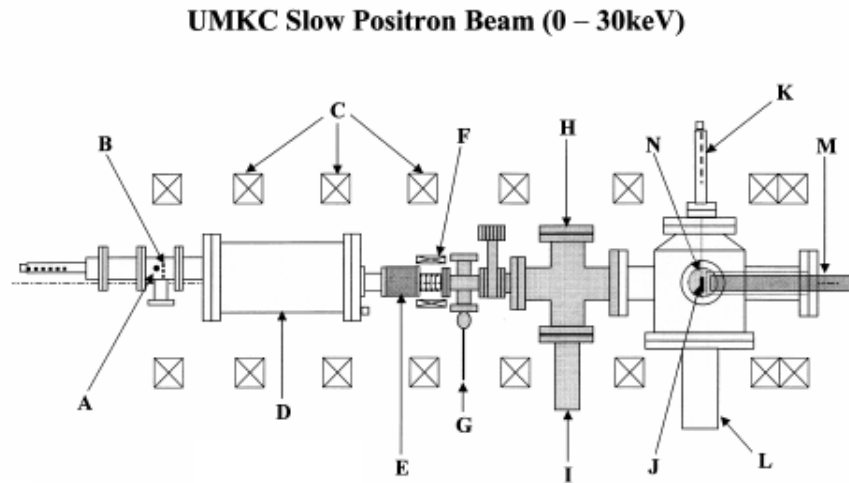


Figure 5-1: Schematic of Slow Positron Beam used for PALS testings. (A: positron source; B: W-mesh moderator; C: magnetic field coils; D: filter; E: positron accelerator and electric insulator; F: correcting magnets; G: gas inlet; H: positron lifetime system for PAL; I: turbo molecular pump; J: sample; K: sample manipulator; L: cryo pump; M: Ge solid state detector; N: PAL detector)

The Slow Positron Beam has the ability to profile the free volume in a sample as a function of depth. This is achieved by the regulation of the voltage applied to the source end of the instrument. The voltage can be regulated from 0-30 keV. The correlation (9) to the voltage applied to the source and the implantation depth of positrons into the sample is

$$z(E) = \left(\frac{400}{\rho}\right)E^{1.6} \quad [1.1]$$

where z is the depth expressed in \AA , ρ is the sample density in g/cm^3 , and E is the incident energy in keV.

The lifetime, intensity and fractional free volume data are summarized in the following figures.

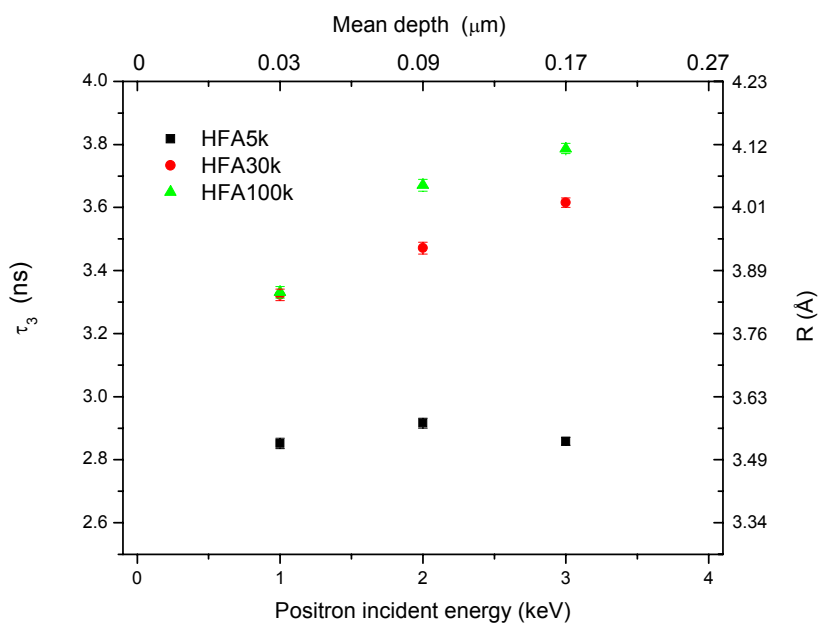


Figure 5-2: o-Ps Lifetime data for HFA samples of MW 5000, 30000, and 100000 at various sample depths. MW are approximate and are based on Gel Permeation Chromatography

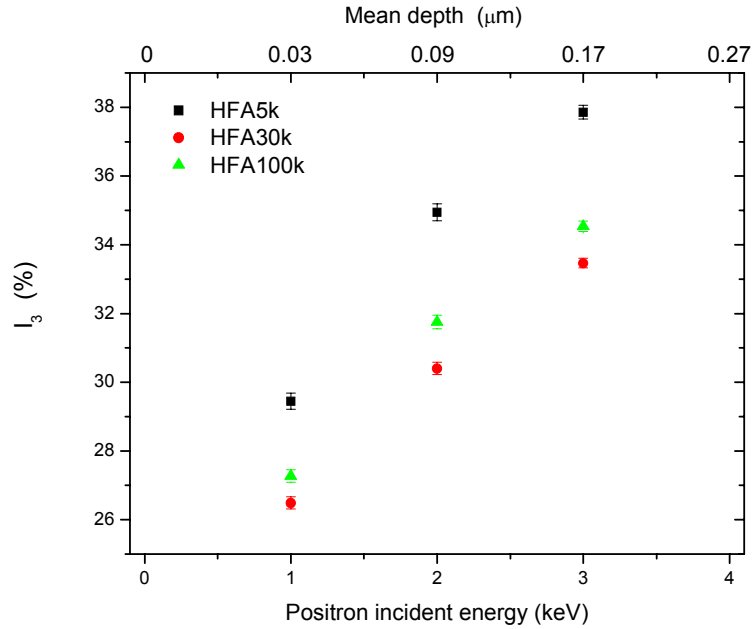


Figure 5-3: Intensity data for HFA samples of MW 5000, 30000, and 100000 at various sample depths

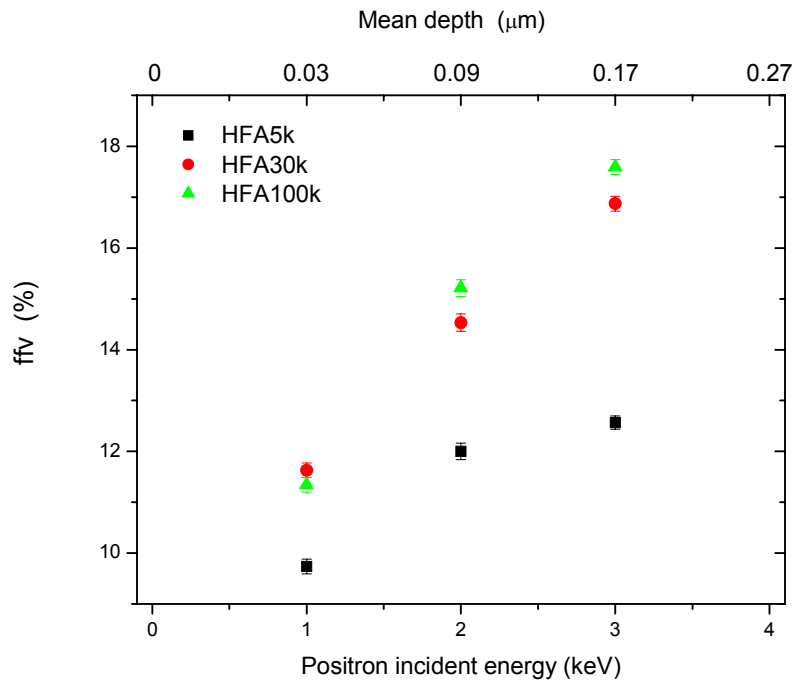


Figure 5-4: Fractional free volume data for HFA samples of MW 5000, 30000, and 100000 at various sample depths. Conversion from lifetime and intensity data to ffv data was performed using equations [3.1-3.3]

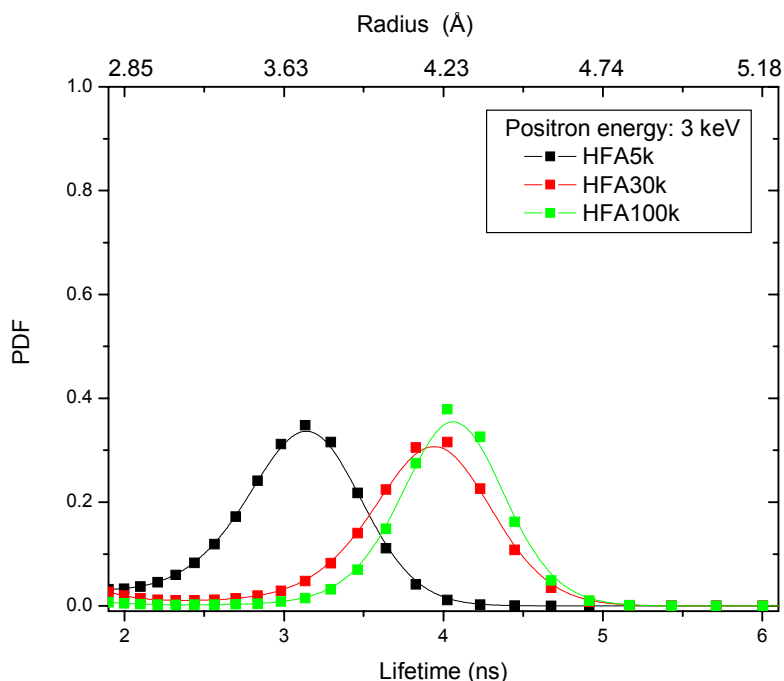


Figure 5-5: Probability distribution function of o-Ps lifetimes and free volume cavity radii from HFA samples of MW 5000, 30000, and 100000 at a sample depth of 0.17 μm .

In Figure 5-2, it can be seen that there is a distinct trend for τ_3 . As molecular weight increases, the lifetime also increases. This would indicate larger free volume pockets. This is consistent with the theory that HFA-PNB is a helical structure with occasional kinks and a longer chain would have more kinks. The more kinks in the chain, the more irregular the packing becomes and larger the free volume cavities become. Figure 5-5 indicates that the entire distribution of τ_3 shifts to higher values as MW increases. This shift is most notable from MW 5000 to MW 30000. Figure 5-3 shows that there is a lower numeric concentration of annihilations, hence free volume pockets, for higher molecular weight samples. Finally, the combined data in the form of the fractional free volume (Figure 5-4) indicates that overall, taking the size of the free volume cavities and number into account, the trend of the increasing cavity size dominates and there is more fractional free volume for the higher molecular weights

(0.175 and 0.16 respectively for the 100000 and 30000 MW) than for the lower 5000 MW (0.125).

Hoskins et.al (10) described the MW effect on dissolution rate of HFA-PNB (a key characterization for a photoresist material).

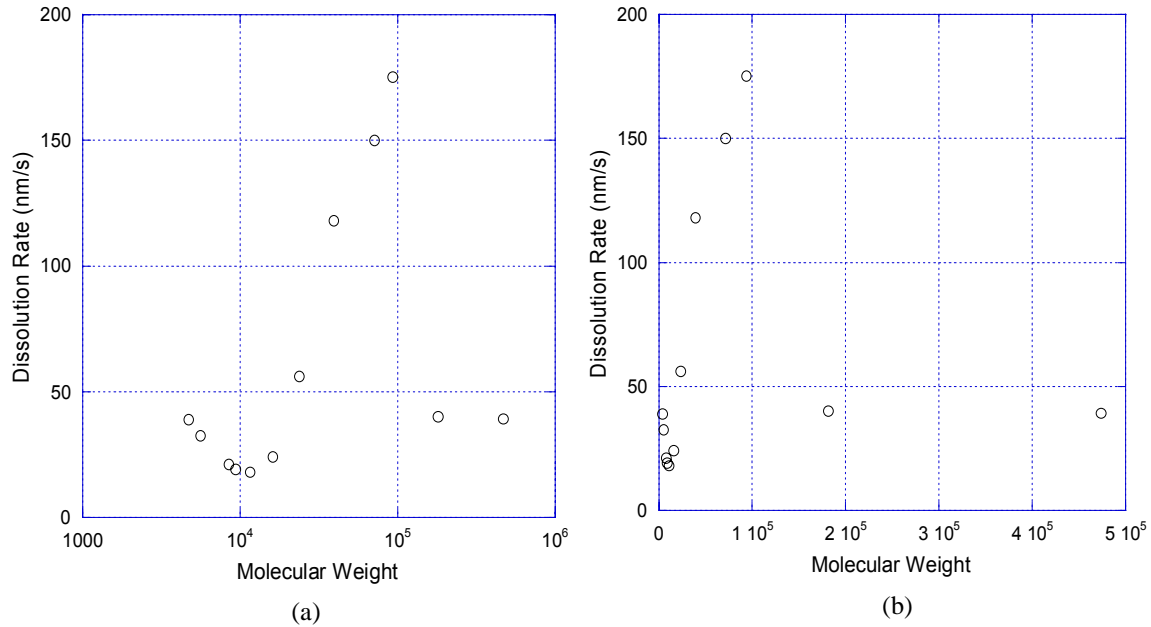


Figure 5-6: Dissolution behavior of HFA-PNB as a function of molecular weight shown in log scale (left) and linear (right)

This behavior was explained as a result of changes in hydrogen bonding in the polymer as more kinks were added as MW increased. Given the increases in fractional free volume, the increased dissolution rate may also be a result of more free volume assessable for developer as MW increases.

5.2 HFA-PNB Free Volume Analysis Amorphous Sample

Next a simulated model of HFA-PNB was examined via Delaunay Tessellation to better understand the specific development of free volume in this polymer. For this

analysis the “Amorphous” or 2 chain of 100 monomer simulated structure was chosen as being the most representative structure of free volume in HFA-PNB (See Chapter 4 for the development of this model and Figure 5-7 for an illustration). This represented a molecular weight of 27400 per chain. It is also representative of high molecular weights of HFA-PNB in general with poor intermolecular alignment. The analysis was carried out using the aforementioned Delaunay method and the results are summarized in the following charts.

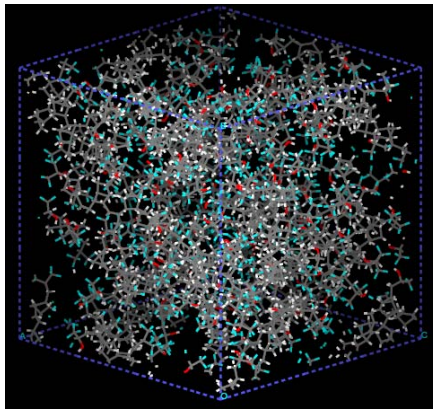


Figure 5-7: Single cell view of the amorphous HFA-PNB model. Note the large void areas representing free volume.

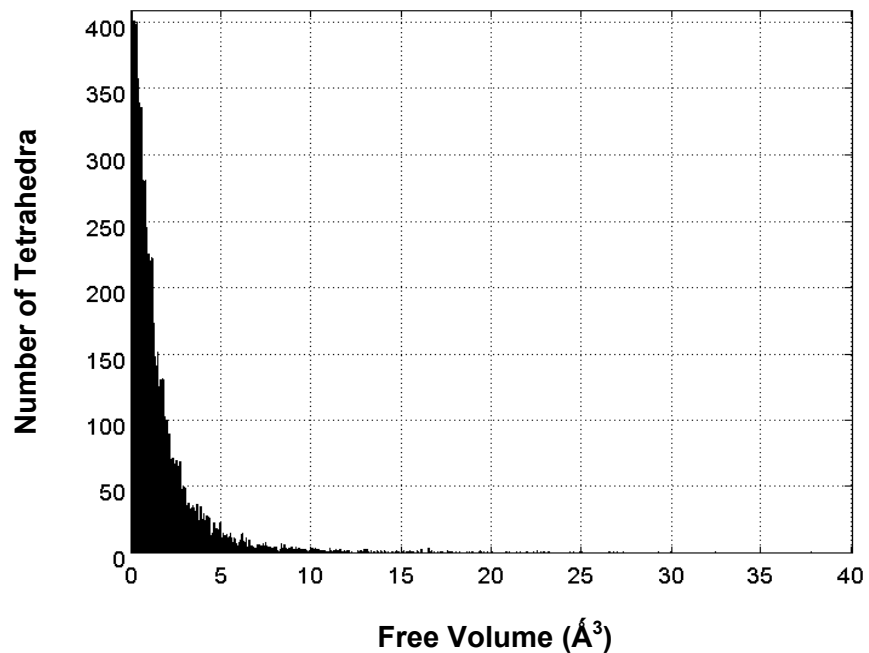


Figure 5-8: Free volume distribution among tetrahedra for amorphous HFA-PNB model

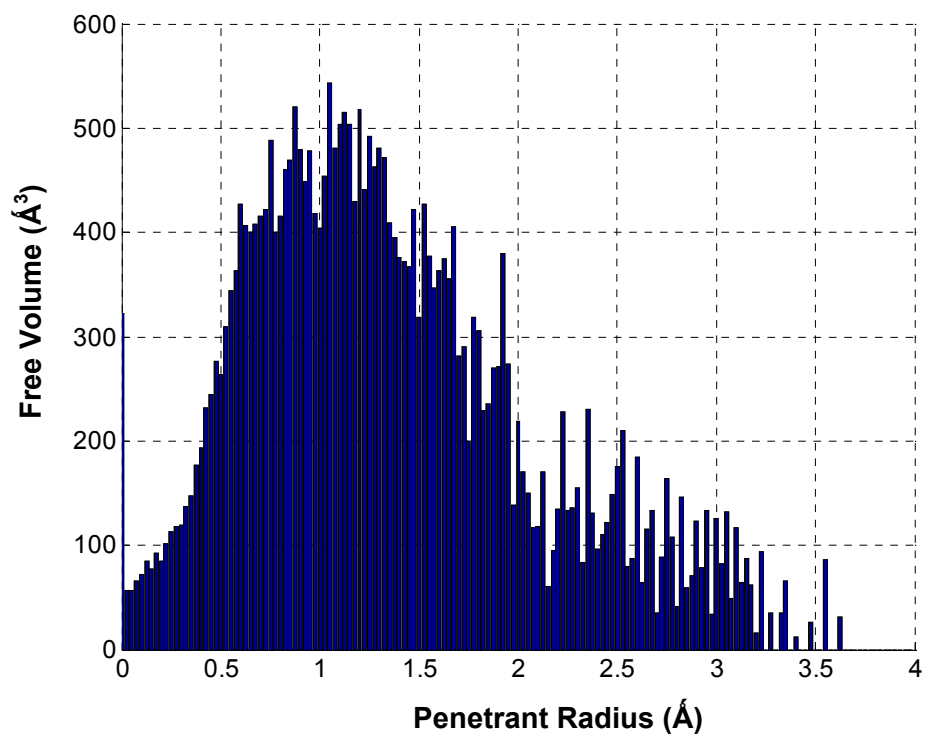


Figure 5-9: Histogram of total free volume within tetrahedra by penetrant radius for amorphous HFA-PNB model

Table 5-2: Free volume distribution statistics

Polymer	Penetrant Radius (Å)	Standard Deviation	Skewness	Kurtosis
HFA-PNB	1.369	0.546	1.592	6.890

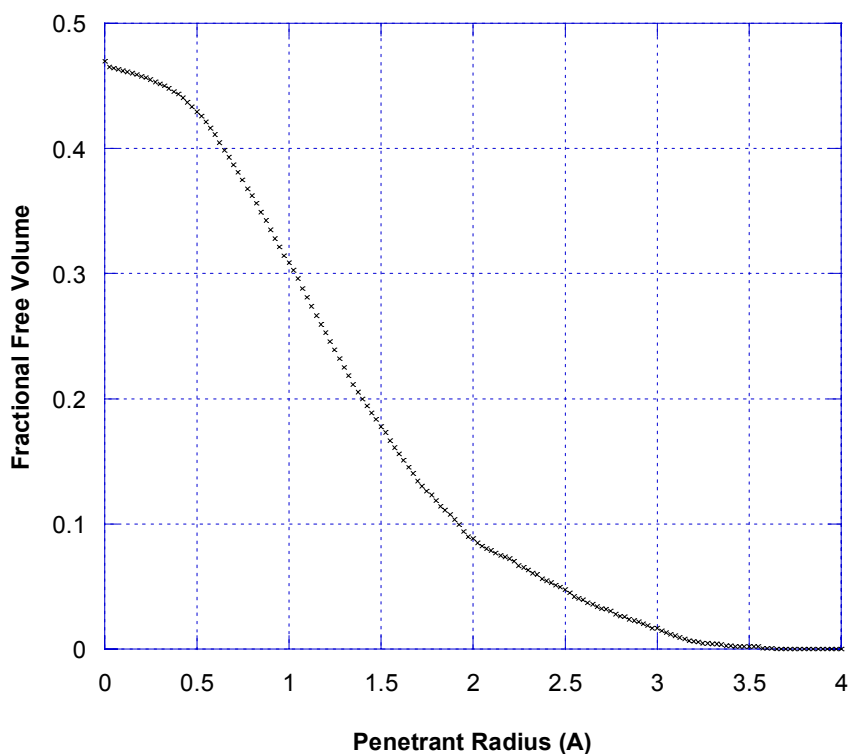


Figure 5-10: Fractional free volume distribution for amorphous HFA-PNB

Figure 5-8 shows that the distribution of tetrahedron volumes for HFA-PNB are similar to those seen in for PET and PEN (see Chapter 3- Table 3-3). The largest tetrahedra is approximately 37 \AA^3 . There are also a large number of very small

tetrahedron. When examining Figure 5-9 and the accompanying statistics in Table 5-2, it can be noted that the distribution of tetrahedron volumes by penetrant radius is fairly normal but slightly skewed to larger penetrant radii. This moves the mean penetrant radius from what would appear to be approximately 1 Å to 1.369 Å. Also for tetrahedra at the mean penetrant radius the total accessible free volume is approximately 500 Å³, much larger than noted for the typical glassy polymer represented by PET and PEN at 290 Å³. (See Chapter 3- Figures 3-5 and 3-6) Examining the full free volume distribution in Figure 5-10, it seems that the overall fractional free volume in the simulated amorphous HFA-PNB is approximately 0.47 but at a penetrant radius of 1.20 Å, the fractional free volume is 0.25. This value is higher than the experimental results for the high molecular weight HFA-PNB samples (Figure 5-4), but are not corrected for thermal effects. Thermal effects would increase the representative van der Waal volume for the atomic system, hence lowering the fractional free volume. If it is assumed that the thermal effects can be taken into account by reducing the simulated free volume by 30%, then the values compare well with the experimental data. This correction is different from the thermal correction proposed by Van Krevelen (11), which is an increase of the van der Waal volume by 30%. Making Van Krevelen's correction would result in the simulated free volume being decreased by a factor of 10. Given the experimental value a fractional free volume of 0.025 seems unreasonable. The reason that Van Krevelen's correction does not work in this instance may be because the assumptions used to develop the thermal correction are based on amorphous polymer systems and interactions. HFA-PNB (as indicated by the WAXD patterns in Figure 4.7) has intermediate order and the same assumptions for free volume may not be applicable.

The 30% reduction of the simulated fractional free volume was carried forth in the rest of the calculations in this work.

5.3 HFA-PNB Clustering Amorphous Sample-Volume Analysis

After Delauny tessellation, the clustering analysis described in Chapter 3 was applied to the amorphous sample. The sample was clustered based on shared faces of the size of o-Ps or 1.20 \AA or larger. This resulted in 210 clusters composed of 4237 tetrahedra. The results of the cluster analysis are shown in the following figures.

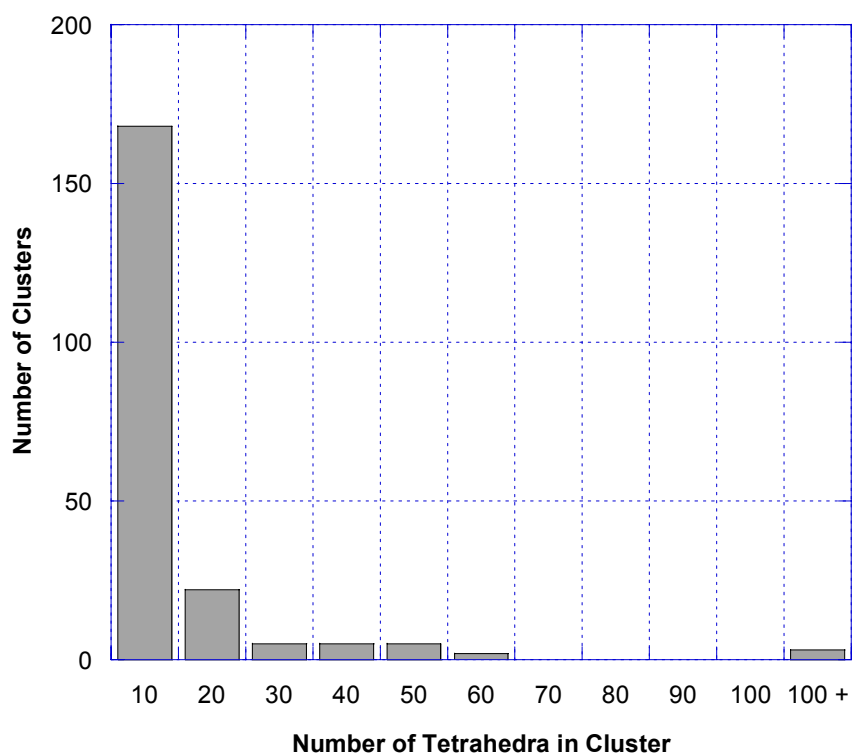


Figure 5-11: Distribution of the number of tetrahedra per cluster of o-Ps radius size for simulated amorphous HFA-PNB

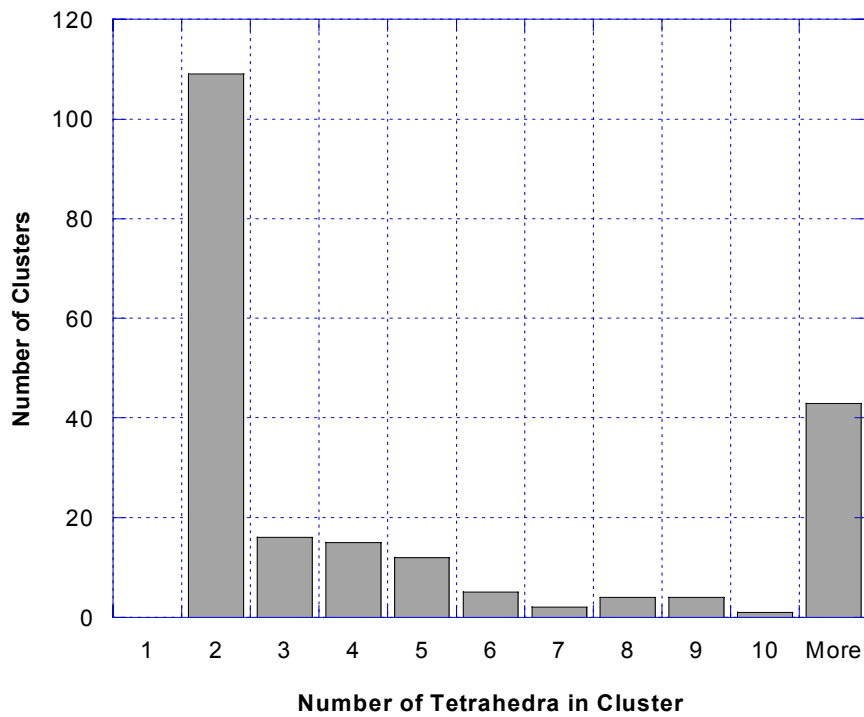


Figure 5-12: Distribution of tetrahedron per cluster of o-Ps radius size for simulated amorphous HFA-PNB for clusters with 10 or less tetrahedron per cluster. Note that due to the definition of a cluster it can not contain less than 2 tetrahedra

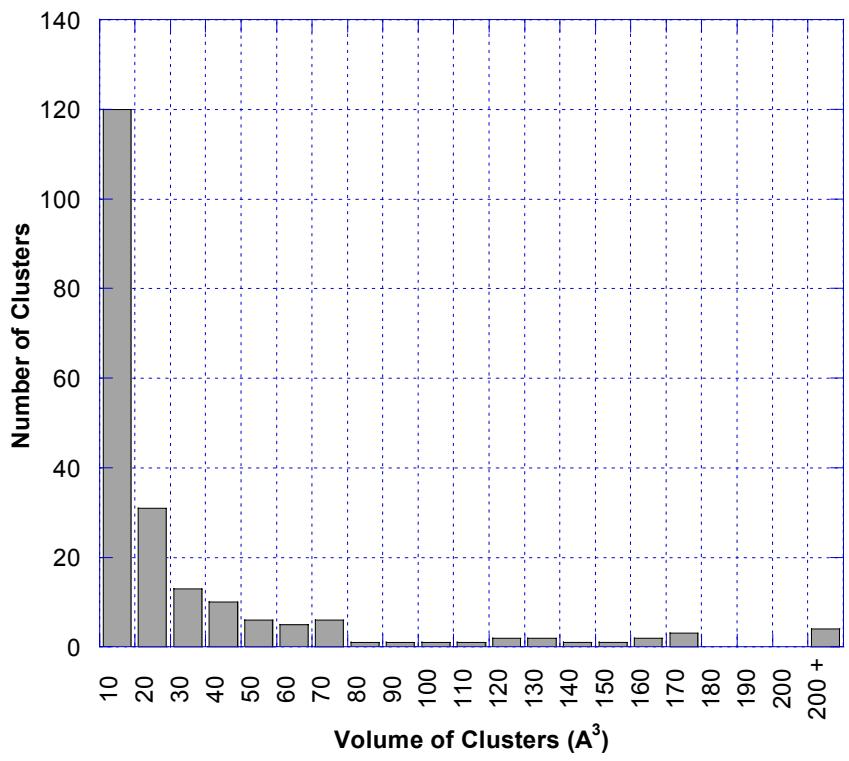


Figure 5-13: Distribution of cluster volume of o-Ps radius size for simulated amorphous HFA-PNB

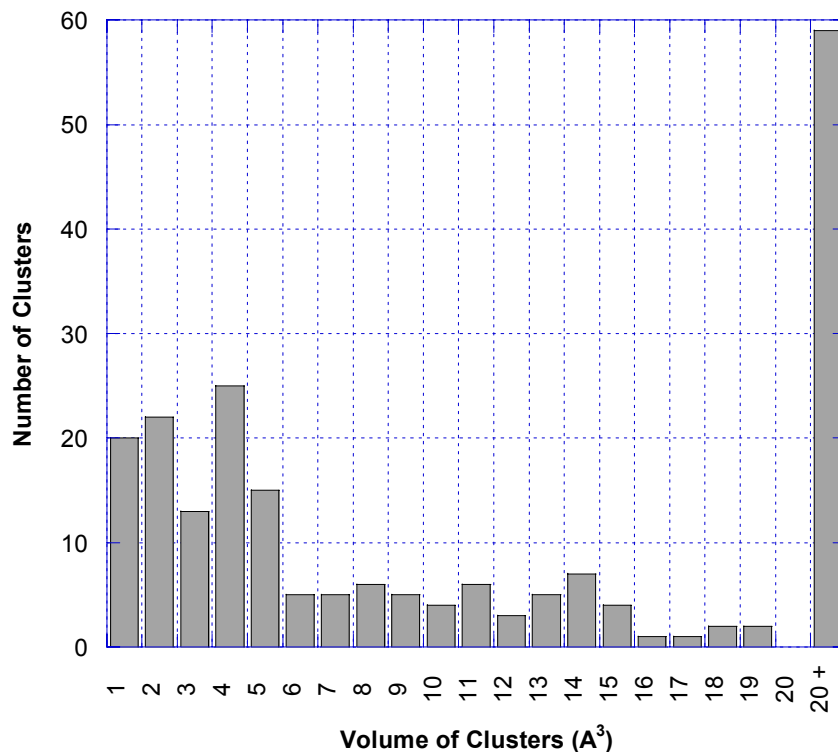


Figure 5-14: Distribution of cluster volumes of o-Ps radius size for simulated amorphous HFA-PNB for clusters with volumes of 10 or less cubic angstroms

Figure 5-11 shows that most of the clusters found in HFA-PNB are relatively small, containing 10 or less tetrahedra per cluster. Figure 5-12 shows that most of the clusters in this region are in fact composed of clusters with 2 tetrahedra per cluster. The average size of these 2 tetrahedra clusters is 3.331 \AA^3 . Figure 5-13 shows that most clusters are also relatively small in volume, with most being less than 10 \AA^3 . Figure 5-14 shows that the volume of most clusters is less than 5 \AA^3 . Perhaps the most interesting data in the clustering analysis are the outlying points, clusters of large number of tetrahedra. These points are shown in Table 5-3.

Table 5-3: Three largest o-Ps clusters in amorphous HFA-PNB.

<u>Cluster Identifier</u>	<u>Number of tetrahedron per cluster</u>	<u>Percent of o-Ps tetrahedron</u>	<u>Cluster Volume (Å³)</u>	<u>Percent of total clustered free volume</u>
A	2472	58.3%	11406.60	66.4%
B	191	4.5%	851.80	5.0%
C	105	2.5%	367.67	2.1%

Most of the tetrahedra and clustered free volume accessible to o-Ps is found in these 3 clusters, the largest of which is more than 66% of the total clustered free volume. This largest cluster may be associated with the kinks in the 2 chains which compose the amorphous sample, and sheds light on how kinks can open up chunks of free volume in HFA-PNB structures.

5.4 HFA-PNB Clustering Amorphous Sample-Shape Analysis

To analyze the shape of free volume clusters, the radius of gyration tensor (S_{ij}) was calculated for each set of cluster coordinates using

$$S_{ij} = \sum_{k=1}^N (x_{ik} - x_{cm})(x_{jk} - x_{cm}) \quad [5.1]$$

The eigenvalues of (S_{ij}), $\langle x_0^2 \rangle$, $\langle y_0^2 \rangle$, and $\langle z_0^2 \rangle$ give information about relative shape of each cluster dimension. To accurately compare the cluster shape across clusters, for a given cluster, each eigenvalue was normalized by the average eigenvalues for that cluster. The normalized eigenvalues can then be averaged for all the clusters in a model to get a sense of the average dimensions of a cluster for HFA-

PNB. To assure that the large outlying clusters did not bias the results, their eigenvalues were not included in the averaging process and were reported separately.

Table 5-4: Cluster eigenvalues for HFA-PNB. Confidence intervals on average cluster values are 95% confidence levels

Cluster	Normalized $\langle x_0^2 \rangle$	Normalized $\langle y_0^2 \rangle$	Normalized $\langle z_0^2 \rangle$
Average	1.694 ± 0.044	0.869 ± 0.023	0.437 ± 0.030
A	1.292	0.961	0.747
B	1.442	0.889	0.670
C	1.385	0.920	0.694

Table 5-5: Aspect ratios of HFA-PNB clusters

Cluster	$\frac{\langle x_0^2 \rangle}{\text{Average}(\langle x_0^2 \rangle, \langle y_0^2 \rangle, \langle z_0^2 \rangle)}$
Average	1.694
A	1.292
B	1.442
C	1.385

Tables 5-4 and 5-5 indicate that the clusters found in HFA-PNB are non spherical. For the average cluster the longest axis is more than 1.5 times larger than the

average of the axes. For the outlying clusters, the difference is not as large but the data indicates that the three outlying clusters also have a prolate ellipsoidal shape.

5.5 HFA-PNB Clustering Amorphous Sample- τ_3 Analysis

To compare the experimental free volume results to the simulated free volume analysis, the o-Ps lifetime was used as a point of comparison. The probability distribution function of lifetimes (τ_3) were extracted from the PALS experiment. To develop the simulated lifetime distribution two approaches were taken:

1. From the Dealunay tessellation analysis, the volume of each tetrahedron was selected. Each volume was then assumed to be spherical and a radius was calculated. From this spherical radius τ_3 can be calculated using equation [4.1]
2. From the clustering analysis, the volume of each cluster was selected. Each volume was then assumed to be spherical and a radius was calculated. From this spherical radius τ_3 can be calculated using equation [4.1]

The resulting lifetime distributions are shown in Figures 5-15 through 5-18.

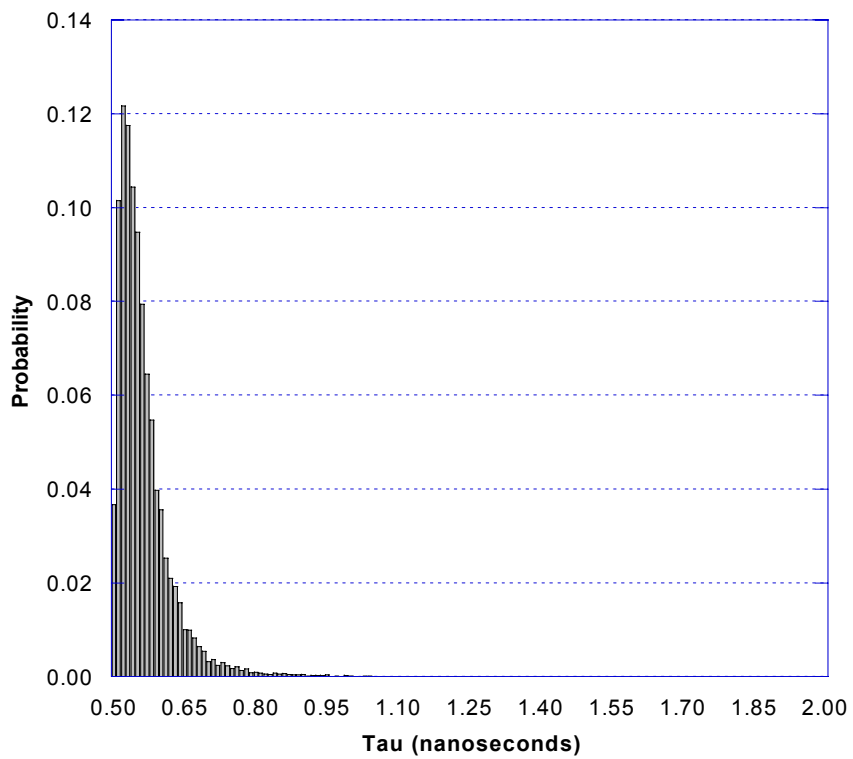


Figure 5-15: Simulated lifetime distribution of amorphous HFA-PNB based upon individual tetrahedron. Probability is based upon all tetrahedron in model.

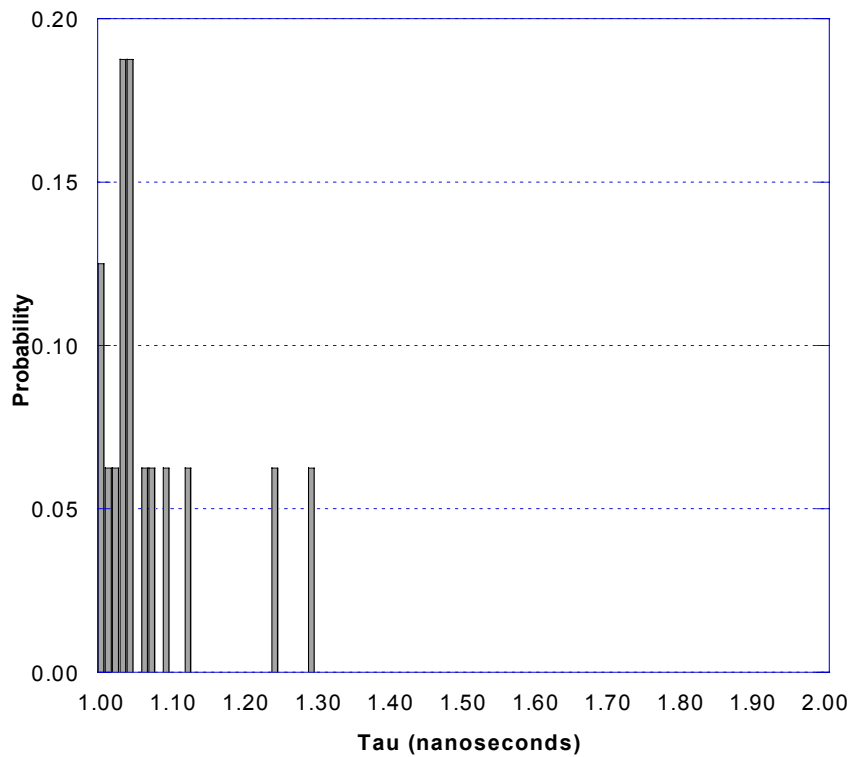


Figure 5-16: Simulated lifetime distribution of amorphous HFA-PNB based upon individual tetrahedron within relevant lifetime range. Probability is based upon tetrahedron in model with lifetimes greater than 1ns.

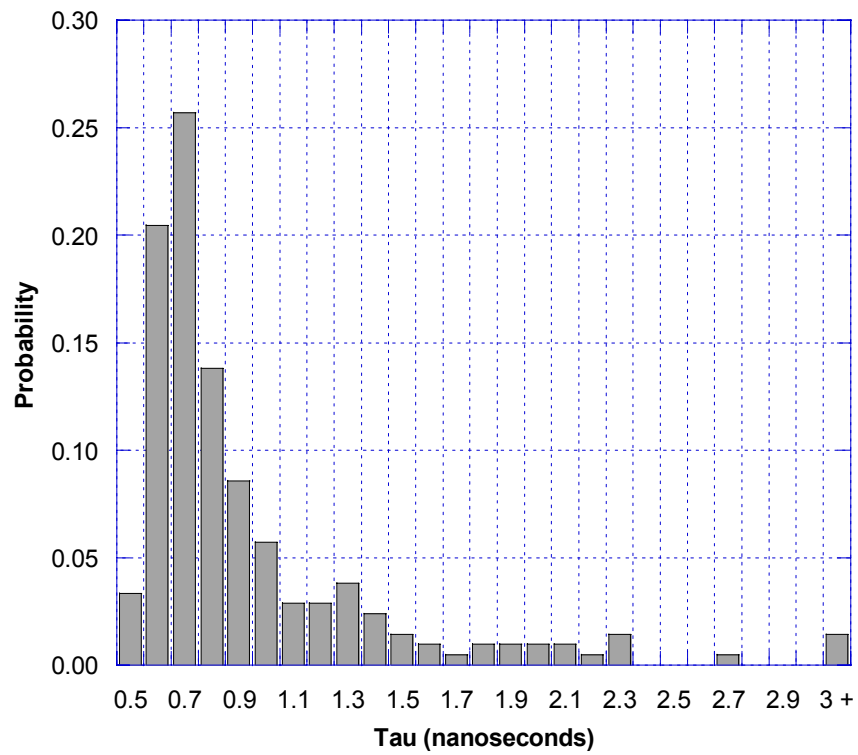


Figure 5-17: Simulated lifetime distribution of amorphous HFA-PNB based upon clustered tetrahedron. Probability is based upon all clusters in model.

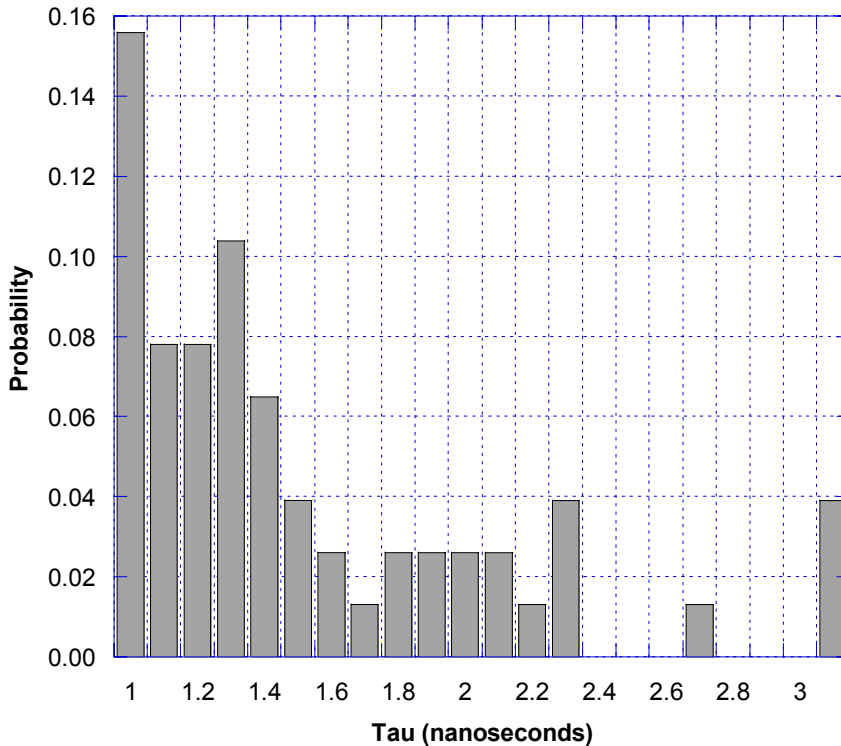


Figure 5-18: Simulated lifetime distribution of amorphous HFA-PNB based upon clustered tetrahedron within relevant lifetime range. Probability is based upon clusters in model with lifetimes greater than 1ns.

When examining the lifetime distributions based upon single tetrahedron, in Figures 5-15 and 5-16, it can first be noted that they are dominated by very small lifetimes. This is consistent with the small volume of the individual tetrahedron. It can also be noted that the distribution is skewed to the right. Of more interest is the lifetime distribution of clustered tetrahedron shown in Figures 5-17 and 5-18. First to note is that this distribution is much less normal than the distribution of individual tetrahedron and more skewed to the right.

To properly compare the clustered lifetime data to experimental values, the spherical lifetimes must be corrected by using equation [4.2] to convert the calculated

τ_{sphere} to $\tau_{elliptical}$. The aspect ratios shown in Table 5-5 have been converted to eccentricities ε defined by the equation

$$\varepsilon = \frac{\sqrt{a^2 - b^2}}{a} \quad [5.2]$$

where a is defined as $\langle x_0^2 \rangle$ and b is the average of all 3 cluster eigenvalues. The eccentricities are summarized in Table 5-6.

Table 5-6: Cluster eccentricities for HFA-PNB. The 95% confidence interval is shown for the average cluster.

<u>Cluster</u>	<u>Eccentricity</u>
Average	0.772±0.016
A	0.633
B	0.720
C	0.692

After $\tau_{elliptical}$ is calculated for each cluster an mean lifetime $\tau_{ell.average}$ can then be calculated for clusters with lifetimes larger than 1 ns (the relevant range for o-Ps) using

$$\tau_{ell.average} = \frac{1}{Volume_{total}} \sum_{i=1}^N Volume_{(i)} * \tau_{elliptical.(i)} * \xi \quad [5.3]$$

where $Volume_{total}$ is the total volume of all the clusters, $Volume_{(i)}$ and $\tau_{elliptical.(i)}$ are the volume and lifetimes of cluster i, and ξ is a correction factor to the cluster volume used to compensate for the higher surface to volume ratio of the clustered tetrahedra. The sensitivity of $\tau_{ell.average}$ to this probability, shown in Figure 5-15, indicates that a ξ of

0.405 results in a lifetime of 4 ns, the same mean lifetime as for the high molecular weight experimental PALS results shown in Figure 5-19.

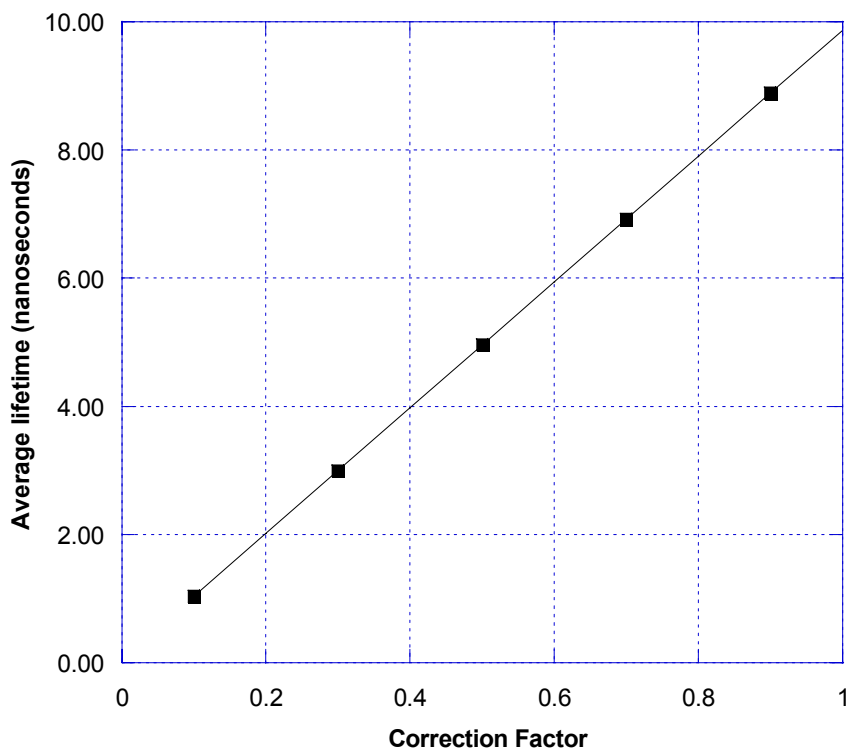


Figure 5-19: Average HFA cluster lifetime $\tau_{ell.average}$ as a function of ξ .

This means that the volume of the defined clusters must be decreased by 60% to represent the higher surface to volume ratio of the clusters. This higher surface area to volume ratio lowers the simulated lifetime. This result is reasonable since for clusters with tortuous paths, there will be a low probability that the o-Ps would be able to sample the volume before annihilation. Hence there is a good fit between the lifetimes calculated for free volume clusters and the experimental data from PALS.

Analysis of the simulated amorphous sample using the Connelly Surface tool in the Cerius2 Program resulted in the visualization shown in Figure 5-20. The probe radius

used was 1.2 Å and the rest of the variables were set at program defaults. The analysis calculated an interior surface area of 14620 Å² which represents a total surface area to total volume ratio of 0.212 and a total surface area to total free volume (at 1.2 Å penetrant radius) of 0.848. While this tool does give an initial surface area measurement of the model, it gives a cumulative measure of this value, not on the basis on individual clusters. A measure of the surface to free volume ratio for individual clusters is necessary for a better measure of the parameter ξ .

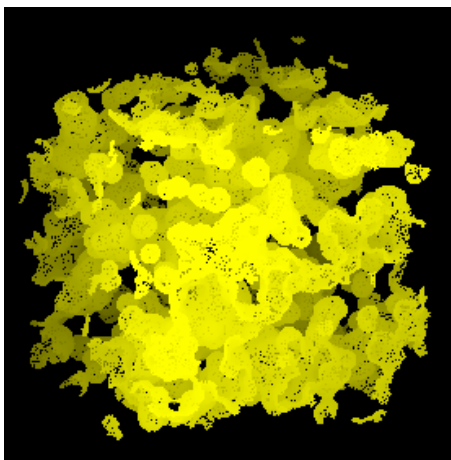


Figure 5-20: Connolly Surface of amorphous HFA-PNB periodic cell. Note the large connected free volume pockets as well as the smaller isolated free volume pockets.

REFERENCES

1. W.Chung , "Molecular Modeling of Structure-Property Relationship for Palladium Catalyzed Poly(Norbornene) and Its Derivatives ," PhD. Thesis, Georgia Institute of Technology, 2003
2. H. Tran; R. Hung; T. Chiba; S. Yamada; T. Mrozek; Y. Hsieh; C. Chambers; B. Osborn; B. Trinqué; M. Pinnow; S. MacDonald; C. Wilson; D. Sanders; E. Connor; R. Grubbs; W. Conley, *Macromolecules* V35, pp 6539-6549, 2002
3. B. Goodall; S. Jayaraman; R. Shick; L. Rhodes, U.S. Patent 6136499, 2000
4. J. Lipian; L. Rhodes; B. Goodall; A. Bell; R. Mimna; J. Fondran; S. Jayaraman; A. Hennis; C. Elia; J. Polley; A. Sen U.S. Patent 6455650, 2002
5. J. Lipian; R. Mimna; J. Fondran; D. Yandulov; R. Shick; B. Goodall; L. Rhodes; J. Huffman, *Macromolecules* V35, pp 8969-8977, 2002
6. L. Rhodes, *Proceedings of SPIE-The International Society for Optical Engineering*, 2005
7. Y. Jean Research Group, Department of Chemistry, University of Missouri-Kansas City, Kansas City, MO
8. R. Zhang; H. Cao; H. Chen; P. Mallon; T. Sandreczki; J. Richardson; Y. Jean; B. Nielsen; R. Suzuki; T. Ohdaira, *Radiation Physics and Chemistry*, V58, pp 639-644, 2000
9. P. Schultz; K. Lynn, *Review of Modern Physics*, V60, p 701, 1988
10. T. Hoskins; W. Chung; P. Ludovice; C. Henderson; L. Seeger; L. Rhodes; R. Shick, *Proceedings of SPIE-The International Society for Optical Engineering*, V5039, pp 600-611, 2003
11. D. Van Krevelen, *Properties of Polymers-Correlation with Chemical Structure*, p 41, 1972

CHAPTER VI

CONCLUSIONS AND RECOMMENDATIONS

In this dissertation, the links between polymeric free volume, structure, and transport properties were examined. The work addresses two specific polymers, polyesters, which are amorphous polymer glasses, and Hexafluoroalcohol-substituted Polynorbornene (HFA-PNB), which contains a level of order intermediate between the amorphous and crystalline state.

Polyethylene Terephthalate (PET) and Polyethylene Napthalate (PEN)

Hypothesis 1: A comparison of free volume and free volume distribution developed from accurate molecular models of PET and PEN should predict the higher fractional free volume found in PEN for the same gaseous penetrant.

Conclusions

- **The fractional free volume analysis of accurate molecular models of PET and PEN are consistent with experimental PALS results for ortho-positronium (o-Ps) and for gas solubility results for O₂.** Molecular models developed using new PET and PEN RIS models were analyzed using Delaunay Tessellation. The volumes of simulated Delaunay tetrahedra accessible to o-Ps and O₂ penetrants were not statistically different between the PET and PEN models. However, there was a statistically significant difference in the distribution of clusters of Delaunay tetrahedra between the PET and PEN models for the O₂ penetrant only. This is consistent with the experimental observation that the free

volume distributions measured by PALS are the same for PET and PEN, but O₂ is more soluble in PEN relative to PET. By grouping the tetrahedron into clusters based upon the ability of a given sized penetrant to move across the face, free volume structures larger than single tetrahedral could be analyzed. Specifically, there is a statistically (at 99% significance level) larger number of small clusters (containing less than 10 tetrahedra/cluster and between 20-30 Å³ in size) in PEN than in PET. This correlation suggests that penetrants move about between individual Delaunay tetrahedral and it is this clustered difference in free volume distribution that appears to explain the higher O₂ solubility in PEN.

Recommendations

- Use the understanding of the link between free volume and solubility represented in this work and molecular dynamic simulations to study diffusivity and overall gas permeability and how they are related to free volume.
- Test the Delaunay Tessellation / Clustering analysis on other amorphous polymeric systems in which free volume is believed to play a large role in gas solubility.

Hexafluoroalcohol substituted Polynorbornene (HFA-PNB)

Hypothesis 2: The microvoids found in HFA-PNB are highly non-spherical.

Conclusions

- **Simulations indicate the systematic decrease in the intermolecular peak of the HFA-PNB WAXD pattern the occurs with increasing polymer molecular weight can be explained by a decrease in intermolecular alignment.**

Molecular dynamic simulations of a series models containing 4 chains with 40 HFA-PNB monomers each were successful in replicating the relative intermolecular peak decrease seen in experimental WAXD patterns of HFA-PNB covering a molecular weight range from 5000 to 470000.

- **The free volume cavities found in large molecular weight HFA-PNB are only slightly non-spherical.** Using an amorphous molecular model of HFA-PNB which is representative of high molecular weight chains with several kinks a Delaunay Tessellation and clustering analysis was performed. The average aspect ratio of the clusters was approximately 1.5.
- **The experimental mean o-Ps lifetime of high molecular weight HFA-PNB can be modeled by clusters of free volume by correcting for the shape of the cluster.** As with the PET and PEN results, the Delaunay tetrahedral HFA-PNB volume was not able to replicate the measured PALS lifetimes. However, neither were the large clusters in the model. The PALS results indicate that volumes sampled by o-Ps are intermediate between the tetrahedra and the clusters of tetrahedra. Correcting the effective volume of the clusters based on their slightly non-spherical shape is not sufficient to reproduce the PALS results. Therefore this suggests that the o-Ps complex samples some subset of the large clusters of tetrahedra. This means that the o-Ps can sample more than one tetrahedra, but is not likely to completely sample large clusters of tetrahedra as their probability for annihilation is increased due to the higher surface/ volume ratio as compared to separate individual tetrahedra.

Recommendations

- Use multiple models of amorphous HFA-PNB to give a better statistical representation of the few larger clusters in these models.
- Develop a Monte Carlo Sampling model to probe interior surface area in clusters.
- Develop a series of varying molecular weight HFA-PNB molecular models and investigate free volume, free volume distribution, and clustered free volume trends. By tracking the changes in how the void volume changes in character as a function of molecular weight the performance of HFA-PNB for membrane applications can be better gauged.
- Use clustering analysis on simulated alkyl substituted PNB to better understand the free volume changes with side group. By clustering free volume in alky PNB, changes in the gas transport properties can be mapped directly to changes in free volume connectivity. The relative amounts of free volume associated with the side chain and backbone can also be examined.